Forschungszentrum Jülich
in der Helmholtz-Gemeinschaft

Optimization of Tracer Experiments to Characterize Transport Properties in Heterogeneous Aquifers Using Non-Invasive Measurement Techniques

Kerstin Müller

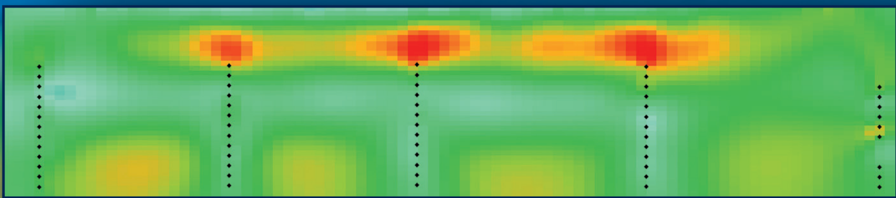

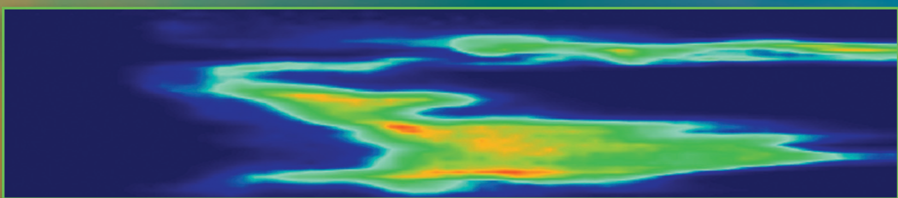

Umwelt
Environment

Schriften des Forschungszentrums Jülich
Reihe Umwelt/Environment Band/Volume 71

Forschungszentrum Jülich GmbH
Institut für Chemie und Dynamik der Geosphäre IV: Agrosphäre

Optimization of Tracer Experiments to Characterize Transport Properties in Heterogeneous Aquifers Using Non-Invasive Measurement Techniques

Kerstin Müller

Schriften des Forschungszentrums Jülich
Reihe Umwelt/Environment Band/Volume 71

ISSN 1433-5530 ISBN 3-89336-465-X

Bibliographic information published by the Deutsche Nationalbibliothek.
The Deutsche Nationalbibliothek lists this publication in the Deutsche Nationalbibliografie; detailed bibliographic data are available in the Internet at http://dnb.d-nb.de.

Publisher and Distributor:	Forschungszentrum Jülich GmbH Zentralbibliothek, Verlag 52425 Jülich Phone +49 (0)2461 61-5368 · Fax +49 (0)2461 61-6103 e-mail: zb-publikation@fz-juelich.de Internet: http://www.fz-juelich.de/zb
Cover Design:	Grafische Medien, Forschungszentrum Jülich GmbH
Printer:	Grafische Medien, Forschungszentrum Jülich GmbH

Schriften des Forschungszentrums Jülich
Reihe Umwelt / Environment Band / Volume 71

D 82 (Diss., RWTH Aachen, 2006)

ISSN 1433-5530
ISBN-10: 3-89336-465-X
ISBN-13: 978-3-89336-465-7

Abstract

The relevance of aquifer heterogeneity for flow and transport is broadly recognized. A characterization of aquifer properties and the local flow and transport processes is obviously hampered by the inaccessibility of the subsurface. To optimize the characterization of the spatial and temporal variability of transport in a heterogeneous aquifer tracer experiments were carried out. Monitoring tracer plumes during tracer tests solely with a grid of multilevel observation wells is often problematic due to large changes of concentrations over small distances. Using geo-electrical imaging methods concentration distributions can be mapped over a wide area. At the Krauthausen test site (Germany) two large-scale tracer experiments in a heterogeneous aquifer were conducted to investigate the potentiality of Electrical Resistivity Tomography (ERT) for imaging subsurface transport. Down-gradient to the tracer injection the breakthrough in three image planes, two planes perpendicular and one parallel to the mean flow direction, was monitored with ERT. First, a $CaCl_2$ tracer solution with a higher electrical conductivity than the groundwater was injected. One year later, the same experiment was repeated using a so-called ‘negative’ tracer with a lower conductivity than the groundwater. The conduction of two consecutive large-scale tracer experiments under similar boundary conditions and the application of a 'positive' tracer with density effects and a 'negative' tracer with lower density than the natural groundwater are the outstanding features of this work.

With ERT changes in bulk electrical conductivity of the aquifer were monitored. Using calibration relations derived in laboratory experiments on columns packed with aquifer sediment, the bulk electrical conductivity measured with ERT was related to solute electrical conductivities measured with multilevel samplers (MLS). Although the injection well was screened over the entire aquifer thickness, both tracers were found in the middle and bottom part of the aquifer but not in the upper part where a high transport velocity was expected. The effect of density driven flow was clearly visible for the 'positive' tracer which showed a tendency towards the aquifer bottom boundary where it was spread out laterally. With ERT about 70 % of the injected tracer mass was recovered at the first cross section. The comparison between ERT and groundwater sampling showed that resistivity tomograms are an appropriate surrogate for traditional concentration maps at the Test site Krauthausen. Furthermore they allow the characterization of transport in heterogeneous aquifers with such a high spatial and temporal resolution that is otherwise impossible to obtain.

The spatial variability of the transport processes in a heterogeneous aquifer is caused by the spatial variability of the hydraulic conductivity. Using cone penetration tests (CPT), the spatial distribution of a parameter that is related to the hydraulic conductivity was derived and empirical relations were used to derive the 3D distribution of the hydraulic conductivity in the tracer test zone. The 2D spatio-temporal information about the transport obtained with ERT in the image planes was compared with three-dimensional numerical flow and transport simulations using the TRACE and PARTRACE numerical models and an aquifer model based on cone penetration data. In order to compare the ERT and numerical simulation data sets, a stream tube model that represents transport in the aquifer by a set of 1D convection-dispersion processes was used. The images of the numerical simulated tracer breakthrough based on a deterministic aquifer model were in good accordance to the ERT images derived at the field tests for the middle and lower parts of the aquifer. In the upper part where high transport velocities and large tracer fluxes were expected, no tracer was observed in the field tests. The simulations reproduced a vertical zoning of the tracer plume that was similarly observed at the first cross section during the 'positive' and 'negative' tracer experiments at the field site. Based on the 1D stream tube model approach it was possible to quantify the aquifers heterogeneity. The simulations showed that CPT is a cost extensive and fast method to characterize the heterogeneity of the aquifer at the Test site Krauthausen.

Kurzfassung

Um die Ausbreitung von Schadstoffen im Boden und Grundwasser vorhersagen zu können, werden numerische Berechnungen zur Simulation der Transportprozesse durchgeführt. Für die Simulationen müssen die transportrelevanten Eigenschaften des Aquifers quantifiziert werden. Bei der Modellierung der Schadstoffmigration in porösen Medien werden im Allgemeinen die Transportmechanismen der Advektion, Dispersion und Diffusion betrachtet. Beim Transport durch den Aquifer unterliegen die Schadstoffe jedoch einer Vielzahl von Reaktionen, etwa in Form von Adsorption an der Gesteinsmatrix. Derartige Reaktionen verlaufen je nach Art des Schadstoffs oder der chemischen Eigenschaften des Grundwassers schnell oder langsam, reversibel oder irreversibel. Um die einzelnen Prozesse in ihrer Komplexität besser verstehen und voneinander differenzieren und die Transportvorhersagen von Modellrechnungen überprüfen zu können, werden im Feldmaßstab experimentelle Untersuchungen des Transports von gelösten Stoffen im Grundwasser durchgeführt. Das Forschungszentrum Jülich betreibt in diesem Zusammenhang das 10 km nordwestlich von Düren gelegene Testfeld Krauthausen, auf dem seit 10 Jahren Tracerversuche in einem oberflächennahen, heterogenen Grundwasserleiter durchgeführt werden. Auf dem 200 $\times$ 60 m großen Testfeld sind insgesamt 75 Grundwassermessstellen und ein Grundwasserbrunnen installiert, die bis in eine Tiefe von 11 bis 13 Meter unter der Geländeoberkante ausgebaut sind. 66 dieser Grundwassermessstellen sind mit Multilevelsamplern ausgestattet. Bei den Multilevelsamplern (MLS) handelt es sich um je 24 PE Schläuche pro Bohrung, die an der Außenseite der Filterrohre in einem Abstand von 30-35 cm angebracht sind und eine teufenabhängige Beprobung des Grundwassers ermöglichen. Zur Untersuchung des Stofftransports in einem heterogenen Aquifer werden auf dem Testfeld zusätzlich neue, nicht-invasive Messmethoden eingesetzt. Bei den nicht-invasiven Verfahren handelt es sich um die elektrische Widerstandstomografie (ERT), die räumlich hoch aufgelöst elektrische Leitungseigenschaften des Untergrundes darstellt, die mit fluss- und transportrelevanten physikochemischen, strukurellen und hydraulischen Eigenschaften des Aquifers in Beziehung gesetzt werden können. Für die Verwendung geoelektrischer Verfahren zum Monitoring von hydrologischen Prozessen im Untergrund liegen zahlreiche Veröffentlichungen vor. In den letzten Jahren wurden durch verbesserte Methoden bei den Inversionsrechnungen erfolgreiche Einsatzmöglichkeiten im Hinblick auf eine qualitative tomografische Erfassung von Fluidbewegungen im Untergrund gezeigt. Es ist darüber hinaus auch möglich, aus den geoelektrischen Messdaten der ERT quantitativ Konzentrationsverteilungen beim Stofftransport im Untergrund abzuschätzen. Der Vorteil der tomografischen Messverfahren liegt darin, dass der Aquifer hinsichtlich der Ausbreitung eines Tracers nicht nur anhand lokaler Beobachtungspunkte verfolgt wird, sondern in seiner gesamten Mächtigkeit dreidimensional erfasst werden kann.

Im Rahmen der vorliegenden Arbeit wurden auf dem Testfeld Krauthausen in aufeinander folgenden Jahren zwei Tracerversuche im großen Feldmaßstab und unter hohem logistischem Aufwand durchgeführt. Besonders hervorzuheben ist das aufwendige

Injektionsverfahren bei beiden Versuchen. Die Einleitung wurde kontinuierlich über eine Woche durchgeführt, um trotz insgesamt niedriger Injektionskonzentrationen den Tracerdurchbruch in größeren Entfernungen zum Einleitbrunnen mittels ERT und MLS verfolgen zu können. Dabei wurden die Tracerlösungen in beiden Jahren auf dem Feld produziert und kontinuierlich über 7 Tage und Nächte eingeleitet. Die Ausbreitung der beiden Tracerwolken wurde durch kombinierte Grundwasserbeprobung und ERT-Messungen an Referenz-Profilen verfolgt. Bei dem ersten Versuch, im Jahr 2002, wurde als konservativer Tracer eine Salzlösung verwendet, die eine um den Faktor 6 erhöhte Leitfähigkeit gegenüber der natürlichen Leitfähigkeit des Grundwassers aufwies. Bei dem zweiten Tracerversuch, der im darauf folgenden Jahr (2003) bei ähnlichen Randbedingungen durchgeführt wurde, kam ein "Negativ"-Tracer zum Einsatz. Bei dem so genannten "Negativ"-Tracer handelte es sich um ein Wasser mit einer niedrigeren Salzkonzentration und vierfach niedrigeren elektrischen Leitfähigkeit als die des Grundwassers. Beide Tracer ermöglichten den Einsatz der nicht-invasiven elektrischen Widerstandstomografie. Zwei Referenz-Profile quer zur Grundwasserfließrichtung und ein Referenz-Profil in Grundwasserfließrichtung wurden mit Oberflächen- und Bohrlochelektroden zur Überwachung der Tracerausbreitung ausgestattet. Die Durchführung zwei aufeinander folgender Tracerversuche im Feldmaßstab unter vergleichbaren Randbedingungen ist ein Alleinstellungsmerkmal der vorliegenden Arbeit. Es gibt bisher in der Literatur keine Veröffentlichungen zu Feldversuchen, bei denen als Tracer ein Wasser eingesetzt wurde, dessen elektrische Leitfähigkeit geringer als die natürliche elektrische Leitfähigkeit des Grundwassers war.

Mit ERT wird die so genannte "bulk" oder totale elektrische Leitfähigkeit gemessen, d.h. die elektrische Leitfähigkeit des Grundwassers und der umgebenden Gesteinsmatrix. Mit der MLS-Methode werden direkt Proben des Grundwassers aus verschiedenen Tiefen gewonnen. Um beide Messungen miteinander vergleichen zu können, wurden im Labor Säulenversuche mit Aquifersediment durchgeführt. Anhand dieser Kalibrationsversuche war es möglich, eine lineare Beziehung zwischen der totalen Leitfähigkeit von Gestein und wässriger Lösung und der Leitfähigkeit der wässrigen Lösung alleine abzuleiten, die die Umrechnung von totaler zur Leitfähigkeit der wässrigen Lösung und umgekehrt ermöglicht. Auf diese Weise konnten beide Methoden qualitativ und quantitativ miteinander verglichen werden.

Beim ersten Versuch kam es trotz der kontinuierlichen Einleitung einer gering konzentrierten Salzlösung zu einem dichtebedingten Absinken des Tracers in Richtung der Aquiferbasis. Durch den Einsatz des „Negativ“-Tracers beim zweiten Versuch wurde das dichteabhängige Absinken der Tracerlösung vermindert und somit die Beschaffenheit und Heterogenität des Grundwasserleiters über eine größere Mächtigkeit erfasst. Dennoch wurde bei beiden Versuchen keine Tracerlösung im obersten Aquiferbereich gefunden, in dem, basierend auf der Kenntnis der hydraulischen Durchlässigkeit der lithologischen Schichten, die höchsten Fließgeschwindigkeiten vermutet werden.

Die Daten, die mittels des ERT- und MLS-Monitorings gewonnen wurden, wurden mit Hilfe eines eindimensionalen effektiven Stromlinienröhren-Modells hinsichtlich der Heterogenität der effektiven Transportparameter charakterisiert und quantifiziert. Bei genauem Vergleich beider Versuche bezüglich der räumlichen Verteilung der effektiven Transportparameter zeigte die ERT-Methode eine größere Reproduzierbarkeit als die MLS-Methode. Insgesamt konnten aber lokal gute Übereinstimmungen von ERT und MLS beobachtet werden.

Für das erste Referenz-Profil wurde darüber hinaus die mittels ERT Messungen wiedergefundene Tracermasse für beide Versuche bestimmt. Beim Salztracerversuch 2002 wurden 69 % der injizierten Tracermasse wieder gefunden, beim "Negativ"-Tracertest waren es 68 %. Die Tracermasse am zweiten Referenz-Profil konnte nur für den "Negativ"-Tracertest berechnet werden. Aufgrund der insgesamt geringeren ERT-Auflösung im Bereich des zweiten Referenz-Profils konnten nur 14 % der injizierten Tracermasse per Massenbilanz bestimmt werden.

Im Anschluss an die Tracerversuche wurden numerische Simulationen durchgeführt. Ziel der Simulationen war es, die Versuche auf dem Testfeld Krauthausen zu reproduzieren. Voraussetzung dafür ist die genaue Kenntnis der Heterogenität des Aquifers. Die räumliche Variabilität der Transportprozesse in einem heterogenen Aquifer wird durch die Variabilität der hydraulischen Leitfähigkeit im Untergrund bestimmt. Mit Hilfe von Spitzendrucksondierungen, auch Cone Penetration Tests (CPT) genannt, kann die hydraulische Leitfähigkeit eines Gesteins relativ schnell und kostengünstig in oberflächennahen Grundwasserleitern bestimmt werden. Solche CPT Messungen wurden auf dem Testfeld Krauthausen hoch aufgelöst durchgeführt, um eine dreidimensionale Verteilung der hydraulischen Leitfähigkeit für das zentrale Testfeld abzuleiten. Mit Hilfe dieser Daten konnte ein deterministisches Aquifermodell konstruiert und in die Fluss- und Transportsimulationen implementiert werden. Das dreidimensionale Fließfeld wurde mit dem Finite Elemente Modell TRACE berechnet, der Transport mit dem "particle-tracking" Modell PARTRACE. Um die Ergebnisse nicht nur qualitativ sondern auch quantitativ mit den Tracertests vergleichen zu können, wurden die Simulationsergebnisse ebenfalls mit einem eindimensionalen effektiven Stromlinienmodell bezüglich der Heterogenität der Transportparameter charakterisiert.

Der Vergleich der Simulationen mit den Feldversuchen zeigte generell gute Übereinstimmung bezüglich der Heterogenität der Transportprozesse im Aquifer. Allerdings fließt im Modell ein Hauptteil der Tracersubstanz durch den obersten Aquiferbereich, für den eine sehr hohe hydraulische Leitfähigkeit mittels Spitzendrucksondierung bestimmt wurde. In dieser hochleitfähigen Schicht wurde in keinem der beiden Feldversuche Tracerlösung detektiert. Es ist zu vermuten, dass dieser Bereich bei den Versuchen nicht erfasst wurde, da die Injektionsbohrung erst ab 3 m unter Geländeoberkante verfiltert ist und sich die Unterkante dieser leitfähigen Schicht ebenfalls bei 2.5 bis 3 m unter Geländeoberkante befindet. Darüber hinaus ist anzunehmen, dass die mittels Spitzendrucksondierung abgeleitete Durchlässigkeit dieser Schicht insgesamt zu hoch bestimmt wurde. Aktuelle Permeameter-Versuche an Sediment aus dieser Tiefe deuten auf eine geringere hydraulische Leitfähigkeit hin.

Der Vergleich der effektiven Transportparameter zeigte insgesamt höhere effektive Geschwindigkeiten für die Simulationen, was auf die hochleitfähige Schicht im oberen

Aquiferbereich zurückzuführen ist, die bei den Feldversuchen nicht erfasst wurde. Bei Betrachtung der räumlichen Verteilung und der Magnituden der Transportparameter konnte insgesamt eine gute Übereinstimmung beobachtet werden. Die Simulationsergebnisse zeigen, dass die Spitzendrucksondierung bzw. CPT-Methode ein geeignetes Verfahren ist, um kostengünstig und schnell die Heterogenität des oberflächennahen Aquifers zu bestimmen.

Danksagung

Liebe Leute. Die Danksagung. Früher habe ich immer gesagt, Danksagungen sind blöd, mach' ich nicht, sind ja doch nur Standardfloskeln, meint doch 'eh keiner ernst. Aber nach nun fast vier Jahren spüre ich doch ein ganz echtes und tiefes Bedürfnis, Danke zu sagen. Denn ohne die vielen Menschen, die mich unterstützt haben, wäre diese Arbeit nie zu Stande gekommen. Dann mal los:

Zunächst möchte ich ganz herzlich meinen Referenten danken. Herrn Prof. Dr. Harry Vereecken, Leiter des Instituts Agrosphäre ICG IV, danke ich für die Möglichkeit, am Forschungszentrum Jülich unter den besten Bedingungen, die man sich als Doktorandin wünschen kann, zu promovieren. Außerdem waren die Diskussionen in den Doktorandenseminaren enorm motivierend für den Fortschritt der eigenen Arbeit. Bei Herrn Prof. Dr. Jan Vanderborght bedanke ich mich für die intensive Betreuung während meiner gesamten Zeit, die vielen bereichernden Diskussionen und dafür, dass er mir das Gefühl gegeben hat, dass jede Frage erlaubt ist. Herrn Prof. Dr. Thomas R. Rüde danke ich aufrichtig für die Übernahme des Referats und seine aufmerksame und intensive Auseinandersetzung mit den Inhalten meiner Dissertation.

Am Institut Agrosphäre sowie an anderen Instituten des Forschungszentrums Jülich bin ich so vielen Menschen unendlich dankbar, ohne die die Tracerversuche im großen Maßstab kaum möglich gewesen wären. Leider würde eine Seite niemals ausreichen, um jedem Einzelnen meinen Dank auszusprechen. Dennoch möchte ich wenigstens Einige namentlich erwähnen. Meinem Kollegen und Zimmernachbarn Dr. A. Englert danke ich für die tatkräftige Unterstützung auf dem Feld, die vielen informativen Gespräche und dass er jederzeit ein offenes Ohr für meine Fragen hatte (und natürlich für die selbst gedrehten Gelegenheits-Protest-Zigaretten zwischendurch). Für den uneingeschränkt reibungslosen und erfolgreichen Ablauf der beiden Tracerversuche waren H. G. Sittardt, R. Harms, O. Esser und A. Langen unverzichtbar. Vielen Dank für den oft über die Arbeitszeiten hinausgehenden Einsatz! Damit wäre ich auch schon bei den "Schichtarbeitern" des ICG IV, die mich Tag und Nacht auf dem Feld bei den Versuchen und im Anschluss beim Monitoring unterstützt und äußerst gut verpflegt haben. Danke! Für die gute Zusammenarbeit bei den ERT-Messungen und Grundwasserbeprobungen möchte ich A. Verweerd, H. M. Münch, K. Gössling und K. Borgers danken. A. Kemna und A. Tillmann danke ich ebenfalls für ihre Unterstützung von der geophysikalischen Seite. H. Hardelauf sage ich Danke, dass er immer Zeit und viel Geduld für meine Fragestellungen hinsichtlich der Simulationen hatte. Den Herren Administratoren T. Schuster und J. Heidbüchel danke ich für zahlreiche "Notfall-Hilfe" bei mehr oder minder gravierenden EDV-Komplikationen, wie zum Beispiel ertrunkene Tastaturen oder ein laut explodierendes Netzteil mit traumatisierenden Folgen für die entsetzte Simulantin. Für fachliche Gespräche in lockerer Atmosphäre und ein sehr angenehmes Arbeitsklima danke ich außerdem den Schwimmern, Ums-Forschungszentrum-Läufern, Kaffeetrinkern, Doch-immer-noch-Rauchern, Bananenessern etc., um nur Einige der Spezies zu nennen. Wenn das die Forschung nicht nach vorne bringt! Zum Schluss danke ich meinen Eltern für ihre Geduld und ihre Unterstützung.

Contents

List of Figures

List of Tables

List of Abbreviations and Symbols

Instruments, Materials, Others

BTC	Breakthrough Curves
CDE	Convection Dispersion Equation
CPT	Cone Penetration Tests
EC	Electrical Conductivity
ERT	Electrical Resistivity Tomography
MLS	Multilevel Samplers

Space Indices

$\boldsymbol{x}$	horizontal transversal direction
$\boldsymbol{y}$	longitudinal direction, mean flow direction
z	vertical transversal direction

Physical Symbols

$\mathbf{A_p}$	Jacobian matrix
a	empirical formation factor [$\mu S\cdot cm^{-1}$]
b	empirical intercept [-]
C	solute concentration [$kg\cdot m^{-3}$]
C_0	initial tracer concentration [$kg\cdot m^{-3}$]
C^r	resident or volume averaged concentration [$kg\cdot m^{-3}$]
C^f	flux averaged concentrations [$kg\cdot m^{-3}$]
C_{ini}	background concentration [$kg\cdot m^{-3*}$]
c	normalized solute concentration [d^{-1}]
c_r	mechanic cone pressure [MPa]
D	effective diffusion-dispersion coefficient [$m^2\cdot d^{-1}$]
D_d	local scale dispersion tensor [$m^2\cdot d^{-1}$]
$D*$	effective diffusion coefficient accounting for tortuosity of the flow paths [$m^2\cdot d^{-1}$]

$\mathbf{D_{eq}}$	equivalent dispersion tensor [$m^2 \cdot d^{-1}$]
d	transfer resistance [Ω]
d_{20}	grain size diameter for a cumulative grain size distribution of 0.20 [mm]
d^m	effective coefficient of molecular diffusion [$m^2 \cdot d^{-1}$]
EC_b	bulk electrical conductivity [$\mu S \cdot cm^{-1}$]
EC_w	absolute electrical conductivity [$\mu S \cdot cm^{-1}$]
F	formation factor for the EC_b - EC_w relation
f	forward model operator of the Poisson equation
f	formation factor to calculate the tracer mass [($kg \cdot m^{-3}$) ($cm \cdot \mu S^{-1}$)]
f_T	temperature correction factor
g	acceleration of gravity [$m \cdot s^2$]
$H(t)$	Heaviside function
I	electrical current [A]
K	hydraulic conductivity [$m \cdot d^{-1}$]
M	tracer mass [kg]
m	parameter vector representing $\log_e$ transformed electrical conductivities
N	number of data
n	porosity [-]
n_e	effective porosity [-]
n, m, α_1	van Genuchten parameters [-], [-], [-]
p	groundwater pressure [hPa]
q	volumetric flow rate [$m \cdot d^{-1}$]
R	matrix evaluating the roughness of **m**
R_i	magnitude of measured resistance
r	data vector of the $\log_e$ transformed resistances
S_s	specific storage coefficient [m^{-1}]
S	effective saturation [-]
T	temperature [°C]
T_0	area under a solute breakthrough curve [$kg \cdot m^{-3} \cdot d$]
t	simulation time [d]
t_0	solute application time [d]
U	large scale uniform advection velocity [$m \cdot d^{-1}$]
W	weighting matrix
N	number of data
α	elastic compressibility coefficient of the porous formation [m^2 N^{-1}]
α_r	regularisation parameter [-]

α_T	temperature coefficient [°C^{-1}]
β	compressibility coefficient of the fluid [m^2 N^{-1}]
γ	gamma activity [counts min^{-1}]
δ_{ij}	Kronecker's Delta
δ	Dirac Delta function
ε_i	data error
$\varepsilon_{\min}$	minimum error
ε_{Ri}	increase in ε_i
θ	volumetric moisture content [Vol.-%]
θ_s	saturated water content [Vol.-%]
θ_r	residual water content [Vol.-%]
λ	Fourier transform variable
λ_{adv}	advective dispersivity [m]
λ_{eq}	equivalent dispersivity [m]
λ_s	stream tube dispersivity [m]
λ_L	longitudinal local dispersivity [m]
λ_T	transversal local dispersivity [m]
μ_t	average of the solute travel times [d]
ν	average flow velocity [m·d^{-1}]
v_{eq}	equivalent velocity [m·d^{-1}]
v_s	stream tube velocity [m·d^{-1}]
ρ	bulk soil electrical resistivity [Ωm]
$\rho_{(ini)}$	initial background bulk soil electrical resistivity [Ωm]
ρ_b	bulk density of the porous formation [kg·m^{-3}]
ρ_w	water density [kg·m^{-3}]
σ_t^2	variance of the solute travel times [d]
τ	tortuosity [-]
τ_1	first temporal moment of travel time distribution [d]
τ_2	second temporal moment of travel time distribution [d^2]
Φ	electric potential [V]
$\Psi(\mathbf{m})$	objective function
$\Psi_{diff}(\mathbf{m})$	objective function for the difference inversion approach
$\Psi_d(\mathbf{m})$	data misfit
ξ	stream tube coordinate [m]

1 Introduction

Groundwater is an important resource that is running short as a cause of increasing water consumption due to an exponential growth of the world wide population and contamination due to the successive intensification in industry and agriculture. The evaluation of the risk assessment of potentially hazardous substances in soils and groundwater implies detailed knowledge about the spatial and temporal variation of transport relevant properties of the subsurface. This requires the application of appropriate methods to characterize subsurface flow and transport processes with minimal disturbance.

The application of geophysical methods to characterize the subsurface structure and heterogeneity is well documented in literature since many years (e.g. Reynolds, 1997). In recent years geophysical methods are increasingly being used to monitor subsurface fluid movement (e.g. Daily et al., 1992). Geophysical tomographic methods, like the Electrical Resistivity Tomography (ERT) have the advantage that subsurface processes are mapped continuously. A number of studies improved the potential of ERT for monitoring tracer experiments in shallow aquifers because the spatial resolution that is obtained with classical groundwater sampling methods is lower determined in the lateral direction by the distance between local boreholes (e.g. Kemna et al., 2002, Singha et al., 2003).

One objective of this study is to investigate the potential of ERT to obtain spatio-temporal information about tracer transport across reference planes in a heterogeneous aquifer. Two tracer experiments were conducted at the test site Krauthausen in the years 2002 and 2003. In 2002, a so called 'positive' tracer, which was a calcium chloride solution with a factor 6 higher electrical conductivity than the natural groundwater was injected. In 2003, a 'negative' tracer, water with a factor 4 lower electrical conductivity compared to the groundwater, was injected. Two tracer tests were carried out under similar boundary conditions to (i) evaluate the effect of density driven flow on tracer transport and the characterization of tracer transport in a heterogeneous aquifer, and to (ii) verify to what extend the results of a tracer test are reproducible. The tracer breakthrough was monitored with ERT at two cross sections perpendicular to the main flow direction and one profile parallel to the flow direction. Besides ERT, groundwater samples were taken at multilevel observation wells to compare ERT with conventional tracer monitoring methods. The tracer breakthrough patterns monitored with ERT and MLS were parameterized by means of a 1D stream tube model approach. The stream tube model (STM) represents transport in the aquifer by a set of 1D convection dispersion processes. Heterogeneity of transport is represented by the variability of advection velocities within the population of stream tubes. Mixing is represented by an equivalent local longitudinal dispersion process within the stream tubes (Vanderborght and Vereecken, 2001). The tracer mass recovered with ERT at the cross sectional planes during the two tracer experiments was quantified by means of a mass balance.

Another objective, focused on in this study is to simulate the tracer tests based on a deterministic aquifer model. The aquifer model was derived using information gained from Cone Penetration Tests (CPT) performed at the Krauthausen test site to characterize the heterogeneity of the aquifer by a three-dimensional hydraulic conductivity distribution. The simulations were done using the numerical flow and transport models TRACE/PARTRACE. Natural boundary conditions derived from hydraulic head measurements at the test site during the field experiments were implemented by Dirichlet boundary conditions. The results of the simulations were compared with the ERT images of the 'positive' and 'negative' tracer tests and parameterized based on a 1D stream tube model approach.

2 Theory

2.1 Flow in Porous Media

The basic processes determining groundwater flow in porous media can be explained by Darcy's law. Darcy's law was established in 1856 by Henry Darcy. It is valid for homogeneous and heterogeneous media provided that conditions with laminar flow are complied. Darcy's law may be written as:

$$\mathbf{q} = -\mathbf{K}\nabla h \qquad \text{Eq. 2-1}$$

where **q** is the volumetric flow vector, **K** is the hydraulic conductivity tensor and ∇h is the gradient of the hydraulic head.

It should be noted that **q** has the dimension of velocity and is called *darcian velocity*. This term is not the same as the average flow velocity. The average flow velocity is given by:

$$v = \mathbf{q} / n_e \qquad \text{Eq. 2-2}$$

where n_e is the effective porosity.

Another fundamental law governing groundwater flow is the continuity equation, which expresses the principle of mass conservation. Considering an elementary control volume of soil centered around a point with Cartesian coordinates, the mass of groundwater M present in an elementary control volume is given by:

$$M = \rho_w \theta \Delta x \Delta y \Delta z \qquad \text{Eq. 2-3}$$

where θ is the volumetric moisture content of the porous medium and ρ_w is the density of water. This quantity of water can change when groundwater enters or leaves the control volume. The principle of mass conservation implies that the net result of inflow minus outflow is balanced by the change in storage versus time and may be written as:

$$\frac{dM}{dt} = in.flow - out.flow \qquad \text{Eq. 2-4}$$

The amount of groundwater flow is denoted by means of the flux **q** which is the volumetric discharge or flow rate per cross-sectional area. Under the assumption that density effects can be neglected the continuity equation may be written:

$$\left[\theta(\alpha+\beta)\frac{\partial p}{\partial t} + \frac{\partial \theta}{\partial t}\right] = -\nabla \mathbf{q} \qquad \text{Eq. 2-5}$$

where α is the elastic compressibility coefficient of the porous formation, β is the compressibility coefficient of water and p presents the groundwater pressure. In this simplified form, the continuity equation expresses the groundwater balance on a volumetric basis. The left-hand side of the equation represents the change in volume of groundwater in a representative volume of the porous medium. The right-hand side of the equation represents the convergence or divergence of the volumetric flow rate of groundwater (Delleur, 1999).

The groundwater flow equation is obtained by combining the continuity equation with Darcy's Law:

$$\left[\theta(\alpha+\beta)\frac{\partial p}{\partial t} + \frac{\partial \theta}{\partial t}\right] = \nabla(\mathbf{K}\nabla h). \qquad \text{Eq. 2-6}$$

Considering that groundwater flow occurs under saturated conditions the water content equals the porosity, and under the assumption of incompressible solid grains the change in porosity can be related to the compression of the porous medium, which depends upon the water pressure or groundwater potential. Thus, the continuity equation for saturated conditions may be written as:

$$S_s \frac{\partial h}{\partial t} = \nabla \cdot (\mathbf{K}\nabla h) \qquad \text{Eq. 2-7}$$

where S_s is the specific storage coefficient, depending only upon compressibility of the porous medium and the fluid

$$S_s = pg(\alpha + n\beta) \qquad \text{Eq. 2-8}$$

where g is the acceleration of gravity and n the porosity (Delleur, 1999).

For unsaturated flow conditions the relationship between moisture content θ, pressure head h and hydraulic conductivity **K** need to be specified. One commonly used approach was developed by van Genuchten (1980) and Mualem (1977). The effective saturation S is defined:

$$S = \frac{\theta - \theta_r}{\theta_s - \theta_r} = \left(1 + (\alpha_1 \cdot h)^n\right)^{-m} \qquad \text{Eq. 2-9}$$

where θ_r is the residual water content, θ_s is the saturated water content and n, m and α_1 are the van Genuchten parameters,

$$K(S) = \mathbf{K} \cdot S^{\tau} \cdot \left(1 - \left[1 - S^{\frac{1}{m}}\right]^m\right)^2 \qquad \text{Eq. 2-10}$$

where $m = 1 - 1/n$ and τ is the tortuosity.

When groundwater flow is stationary, the variables on the left-hand side of the Richard's equations become independent of time. Thus, the groundwater flow equation reduces to:

$$\nabla(\mathbf{K}\nabla h) = 0\,. \qquad \text{Eq. 2-11}$$

2.2 Solute Transport

To predict solute transport in a saturated porous medium the fluid velocity needs to be described. The flux of fluid over a macroscopic cross section of the porous medium has been experimentally shown to follow Darcy's law. The average flow velocity ν which is defined by the fluid flux divided by the water-filled porosity (cp Eq. 2-2) represents the macroscopic average of the pore scale velocities. There are however different processes affecting the variability of the pore scale fluid velocity e.g. the no slip-condition, which renders the fluid velocity zero at the solid surfaces, the complex pore scale geometry and interconnections between pores, and the variability of pore sizes (Delleur, 1999). The effects of molecular diffusion and the microscopic variations of fluid velocity on solute transport are represented by the so called local hydrodynamic dispersion.

Transport of a non-reactive tracer in the three-dimensional flow field $\mathbf{q}(\mathbf{x})$ is described using the convection dispersion equation (CDE) and may be expressed by:

$$\theta(\mathbf{x})\frac{\partial C(\mathbf{x},t)}{\partial t} = -\mathbf{q}(\mathbf{x})\nabla C(\mathbf{x},t) + \nabla[\theta(\mathbf{x})D_d(\mathbf{x})\nabla C(\mathbf{x},t)] \qquad \text{Eq. 2-12}$$

where $C(\mathbf{x},t)$ is the solute resident concentration in the liquid phase, and $D_d(\mathbf{x})$ is the local scale dispersion tensor. According to Bear (1972) the dispersion tensor is defined:

$$D_{d,ij}(\mathbf{x}) = \left(\alpha_T\sqrt{\nu_i\nu_j} + d^m\right)\delta_{ij} + \frac{(\lambda_L - \lambda_T)}{\sqrt{\nu_i\nu_j}}\nu_i\nu_j \qquad \text{Eq. 2-13}$$

where $\sqrt{\nu_i\nu_j}$ is the average water velocity magnitude, λ_L is the longitudinal local dispersivity,

λ_T is the transverse local dispersivity, d^m is the effective coefficient of molecular diffusion in the porous medium, and δ_{ij} is the Kronecker's Delta ($\delta_{ij} = 0$ for $i \neq 1$ and $\delta_{ij} = 1$ for $i = j$). The values of λ_T, λ_L and d^m need to be determined experimentally (Delleur, 1999).

Molecular diffusion is a very slow mechanism and the importance of diffusion increases with decreasing flow velocities. Concerning transport in porous media in this case study at the test site Krauthausen the impact of molecular diffusion can be neglected.

2.3 Equivalent Transport Models

2.3.1 Characterization of Transport Processes

Groundwater flow and transport in the subsurface is a complex, three-dimensional, heterogeneous setting. The heterogeneity of the aquifer which causes a high variability in flow velocities at the macroscopic scale can be described accurately only through careful hydrogeologic practice in the field. However, regardless of how much data are collected uncertainty remains. Stochastic approaches have resulted in many significant advances in characterizing subsurface heterogeneity and dealing with uncertainty.

Transport processes in groundwater can be characterized by spatial moment analysis of a solute plume evolution (Dagan, 1984, Neumann et al., 1987) or temporal moment analysis of solute breakthrough curves (BTC) (Dagan and Nguyen, 1989). The first method describes transport in terms of the positions of solute particles or the spatial distribution of solute concentrations at fixed times and with the second method arrival times of solutes or the temporal evolution of solute fluxes at fixed reference planes are determined (Simmons, 1982, Shapiro and Cvetkovic, 1988, Cvetkovic and Shapiro, 1989, Dagan et al., 1992). Spatial moment analysis of solute transport requires a high spatial resolution of observation points. Thus, the analysis of solute arrival times is commonly used if the spatial resolution of observation points is limited.

For the characterization of three-dimensional transport processes in heterogeneous aquifers equivalent transport models and parameters are used. On the basis of equivalent models locally measured BTCs can be up-scaled to transport processes at larger scales and to a travel time distribution which is representative for the aquifer.

2.3.2 Derivation of Equivalent Transport Parameters from Field Tracer Tests

3D solute transport in porous media can be described by the so-called equivalent convection-dispersion model. This model characterizes ensemble averaged concentrations by assuming a hydrodynamically uniform medium with a large scale uniform advection velocity $\mathbf{U}$ and an equivalent dispersion tensor $\mathbf{D}_{\mathbf{eq}}$. The ensemble averaged concentrations are given by:

$$\frac{\partial \langle C(\mathbf{x},t)\rangle}{\partial t} = -\mathbf{U}\nabla\langle C(\mathbf{x},t)\rangle + \mathbf{D_{eq}}\nabla^2\langle C(\mathbf{x},t)\rangle \qquad \text{Eq. 2-14}$$

The ensemble averaged concentrations can either be defined as the ensemble resident or volume averaged concentrations $\langle C^r(\mathbf{x},t)\rangle$ which represent the average of the local concentrations in all realizations of the second order stationary random field or $\langle C(\mathbf{x},t)\rangle$ represents the ensemble flux averaged concentration $\langle C^f(\mathbf{x},t)\rangle$ which is given by the average of the local solute fluxes divided by the average of the local water fluxes. $\langle C^r(\mathbf{x},t)\rangle$ is related to a solute particle location probability distribution whereas $\langle C^f(\mathbf{x},t)\rangle$ relates to a distribution of particle travel times (Vanderborght et al., 2005).

Assuming that a stationary hydraulic conductivity field with a uniform mean flow field is given and the extent of the solute plume in the direction perpendicular to the mean flow direction is much larger than the spatial correlation scale of the hydraulic conductivity then $\langle C(\mathbf{x},t)\rangle$ is constant in a plane perpendicular to the mean flow direction x_1. Under these conditions the large-scale transport can be expressed as an one-dimensional process and the equivalent dispersion model is then defined as:

$$\frac{\partial \langle C(x_1,t)\rangle}{\partial t} = -U_1\frac{\partial \langle C(x,t)\rangle}{\partial x_1} + D_{1eq}\frac{\partial^2 \langle C(x_1,t)\rangle}{\partial x_1^2} \qquad \text{Eq. 2-15}$$

where U_1 is the mean pore water velocity and D_{1eq} is the equivalent dispersion tensor, which is expressed by the product of the equivalent dispersivity λ_{eq} and the mean pore velocity U_1 (Vanderborght et al., 2005). For smaller travel distances the equivalent convection dispersion model must be interpreted as a tool to describe and parameterize a locally measured breakthrough curve as a result of a one-dimensional equivalent convective dispersive process in a hydro-dynamically uniform medium.

A problem with the application of Eq. 2-15 for the analysis of real solute plumes is that the width of the solute plume or its lateral extensions are not sufficiently large so that the ensemble averaged concentration is not constant in the reference plane but decreases with increasing lateral distance from the expected center of mass of the plume. As a consequence, the ensemble averaged concentration cannot be inferred from the spatial average of the solute concentration in a reference plane.

As an alternative to the equivalent dispersion model (cp. Eq. 2-15), a stochastic stream tube model can be used to account for heterogeneity of flow and transport in aquifers. The stream tube approach describes transport by a set of independent stream tubes parallel to the mean flow direction. Transport through a stream tube is represented by a simple 1D convection dispersion process model whose parameters are constant and each tube is isolated from adjacent tubes (Jury and Roth, 1990). Locally measured solute concentrations at a certain point $C(\mathbf{x},t)$ are interpreted to be the result of a 1D convection dispersion process in a stream tube, which connects the injection point with the location $\mathbf{x}$. The 1D stream tube transport may be written as:

$$\frac{\partial C(\xi,t)}{\partial t} = -v_S(\mathbf{x})\frac{\partial C(\xi,t)}{\partial \xi} + v_S(\mathbf{x})\lambda_S(\mathbf{x})\frac{\partial^2 C(\xi,t)}{\partial \xi^2} \qquad \text{Eq. 2-16}$$

where v_S and λ_S are the stream tube velocity and the stream tube dispersivity, respectively, and ξ is the stream tube coordinate (Vanderborght et al., 2005). The variability of v_S across a reference plane is a measure of plume distortion as a result of spatial variations of water flow. The average value of λ_S represents the dilution of the locally observed concentrations due to mixing along the stream tube trajectory.

To derive the stream tube model parameters, two approaches were used. In the first approach, the time moments of the locally measured BTCs were calculated. The first two temporal moments of a BTC measured at location $\mathbf{x}$ are defined as:

$$\tau_1(\mathbf{x}) = \int_0^\infty t c(\mathbf{x},t)dt \qquad \text{Eq. 2-17}$$

$$\tau_2(\mathbf{x}) = \int_0^\infty t^2 c(\mathbf{x},t)dt \qquad \text{Eq. 2-18}$$

where $c(\mathbf{x},t)$ is the normalized concentration at location $\mathbf{x}$ and time t, which is defined as:

$$c(\mathbf{x},t) = \frac{C(\mathbf{x},t)}{\int_0^\infty C(\mathbf{x},t)dt} = \frac{C(\mathbf{x},t)}{T_0(\mathbf{x})} \qquad \text{Eq. 2-19}$$

where $T_0(\mathbf{x})$ is the area under the BTC measured at location $\mathbf{x}$.

If the solute mass is injected instantaneously and if flux-averaged concentrations are given, $c(\mathbf{x}, t)$ represents a distribution of solute travel times from the injection point to location $\mathbf{x}$. The average solute travel times $\mu_t(\mathbf{x})$ and the variance of the solute travel times $\sigma_t^2(\mathbf{x})$ are related to $\tau_1(\mathbf{x})$ and $\tau_2(\mathbf{x})$ as:

$$\mu_t(\mathbf{x}) = \tau_1(\mathbf{x}) \qquad \text{Eq. 2-20}$$

$$\sigma_t^2(\mathbf{x}) = \tau_2(\mathbf{x}) - \tau_1^2(\mathbf{x}) \qquad \text{Eq. 2-21}$$

The average and variance of the solute travel times can be used to determine the 'equivalent' solute particle velocity $v_{eq}(\mathbf{x})$, and the 'equivalent' dispersivity $\lambda_{eq}(\mathbf{x})$, which characterize the BTC measured at location **x** (Jury and Sposito,1985):

$$v_{eq}(\mathbf{x}) = \frac{x_1}{\mu_t(\mathbf{x})} \qquad \text{Eq. 2-22}$$

$$\lambda_{eq}(\mathbf{x}) = \frac{\sigma_t^2(\mathbf{x}) x_1}{2\mu_t(\mathbf{x})^2}. \qquad \text{Eq. 2-23}$$

If solute mass is injected over a finite time period the injection can be described by a block input function. The first two temporal moments then can be defined as:

$$\mu_t = \frac{t_0}{2} + \frac{x}{v_1} \qquad \text{Eq. 2-24}$$

$$\sigma_t^2 = \frac{t_0^2}{12} + \frac{2xD_1}{v_1^3} \qquad \text{Eq. 2-25}$$

where $t_0 = T_0/C_0$. The first temporal moment μ_t represents the mean breakthrough time and σ_t^2 the variance for a block input (Leij and Dane, 1991).

In the second approach, the solution of the 1D convection dispersion equation is fitted to the locally measured breakthrough curve. The calculation of the flux concentration of the CDE corresponding to a step function input of solute is given by:

$$C(0,t) = C_0 H(t) \qquad \text{Eq. 2-26}$$

where $H(t)$ is the Heaviside function, the analytical solution of the 1D convective dispersive stream tube approach may be written as:

$$C(x_1,t) = \frac{C_0}{2}\left[erfc\left(\frac{x_1 - vt}{\sqrt{4Dt}}\right) + \exp\left(\frac{vx_1}{D}\right) erfc\left(\frac{x_1 + vt}{\sqrt{4Dt}}\right)\right] \qquad \text{Eq. 2-27}$$

where x_1 is the distance to the injection point and C_0 is the concentration of the solution that is injected. If C_0 is not known it can be fitted. Considering a field experiment where the concentration is injected over a certain time the one-dimensional convective dispersive stream tube transport process can be represented by the sum of a step input function and a negative step input which is shifted over a certain time and may be written as:

$$C(x_1,t) = \frac{C_0}{2}\left[erfc\left(\frac{x_1 - vt}{\sqrt{4Dt}}\right) + \exp\left(\frac{vx_1}{D}\right)erfc\left(\frac{x_1 + vt}{\sqrt{4Dt}}\right)\right] - w\frac{C_0}{2}\left[erfc\left(\frac{x_1 - vtc}{\sqrt{4Dt}}\right) + \exp\left(\frac{vx_1}{D}\right)erfc\left(\frac{x_1 + vtc}{\sqrt{4Dt}}\right)\right] \qquad \text{Eq. 2-28}$$

with the following constraints:

if $t \le 7$ then $w = 0$

if $t > 7$ then $tc = t - 7$ and $w = 1$ (Jury and Roth, 1990).

3 Characterization of Transport Processes in a Heterogeneous Aquifer Using Non-Invasive Measurement Techniques

3.1 Materials and Methods

In this section two tracer experiments conducted at the test site Krauthausen are described. In both experiments the same amount of tracer solution was injected at the same location in the aquifer. In the first experiment, a tracer with a higher electrical conductivity ('positive' tracer) was injected and in the second experiment, one with a lower electrical conductivity ('negative' tracer) was injected. The tracer tests were monitored using multilevel groundwater sampling (MLS) and Electrical Resistivity Tomography (ERT). The data collected during the field experiments were qualitatively compared with regard to the different behavior of the two tracer solutions within the heterogeneous aquifer and quantitatively in terms of equivalent, also called effective, transport parameters and mass recovery.

3.1.1 Experiment Description

3.1.1.1 Hydrogeological Setup

The test site Krauthausen is situated approximately 10 km northwest of the city of Düren and 6 km southeast of the FORSCHUNGSZENTRUM JÜLICH GmbH, Germany. A detailed description of the Krauthausen test site is given by Vereecken et al. (2000), Döring (1997) and Englert (2003). The field has an extension of 60 by 200 m. Geologically, it belongs to the southern part of the Lower Rhine Embayment. The upper aquifer system is composed of unconsolidated quaternary deposits, and a pseudogley soil at the top. The base of the aquifer is built up by thin layers of clay and silt and situated at a depth between 11-13 m below the surface. The variance of the log transformed hydraulic conductivity of the aquifer is estimated to be 1.3, and the spatial correlation in the horizontal and vertical direction 6.7 and 0.37 m, respectively (Döring, 1997). The overall total porosity resulting from total porosity measurements on 83 soil cores at nine locations at the test site Krauthausen is 26 % with a standard deviation of 6 % (Vereecken et al., 2000).

The main direction of the groundwater flow is towards NW with a hydraulic gradient of about 0.002, which remains fairly constant over time. The groundwater table shows significant seasonal variation ranging from 2.5 m to 1 m below surface in summer and winter, respectively.

3.1.1.2 Setup of the Test Site

To investigate water flow and transport in an aquifer, the test site was equipped with groundwater observation wells. The drillings for the observation wells were deepened using a dry rotary drilling method. One drilling has a diameter of 620 mm, all other drillings have a diameter of 324 mm (Englert, 2003).

At the Krauthausen test site 76 observation wells with a diameter of 50 mm were installed reaching to a depth of 10-11 m below the surface (87 m above sea level). For local monitoring purposes, 66 observation wells were equipped with multilevel groundwater samplers (MLS) consisting of a bundle of 24 polyethylene tubes (diameter 0.5 cm) of different length attached to the outside wall of an observation well allowing a depth dependent sampling over 0.3 or 0.35 m intervals. The boreholes are screened over various depths. Most of the boreholes equipped with MLS are screened between 3 and 10 m below the surface.

To investigate the effect of aquifer heterogeneity on flow and transport processes, tracer experiments, in which the movement of an injected tracer solution in the aquifer is monitored, are carried out.

Two large scale tracer experiments were carried out consecutively at the test site in the autumn and winter months of the years 2002 and 2003. They were conducted as an ‘up-scaled’ continuation of a former, smaller scale tracer test where ERT imaging was used to monitor the breakthrough of a conductive tracer (Kemna et al., 2002).

A schematic picture of the test site is given in Figure 3-1.

3.1.1.3 Tracer Injection

One observation well, borehole 22, was chosen as injection well for the tracer solutions (cp. Figure 3-1). The injection well is screened between 3 and 11 m below the surface.

During both tracer tests 140 000 l of tracer solution were injected continuously over a time period of seven days. The tracer solution was injected over the entire screened well section which covers almost the entire saturated aquifer thickness. This was done by injecting the tracer solution by a tube on the top of the groundwater surface in the borehole. The flow rate was 835 l per hour. In the 2002 experiment we injected a calcium chloride solution with an electrical conductivity of approximately 6000 $\mu S \cdot cm^{-1}$ which was about a factor 6 more conductive than the mean natural groundwater conductivity of 950 $\mu S \cdot cm^{-1}$. In the second year a tracer solution with an averaged electrical conductivity of 241 $\mu S \cdot cm^{-1}$ and thus, factor four more resistive than the mean background groundwater conductivity which was 850 $\mu S \cdot cm^{-1}$ (in 2003) was injected.

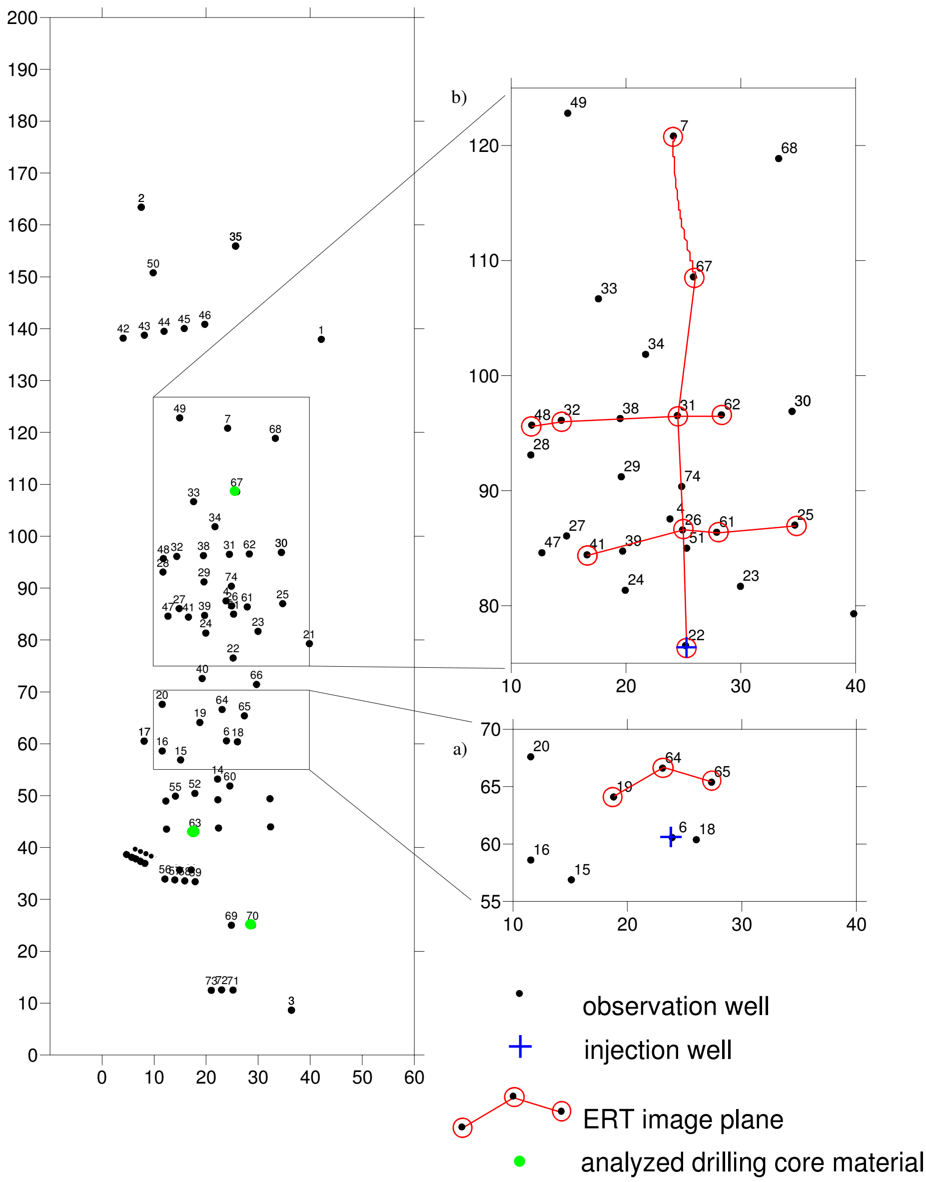

Figure 3-1: Map of the Krauthausen test site showing the distribution of monitoring wells (left) and location of the observation wells selected for ERT and MLS data acquisition during a) the small-scale tracer experiment described by Kemna et al. (2002) and b) the up-scaled tracer tests with the 'positive' tracer (2002) and the 'negative' tracer (2003).

In both tracer experiments, the injected tracer solution was prepared from drinking water (mean electrical conductivity of 500 $\mu S \cdot cm^{-1}$) which was mixed with a highly concentrated $CaCl_2$ solution (34 % $CaCl_2$) or de-ionized water. The de-ionized water was prepared at the field site using flow-through bottles filled with ion exchanger resins. The flow of the drinking water into the injection tube was regulated using a dynamic flow controller which was connected to the drinking water supply network and which automatically compensated for pressure variations on the net. The flow of the solutions that were pumped in the injection tube and mixed with the drinking water was monitored and manually regulated. Furthermore, to control the constancy of the conductivity, samples of the injected solution were taken and analyzed on site every thirty minutes. The tracer cloud of the so-called 'positive' tracer (more conductive tracer) was monitored over 78 days, the monitoring of the 'negative' tracer (more resistive tracer) was completed 71 days after the beginning of injection.

3.1.1.4 Monitoring of Tracer Plume Using MLS

The movement of the injected plume was monitored using local groundwater samples obtained from the MLS and using ERT measurements along three transects. The monitoring started with daily measurements in the first two weeks. After the first two weeks the monitoring was done every two or three days till the tailing was almost finished, and it ended up with weekly measurements. The multilevel groundwater sampling was carried out with a 12-channel peristaltic pump. To ensure that no stagnant water from inside of the tube was collected, 200 ml groundwater was flushed before taking the sample. The electrical conductivity of the samples at 25°C was determined in the laboratory because of the high amount of samples that were taken simultaneously to the ERT measurements at the test site. During the monitoring 12 of 24 MLS in each observation well in the investigation area were sampled. Between 264 and more than 300 groundwater samples were taken each sampling day. The location of the observation wells and the injection well are shown in Figure 3-1. To determine the natural background electrical conductivity of the groundwater and its spatial variability in vertical direction, observation wells located upstream from the injection well were sampled. In order to relate the electrical conductivity of the groundwater samples determined at the reference temperature of 25°C with ERT derived bulk electrical conductivity images at the temperature of the aquifer, the temperature of the groundwater was measured. The groundwater temperature was measured on site at a observation well upstream the tracer experiment by pumping out till the temperature remained constant in time. The temperature was 11°C at both experiments.

3.1.1.5 ERT Dataset Collection

For the ERT measurements two transects perpendicular to the mean flow direction were selected. The image planes were spanned by four sampling wells equipped with electrode chains in the screened borehole section. Each chain consisted of 16 0.5 m spaced electrodes, 13 of them situated in the saturated zone of the aquifer. The upper 3 electrodes were installed to capture the entire saturated aquifer thickness even if the groundwater table increases during the monitoring which started in September and ended in the more humid winter month December. The first cross section was positioned approximately 10 m downstream from the injection well and the second approximately 20 m. In addition, a cross section parallel to the mean flow direction, comprising 5 ERT boreholes, was monitored. In order to increase subsurface coverage, in particular in the near surface region down to a depth of 4 m below the surface the borehole electrodes were complemented with surface electrodes: 32 electrodes with 0.75 m and 40 electrodes with 1.1 m spacing for the image planes perpendicular and parallel to the mean flow direction, respectively.

For the ERT data collection, an electrical current I is injected into a pair of electrodes (dipole) and the electric potential difference between two other electrodes $\Delta\Phi$ is measured from which a transfer resistance **d** [Ω] is derived:

$$\mathbf{d} = \frac{\Delta\Phi}{I}. \qquad \text{Eq. 3-1}$$

In this study, electrodes were paired using a combination of standard 'skip-one' (surface electrodes) and 'skip-two' (borehole electrodes) dipole-dipole protocols. The 'skip-one' and 'skip-two' configurations led to similar dipole length in both arrangements. To avoid very high potential gradients only dipoles with at least one dipole length distance to the current injection were considered for potential measurements. Only dipoles of surface electrodes or of electrodes in the same borehole were used for current injection or potential difference measurements, leading to 1770 dipole current injections at a cross section (Gössling, 2004). The measurements were conducted over a period of almost 4 months (including the measurements to determine the background bulk electrical conductivity at the test site in the run up to the experiments) using a geoelectrical resistivity tomography instrument (RESECS, GEOSERVE GmbH Kiel, Germany). It was recently shown in a synthetic numerical experiment, with a similar ERT dataset collection configuration, that this setup is actually capable of resolving and quantifying solute transport characteristics in a 2D image plane (Vanderborght et al., 2005).

3.1.2 ERT Data Set Inversion

With ERT, a map of the spatial distribution of the bulk electrical conductivity EC_b is derived from datasets of transfer resistance measurements. For general distributions of the electrical conductivity, analytical expressions of the electric potential for a certain current injection are not obtainable and hence numerical finite element (FE) or finite difference (FD) models must be used. For our study the numerical solution comprised discretization of the investigation area (ERT image planes) into a finite element grid, a finite element forward modeling and minimization of an objective function.

3.1.2.1 Coordinate System for the ERT Data Set Inversion

For the ERT data set inversion approximations are necessary. One approximation is that the ERT surfaces are assumed to be straight lines and that the upper boundary is perfectly planar. At the field site, there are slight differences in the relief. The absolute height of the top ground above sea level was set to 98.4 m for the ERT data inversion. In reality the absolute height varies at the image planes. The deviations from the approximated height at the profiles are given in Table 3-1. These fluctuations affect the data sets derived from the surface electrodes which are tucked into the ground. Another approximation is that the cross sectional surfaces are assumed to be equal to the x-direction which is perpendicular to the mean flow direction.

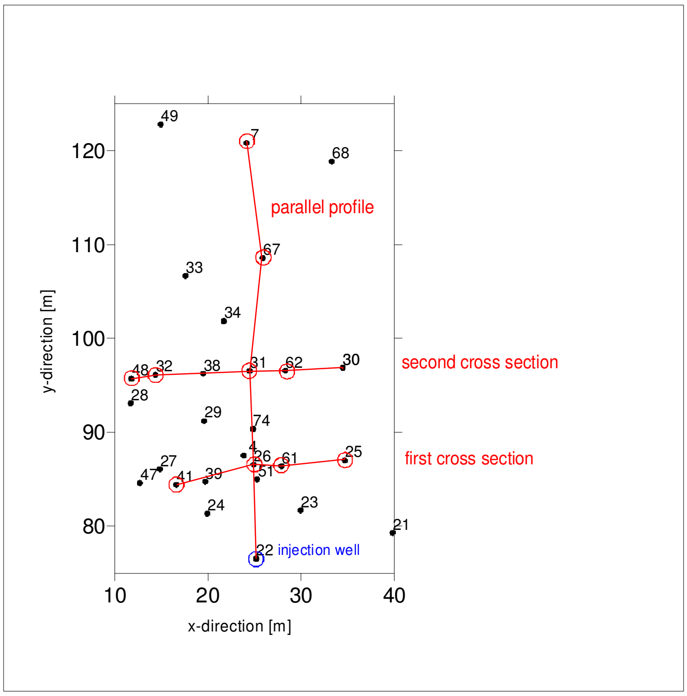

Figure 3-2: Positions of the ERT boreholes (red circles) and surface electrodes (straight red lines).

In reality only one borehole is situated exactly at the approximated straight image planes. For the first cross section, borehole 26 was suggested to be equal to the northing coordinate of the approximated straight ERT image plane. For the second cross section, the northing coordinate of borehole 31 corresponds exactly with the approximated straight image plane. The parallel profile is assumed to be parallel to the y-direction. For the ERT data inversion, the easting coordinate of the parallel profile was suggested to be equal to the easting coordinate of the injection well, borehole 22. The maximum deviations, of the other boreholes corresponding to the selected image planes, from the idealized ERT image planes are given in Table 3-1. Generally these approximations are maintainable and do not lead to significant errors.

Table 3-1: Easting and northing coordinates and height of the top ground above sea level at the field site and ERT coordinates in y-direction for the parallel profile and in x-direction for the two cross sections, respectively.

parallel profile	y [m]	y ERT [m]	x [m]	surface z [m NN]
borehole 22	76.52	2.50	25.18	98.29
borehole 26	86.58	12.56	24.91	98.31
borehole 31	96.52	22.50	24.47	98.37
borehole 67	108.58	34.56	25.87	98.42
borehole 7	120.82	46.80	24.13	98.40
maximum deviation from the approximated straight/planar profile [m]			1.05	0.11

first cross section	x [m]	x ERT [m]	y [m]	surface z [m NN]
borehole 41	16.60	3.90	84.41	98.39
borehole 26	24.91	12.49	86.58	98.42
borehole 61	27.89	15.47	86.38	98.44
borehole 25	34.70	22.31	87.00	98.46
maximum deviation from an approximated straight/planar profile [m]			2.17	0.06

second cross section	x [m]	x ERT [m]	y [m]	surface z [m NN]
borehole 48	11.78	4.89	95.69	98.33
borehole 32	14.36	7.47	96.11	98.31
borehole 31	24.47	17.58	96.52	98.37
borehole 62	28.30	21.41	96.58	98.38
maximum deviation from an approximated straight/planar profile [m]			0.83	0.09

3.1.2.2 Forward Modeling

In this study ERT is confined to vertical image planes. Assuming that the subsurface bulk electrical conductivity distribution EC_b is constant in the y direction which corresponds to the direction of the mean flow the 3D ERT imaging approach can be simplified to a 2D imaging approach after a Fourier transformation. The partial differential equation for the electrical potential and a current injection at the origin of the coordinate system, x = 0, may be expressed as:

$$\frac{\partial}{\partial x}\left(EC_b \frac{\partial \Phi}{\partial x}\right) + \frac{\partial}{\partial z}\left(EC_b \frac{\partial \Phi}{\partial z}\right) - \lambda^2 EC_b \Phi = -\mathrm{I}\delta(x)\delta(z) \qquad \text{Eq. 3-2}$$

where Φ is the potential in the Fourier transform domain, λ is the Fourier transform variable corresponding to the strike direction y, I is the source current, and δ is the Dirac delta function. To solve the forward problem typically mixed boundary conditions are used at the lateral and bottom boundaries (Dey and Morrison, 1979). The numerical solution is based on a finite element mesh (FEM). Within each element the electrical conductivity is assumed to be constant. The model space is discretized into discrete nodes and an appropriate solution is calculated at each node.

3.1.2.3 Numerical Inversion

Geophysical tomographic inverse problems are typically underdetermined because of the high amount of model parameters. One often used precondition for finding an appropriate electrical conductivity distribution is the smoothness constraint which requires the obtained distribution to be as smooth as possible. The inverse problem is formulated as an optimization problem and the smoothness constraint is incorporated within an objective function.

Referring to Daily et al. (1992) and LaBreque et al. (1996), the objective function can be expressed as:

$$\Psi(\mathbf{m}) = \|\mathbf{W}[\mathbf{r} - \mathbf{f}(\mathbf{m})]\|^2 + \alpha_r \|\mathbf{Rm}\|^2 \qquad \text{Eq. 3-3}$$

where $\mathbf{m}$ is the parameter vector representing the $\log_e$ transformed electrical conductivities in the different elements, $\mathbf{W}$ is a data weighting matrix used to weight individual resistances, $\mathbf{r}$ is the data vector of the measured and $\log_e$ transformed resistances, $\mathbf{f}$ is the operator of the forward solution, $\mathbf{R}$ is a matrix evaluating the roughness of $\mathbf{m}$ and α_r is a regularization parameter that determines the importance of the smooth appearance of the electrical conductivity field relative to the misfit between calculated and observed resistances. Based on a discrete pixel parameterization the differences between the measurements $\mathbf{r}$ and the forward modeling results **f(m)** are calculated. The data weighting matrix is

$$\mathbf{W} = diag(1/\varepsilon_1,...,1/\varepsilon_N) \qquad \text{Eq. 3-4}$$

assuming uncorrelated data errors ε_i. The data errors are given by a simple Gaussian error model in which the magnitude of the error ε_i increases with the magnitude of measured resistance R_i according to:

$$\varepsilon_i = \varepsilon_{\min} + \varepsilon_{Ri} \cdot R_i \,. \qquad \text{Eq. 3-5}$$

where $\varepsilon_{\min}$ stands for the minimum error whereas parameter ε_{Ri} defines the increase in ε_i with R_i (LaBrecque et al., 1996).

The roughness vector approximates the 2D gradient of the continuous distribution of

$\log_e EC_b$ associated with the discrete parameterization **m**, such that

$$\|\mathbf{Rm}\|^2 \approx \iint \|(\nabla EC_b)\|^2 dxdz \qquad \text{Eq. 3-6}$$

where the integration covers the (x, z) image plane (Kemna et al., 2002).

Due to the non-linear relation between the electrical potential and the specific transfer resistances the minimization of Eq. 3-3 is achieved with help of an iterative Gauss-Newton scheme. For each iteration step p, the linear system of equations

$$\left(\mathbf{A}_p^T \mathbf{W}^T \mathbf{W} \mathbf{A}_p + \alpha \mathbf{R}^T \mathbf{R}\right) \Delta \mathbf{m}_p = \mathbf{A}_p^T \mathbf{W}^T \mathbf{W}\left[\mathbf{r} - \mathbf{f}(\mathbf{m}_p)\right] - \alpha_r \mathbf{R}^T \mathbf{R} \mathbf{m}_p \qquad \text{Eq. 3-7}$$

is solved for a model update $\Delta\mathbf{m}_p$. $\mathbf{A}_p$ is the Jacobian matrix evaluated for the current model $\mathbf{m}_p$ with $\mathbf{A}_{ij} = \partial r_i / \partial m_i$. As starting model of the inversion a homogeneous EC_b distribution determined from the mean measured response was used. The iteration process stops if an acceptable target value of the objective function is reached. Statistically the target value can be defined by a root mean square (RMS) value of one as described in the following equation:

$$1 = \sqrt{\frac{\Psi_d(\mathbf{m})}{N}} \qquad \text{Eq. 3-8}$$

where N is the number of independent data and $\Psi_d(\mathbf{m})$ is the data misfit. From statistical theory $\Psi_d(\mathbf{m})$ should be of the order of the number of data N.

3.1.2.4 Difference Inversion

When monitoring transport processes, the main interest is in the mapping with high spatial resolution (at image planes) of temporal changes in electrical conductivity. Hence, to monitor tracer migration, images of electrical conductivity at several time steps during and after tracer injection are compared to the pre-tracer condition in the observed image plane. There are several approaches to image temporal changes, all of which have the aim to eliminate time-static features in conductivity structures such as textural properties of the aquifer and as a consequence thereof to emphasize time-varying features of the electrical conductivity images.

One approach is to model and invert the ratios of transfer resistance measurements at several time steps (t > 1) and a background transfer resistance dataset (t = 0) multiplied by the corresponding, calculated resistance distribution for the homogenous reference model (Daily and Owen, 1991). This approach yields an absolute image of the temporal resistivity changes. More recently, LaBreque and Yang (2001) proposed to use a background model

$\mathbf{m}_0$ instead of a homogeneous reference model. This approach is referred to as 'difference inversion'. The objective function to be minimized is:

$$\Psi_{diff}(\mathbf{m}) = \left\| \mathbf{W}[\mathbf{r} - \mathbf{r_0} + \mathbf{f}(\mathbf{m_0}) - \mathbf{f}(\mathbf{m})] \right\|^2 + \alpha_r \left\| \mathbf{R}(\mathbf{m} - \mathbf{m_0}) \right\|^2 \qquad \text{Eq. 3-9}$$

For the measurements at the test site, the background model $\mathbf{m_0}$ was used as starting model for the difference inversion. The model was derived from an absolute inversion of the background data $\mathbf{r_0}$. The background model was determined applying an absolute inversion with a relative error of 5 % and an absolute error of 0,3 Ωm (Gössling, 2004). The advantage of this approach is that smoothness is directly imposed on the model change **m - m₀** and thus independent from time-static structures in **m** or $\mathbf{m_0}$. Furthermore systematically errors, which occur similarly in **r** and $\mathbf{r_0}$, cancel out each other. The same is true for the systematic errors in **f(m)** and $\mathbf{f(m_0)}$ (Gössling, 2004).

3.1.2.5 ERT sensitivity

An important attribute for the interpretation of ERT inverted images is the spatial resolution which is a complex function of numerous factors (e.g. electrode layout, measurement schedule, data quality, imaging algorithm, electrical conductivity distribution) and, in general, varies significantly across the image plane (Kemna et al., 2002).

One simple and indirect approach that deals with the complex problem of resolution is the analysis of ERT sensitivity. Sensitivity describes how a local change in electrical conductivity affects a single transfer resistance measurement. The sum of all sensitivities related to local scale changes in electrical conductivity at a certain location is an indirect measure of how well the conductivity at this location may be retrieved from the measurement data set. This sensitivity sum is calculated for each discretized element from the Jacobi and data weighting matrices $\mathbf{A}$ and **W** as:

$$\sum_{i=1}^{N} \left[\frac{(\mathbf{A})_{ij}}{\varepsilon_i} \right] = \left(\mathbf{A}^T \mathbf{W}^T \mathbf{W} \mathbf{A} \right)_{jj} \ . \qquad \text{Eq. 3-10}$$

The map of these sensitivity sums shows to which extent different locations influence the ERT dataset obtained for a certain electrode arrangement and data collection. High sensitivities signalize a high resolution, low sensitivities signalize that the transfer resistance measurements may be afflicted with noise. In principle, as to be expected and well-known (Ramirez et al., 1993), overall sensitivity decreases dramatically towards the bottom of the ERT plane and towards the middle between two electrode chains, indicating significant loss of resolution in these regions (Kemna et al., 2002).

3.1.3 Relation between Bulk EC and Tracer EC

With ERT the bulk electrical conductivity EC_b of the aqueous phase and the solid matrix is determined whereas from the multilevel groundwater sampling the electrical conductivity of the groundwater EC_w is derived.

According to Archie's law (Archie, 1942) the bulk electrical conductivity is directly related to the solute electrical conductivity. In the absence of significant matrix conduction and assuming total saturation the relation between bulk electrical conductivity and solute electrical conductivity is:

$$EC_w = F \cdot EC_b \qquad \text{Eq. 3-11}$$

where F is the formation factor which is a function of physical properties of the aquifer.

Though the fact that EC_b is a generally non-linear function of EC_w, in many cases, it may be fairly well approximated by a linear calibration function:

$$EC_b = a(\mathbf{x})EC_w + b(\mathbf{x}) \qquad \text{Eq. 3-12}$$

where $a(\mathbf{x})$ and $b(\mathbf{x})$ are empirical calibration parameters independent of salinity (Sen et al., 1988, Rhoades et al., 1989). In heterogeneous aquifers the calibration parameters obviously depend on location **x** (Kemna et al., 2002). This fact has also been observed at the test site where the initial bulk electrical conductivity $EC_{b(ini)}$ varied considerable with location compared to the relative constant background conductivity of the groundwater $EC_{w(ini)}$. The assumption in Eq. 3-12 was verified by laboratory measurements on aquifer sediment from the Krauthausen test site. Columns packed with aquifer sediment were charged with tracer solution of known electrical conductivity. As tracer a calcium chloride solution was used with electrical conductivities ranging from 100 $\mu S \cdot cm^{-1}$ up to 5000 $\mu S \cdot cm^{-1}$. The measurements were conducted with sediment from different depth, and with different fractions of gravel and sand. Samples were taken from three vertical drilling cores at intervals from 4.5 up to 9.5 m below surface from drilling cores of borehole 63 and 67, and 5.5 to 6 m and 7 to 7.5 m from drilling core B 70. The location of the boreholes is shown in Figure 3-1. From the sediment taken at boreholes 63 and 67 only the sediment fractions with a grain size smaller than 20 mm and 2 mm, respectively, were used. The gravel and sand fractions of borehole 70 were first separated by sieving. Subsequently, soil columns were packed using three different gravel-sand mixtures: 70 % sand and 30 % gravel, vice versa with 30 % sand and 70 % gravel and 50 % sand and 50 % gravel (percentages correspond with gravimetric sediment fractions). The porosity of the samples varied between 20.4 and 30.7 % and the density of the packed sediment material was 2.62 g · cm^{-3}. The bulk electrical conductivity EC_b was measured with Time Domain Reflectrometry (TDR), and standardized to 25°C.

In order to compare the ERT bulk electrical conductivities with the solute electrical conductivities derived from multilevel sampling both measurements were standardized at a reference temperature of 25°C. As mentioned before the solute samples were analyzed in the laboratory. For the ERT derived pixel electrical conductivities a temperature correction factor was used (Franson, 1985):

$$f_T = \frac{1}{\left[1 + \alpha_T (T - 25)\right]} \qquad \text{Eq. 3-13}$$

where α_T [°C^{-1}] is the temperature coefficient of the sample, which is equal to 0.0191°C for the standard 0.01 mol·l^{-1} KCl solution, and T [°C] is the temperature of the groundwater. In our case the temperature of the groundwater was constant at 11°C during the experiments.

3.1.4 Lab-Scale Breakthrough Experiments to Test the Conservation of the Positive and Negative Tracer Solutions

To test whether the 'positive' and 'negative' solutions represent conservative tracers for groundwater transport, lab-scale breakthrough experiments were carried out in columns packed with aquifer sediment. The sediment was taken from drilling core B69 at an interval from 9.5 to 10 m below the surface. Only sediment fractions with a grain size smaller 2 mm were used. The columns were first saturated with groundwater, then charged with a 1 mol·l^{-1} $CaCl_2$ pulse ('positive' tracer), and subsequently with a 'negative' tracer pulse, which was a mixture of groundwater and de-ionized water with a ratio of 1:9. The flow rate through the columns was kept constant and amounted 0.29 m·min^{-1}. The experiments were conducted over a period of 50 and 60 hours, respectively. The electrical conductivity of the effluent was measured using a flow through cell and corrected to a reference temperature of 25°C.

In Figure 3-3 breakthrough curves of the positive and negative tracer pulses are shown. A visual inspection of the breakthrough curves confirms that the transport behavior of both tracer solutions is similar. Both tracer solutions behave as conservative tracers (Müller et al., 2005).

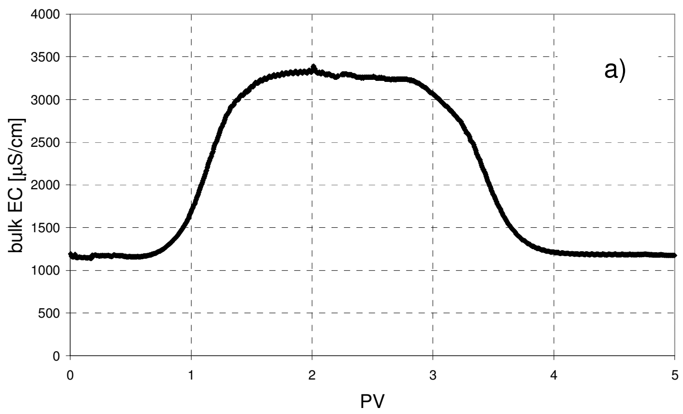

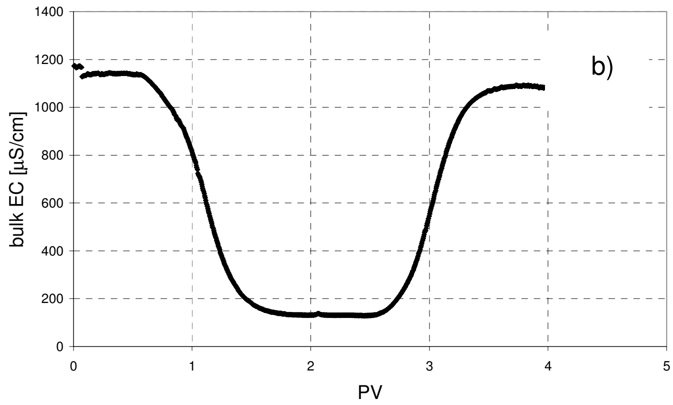

Figure 3-3: Breakthrough curves derived from laboratory experiments. Water-saturated column a) charged with the 'positive' tracer and b) with the 'negative' tracer.

3.1.5 Mass Balance

For the approximation of the amount of tracer mass that was recovered with ERT at the two cross sections mass balances were estimated. The general equation to calculate the tracer mass at a reference plane which is perpendicular to the mean flow direction may be defined as:

$$M = \int q_1(\mathbf{x})(C_t(\mathbf{x}) - C_{ini})dtdxdz \qquad \text{Eq. 3-14}$$

where C_t is the measured concentration at time t and C_{ini} is the background concentration. A problem with the application of Eq. 3-14 is that $q_1(\mathbf{x})$, the local water flux at location **x**, is generally not known. Therefore, the local flux was approximated by the mean flux $\langle q_1 \rangle$ through the reference plane, which we further assumed to be constant in the reference plane.

$$M = \iiint \langle q_1 \rangle (C_t(\mathbf{x}) - C_{ini}) dtdxdz \qquad \text{Eq. 3-15}$$

Due to the fact that not concentrations but electrical conductivities were measured and with the knowledge that concentration and conductivity behave proportional, a "factor" was introduced to estimate the recovered tracer mass from electrical conductivity measurements.

$$EC_w \sim C \Rightarrow f \cdot EC_w = C \qquad \text{Eq. 3-16}$$

where $f = \left[\frac{kg}{m^3}\right] \cdot \left[\frac{cm}{\mu S}\right]$. It has to be mentioned that the factor f is ion-specific. With the help of calibration relations between concentration and conductivity for specific ions it is possible to determine the recovered tracer mass from electrical conductivity measurements. For the 'positive' and 'negative' tracer experiments the recovered mass was determined without the ion-specific factor. With the knowledge of the exact amount of injected tracer substance and the relative amount of tracer 'mass', that was recovered at the first cross section in the 'positive' tracer test, it was possible to determine the absolute amount of recovered tracer mass. For the 'negative' tracer test only the relative amount of recovered tracer was determined because of the fact that not a salt solution with a given concentration but a water with lower electrical conductivity was injected.

The 'mass' of tracer derived from bulk electrical conductivity measurements at a cross sectional area is consequently:

$$M = f \cdot \iiint \langle q_1 \rangle (EC_{w(t)} - EC_{w(ini)}) dtdxdz\,. \qquad \text{Eq. 3-17}$$

The initially injected tracer 'mass' based on the bulk electrical conductivity is given by:

$$M_{ini} = f \cdot (EC_{w(0)} - EC_{w(ini)}) \cdot V_0 \qquad \text{Eq. 3-18}$$

where $EC_{w(0)}$ is the electrical conductivity of the injected tracer solution and $EC_{w(ini)}$ is the initial background electrical conductivity of the groundwater and V_0 is the injected tracer volume.

Since bulk electrical conductivities were measured with ERT, the EC_w needed to be related to EC_b (cp. Eq. 3-12) and thus the resulting equation to calculate the recovered 'mass' at a cross sectional area may be defined as:

$$M = f \cdot \left[EC_{w(ini)} + \frac{b}{a} \right] \iiint \langle q_1 \rangle \left[\frac{EC_{b(t)} - EC_{b(ini)}}{EC_{b(ini)}} \right] dt dx dz \qquad \text{Eq. 3-19}$$

where a and b are the empirical correlation parameters, the formation factor and the intercept, derived from column experiments with aquifer sediment (cp. subsection 3.1.3).

To simplify the mass balance equations, we approximated the ERT reference planes by planar surfaces and assumed that the x-coordinate corresponds with the trajectory along the reference plane.

3.1.6 Derivation of the Equivalent Parameters from ERT and MLS

The equivalent transport parameters were determined at two reference planes 10 and 20 m distant to the injection well for the 'negative' tracer test 2003 and at one reference plane 10 m from the injection well for the 'positive' tracer test. Equivalent transport parameters were derived from the inverted ERT data and compared to equivalent transport parameters derived from the MLS in the boreholes situated at the ERT reference planes. Both, ERT and MLS data were related to a bulk background conductivity/resistivity model (ERT) and a mean background solute conductivity (MLS). Therefore, the calibration relations between bulk aquifer conductivity and resistivity, respectively, to solute conductivity or solute concentrations were not required for the quantification of the transport processes. The derivation of the equivalent parameters was done using the SAS/STAT® statistical software package.

The ERT data sets of each monitoring day inverted with the difference inversion approach were merged and sorted by day, x- and z-coordinates and bulk electrical conductivity ('positive' tracer test) and resistivity ('negative' tracer test), respectively. The zeroth moment was determined for each pixel by integrating the bulk conductivity (resistivity) breakthrough at each pixel. Data with no tracer breakthrough were set to zero. After this procedure v_{eq} and λ_{eq} were obtained from fitting the final ERT data set to the one-dimensional convection dispersion equation (cp Eq. 2-28).

The transport observed with multilevel sampling was quantified with the same method as the ERT data. The transport parameters were derived from the monitored solute conductivities at the MLS of each borehole situated at a reference plane. The analyzed data were the absolute differences in solute electrical conductivity compared to the natural background conductivity of the groundwater. The data sets generated for each monitoring day were merged and sorted by day, borehole, multilevel samplers and solute electrical conductivity. After integrating the solute conductivity breakthrough for each multilevel sampler at each borehole v_{eq} and λ_{eq} were determined by a least square fit of the one-dimensional convection dispersion equation.

The parameters were fitted because negative solute or bulk electrical conductivities (resistivities), respectively, were occasionally observed in the inverted ERT bulk electrical conductivity images due to inversion artifacts as well as in the local solute breakthrough curves derived from MLS due to variations in the natural background conductivity of the groundwater. Since time moments were strongly influenced by conductivities smaller than the background in the tail of the breakthrough, especially the higher moments, negative conductivities in the tailing part of the breakthrough occasionally led to artificially small mean arrival times and negative travel time variance (Vanderborght et al., 2005).

Figure 3-4 shows exemplarily two selected measured and fitted BTCs derived from multilevel sampler 18 at the boreholes 26 (first cross section, 10 m distant to the injection well) and 31 (second cross section, 20 m distant to the injection well) during the 'positive' tracer test. The fitted curves were generated by a least square fit of the 1D CDE. The plots show that the measured BTC are well described by the 1D CDE fit.

On closer examination to borehole 26 which is situated in direct flow direction from the injection well borehole 22 (cp. Figure 3-1) it has to be noted that the monitoring of the tracer breakthrough was not ideal for this observation well. There was a lack of monitoring between monitoring day 9 and 13 after the beginning of injection due to logistic reasons. This led to an insufficient mapping of the tracer breakthrough. In consideration of the injection which was done continuously over seven days the breakthrough curve should have shown a plateau.

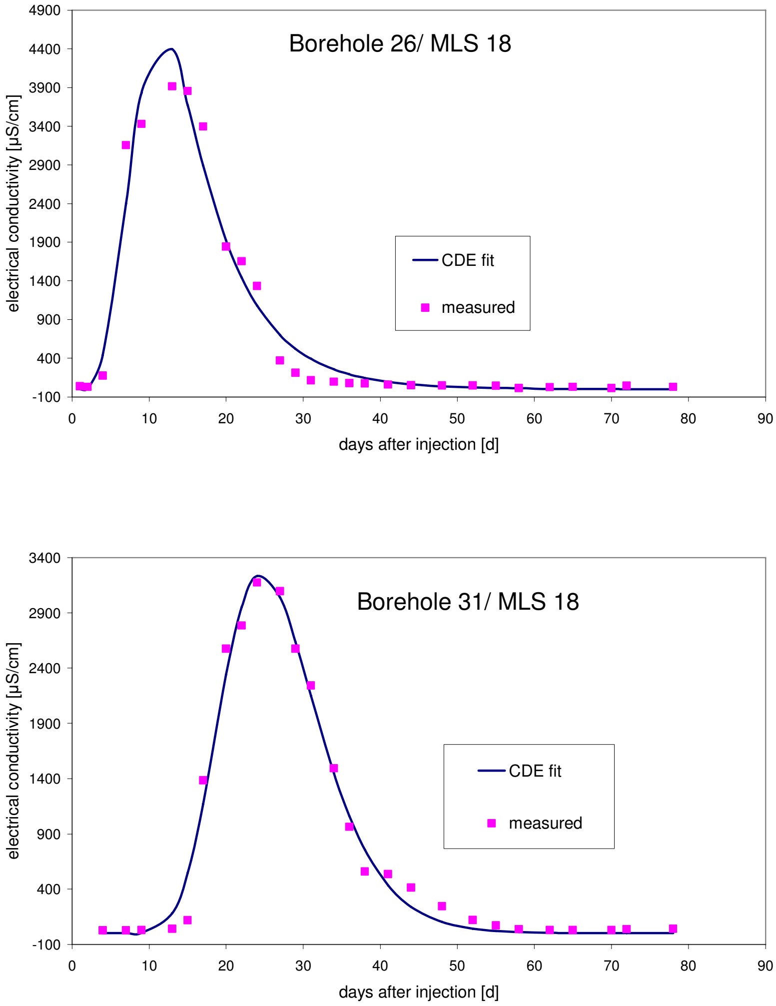

Figure 3-4: Selected measured and fitted BTCs derived from the MLS data during the 'positive' tracer test. Borehole 26 is situated 10 m distant to the injection well (first cross section), borehole 31 is situated 20 m distant to the injection well (second cross section).

3.2 Results

This chapter is composed of two parts. In the first part, the ERT images are discussed. This part includes the sensitivity of the ERT electrode configurations, the background EC_b distribution, a comparison between ERT images and data obtained from MLS, and a comparison between the positive and negative tracer images.

In the second part, the observed tracer data are quantitatively interpreted. First, mass balances are derived. Second, equivalent transport models are used to quantify the observed breakthroughs. With the aid of equivalent transport models, the spatio-temporal information about the transport process in the breakthrough datasets is 'condensed' or 'summarized' in spatial images of equivalent transport parameters. This summary further facilitates a comparison between the different tracer tests and different observation methods.

3.2.1 Electrode Configuration and Sensitivity

Figure 3-5 shows on the left side the relative changes in bulk electrical resistivity at the first cross section (tracer test 2003) 14 days after tracer injection derived from measurements with both, surface and borehole electrodes and from measurements using, only borehole electrodes and only surface electrodes, respectively. On the right side the corresponding sensitivities for the electrode configurations are imaged.

The relative changes in resistivity show no significant difference with regard to the application of only borehole or both, borehole and surface electrodes. There is only a difference in the magnitude of the tracer signal. Because of the higher amount of implemented data, the relative change imaged with the combined surface-borehole-electrode configuration is likely better than the borehole configuration (Gössling, 2004). The tracer breakthrough could not be resolved with only the surface electrode measurement schedule. In 2002 ('positive' tracer test) the surface electrodes did not give additional spatial resolution because of the poor electrode-soil contact due to the very dry soil conditions when the measurements were conducted. For the 'negative' tracer test, both surface and borehole electrodes were used in the ERT inversions because of the higher data amount as mentioned above.

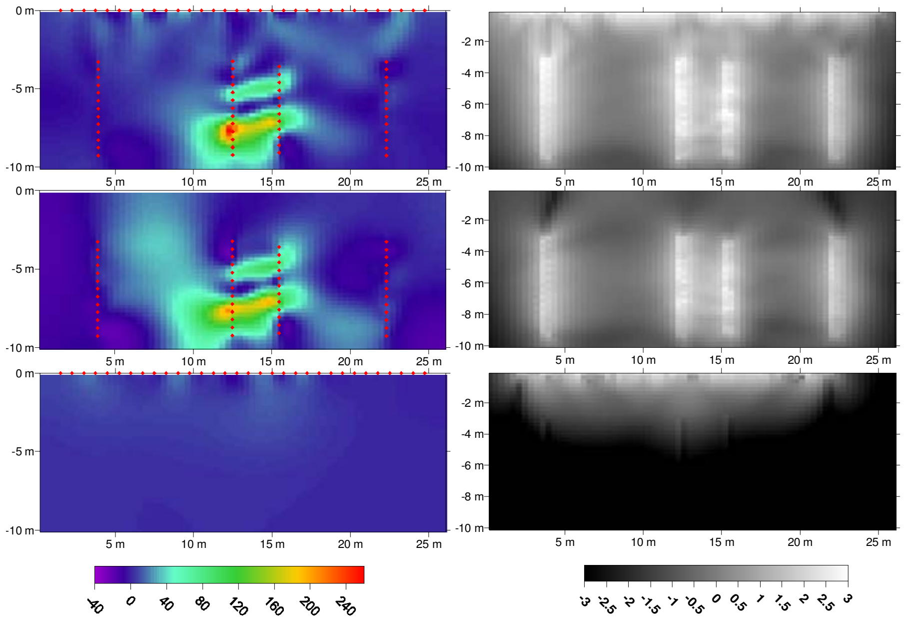

Figure 3-5: Relative changes in bulk electrical resistivity [%] (left side) and sensitivity (right side) derived with surface and borehole electrodes (upper diagrams), only borehole electrodes (middle diagrams), and only surface electrodes (lower diagrams) at the first cross sectional ERT image plane at monitoring day 14 after beginning of injection. Sensitivities are given in [$\log_{10}$ Ωm].

3.2.2 The Background Model

Based on the difference inversion approach temporal relative changes in bulk aquifer electrical resistivity or conductivity, respectively, measured with ERT at different time steps can be imaged with reference to a certain background model. The resulting ERT background images of the electrical resistivity distribution and the corresponding sensitivities are shown for the first and second cross section and for the parallel profile in Figure 3-6. Basically, the background distribution reflects the lithological situation at the test site with a highly resistive layer at a depth about 2 m below the surface corresponding to the unsaturated gravel sediment below the top loess soil layer. Below 2 m the saturated zone of the aquifer is marked by a decrease in resistivity. Between 4 and 5 m below the surface is a layer with slightly lower resistivities which corresponds to a layer with a higher sand fraction than in the over- and underlying sediment layers. Furthermore, the ERT images of the second cross section and the parallel profile show regional anomalies in electrical resistivity in the lower central part of the image planes. These anomalies are due to the large distances between the ERT boreholes and the consequentially low sensitivity in this part of the sections.

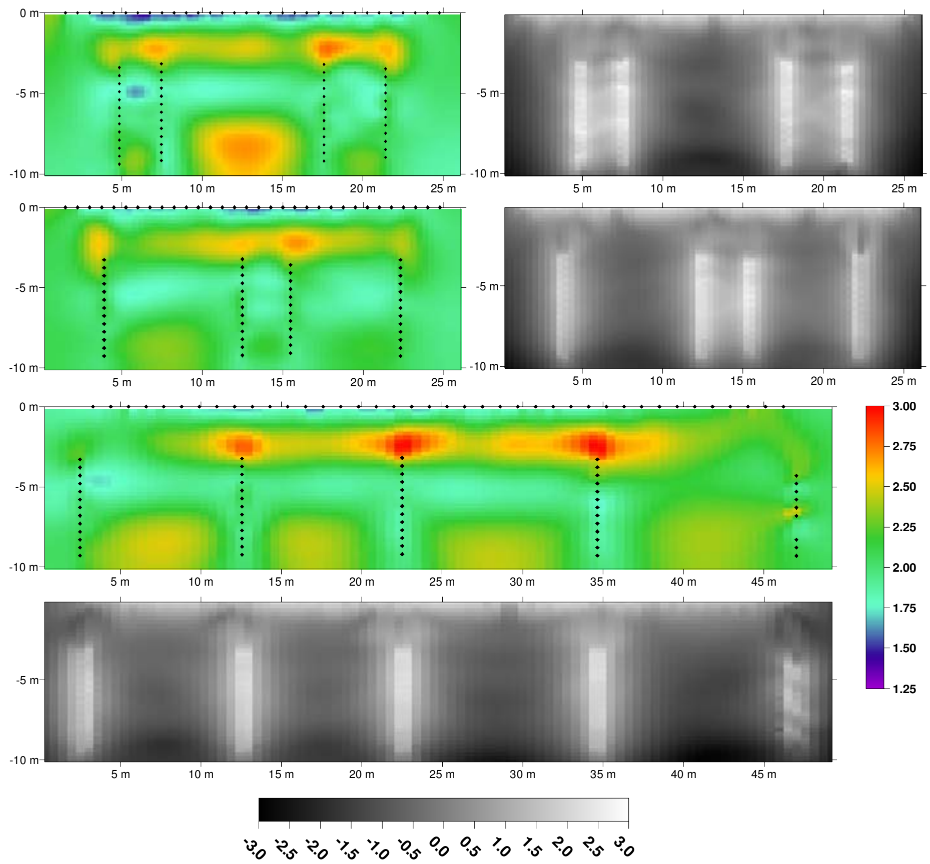

Figure 3-6: ERT background images of the bulk electrical resistivity distribution in [$\log_{10}$ Ωm] (colored images) and the corresponding sensitivities (grey shaded images) at the second cross section (above), the first cross section (middle), and the parallel profile (below). Resistivities and sensitivities are given in [$\log_{10}$ Ωm].

3.2.3 Derivation of Bulk Electrical Conductivity

As introduced in section 3.1.3 laboratory measurements on columns packed with aquifer sediment were conducted to derive empirical calibration parameters. A linear calibration relation was determined that relates the solute electrical conductivity (EC_w) derived from groundwater multilevel sampling to the bulk aquifer conductivity (EC_b) measured with ERT. The calibration results of three column experiments with different gravel to sand fractions of aquifer sediment are illustrated in Figure 3-7. The aquifer sediment was taken from the drilling core of borehole 70 at a depth between 7 and 7.5 m below the surface. The formation factor $a(\mathbf{x})$ varied between 0.15 and 0.18 and increased with decreased gravel content. The intercept $b(\mathbf{x})$ varied between 12 and 23 µS · cm^{-1} but there was no clear relation with sand or gravel contents.

To correlate the EC_b data derived from the ERT measurements with the MLS derived EC_w in the following, a temperature correction factor of 1.365 was determined to standardize the ERT samples to a temperature of 25℃.

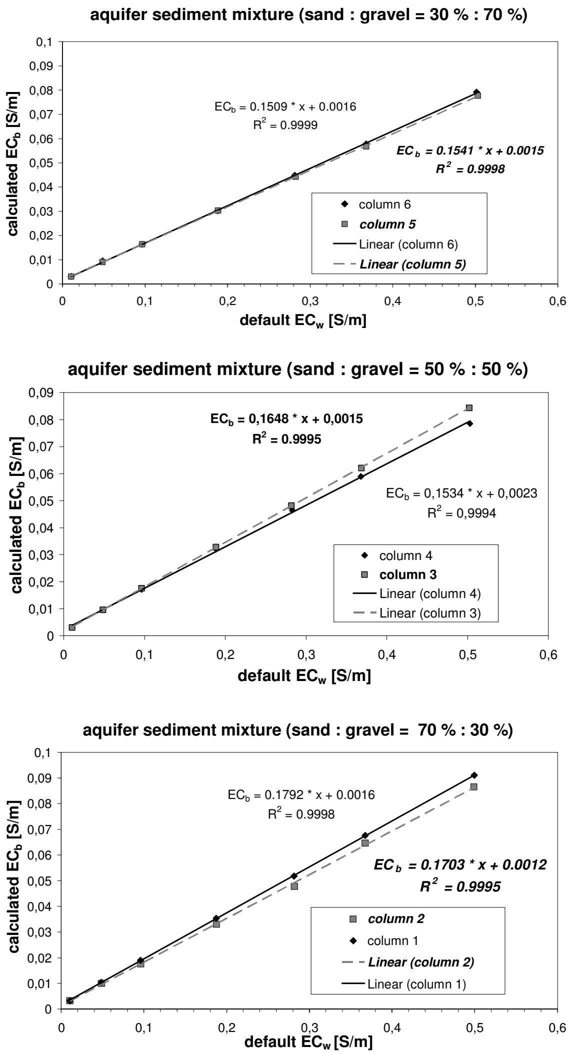

Figure 3-7: Linear correlation between default EC_w concentrations of the tracer solution and TDR measurements of bulk EC_b on columns with different sand fractions.

The intercept $b(\mathbf{x})$ was negligible for the translation between EC_w and EC_b for the range of conductivities in the positive tracer test conducted in 2003 (0.1 S m^{-1} < EC_w which corresponds with 0.02 S m^{-1} < EC_b). For the range of conductivities the negative tracer test conducted in 2004 (0.025 S m^{-1} < EC_w < 0.1 S m^{-1} corresponding roughly with 0.005 S m^{-1} < EC_b < 0.02 S m^{-1}), the intercept $b(\mathbf{x})$ could not be neglected.

3.2.4 Comparison of Bulk Electrical Conductivities

3.2.4.1 Comparison of Relative ERT and MLS Tracer Breakthrough

In Figure 3-8 the temporal changes in relative bulk electrical resistivity ('negative' tracer 2003) and bulk electrical conductivity ('positive' tracer 2002) for several time steps after the start of injection are shown. The first cross section corresponds to the transect perpendicular to the mean flow direction located in about 10 m distance to the injection well. The temporal ERT images were obtained by applying isotropic smoothing for regularization in the inversions. Concerning to the regularization it is important to keep in mind that the type of smoothing (i.e. horizontal, isotropic, or vertical) influences the type of the recovered plume as well as it affects the fitted transport parameter. The relative changes in bulk soil resistivity are defined as

$$\Delta_r \rho[\%] = 100 \cdot \left[\frac{\rho - \rho_{(ini)}}{\rho_{(ini)}} \right] \qquad \text{Eq. 3-20}$$

where $\rho_{(ini)}$ is the initial background bulk soil resistivity and ρ is the measured bulk soil resistivity which can be approximated by a linear calibration function of EC_b. Based on the relation that $\rho = 1/EC_b$, the bulk soil conductivity can be derived from the bulk soil resistivity and written as:

$$\Delta_r EC_b[\%] = 100 \cdot \left[\frac{1/\rho - 1/\rho_{(ini)}}{1/\rho_{(ini)}} \right]. \qquad \text{Eq. 3-21}$$

The local data derived from the groundwater samples are shown in the ERT images and represented by vertical bars in the location of the boreholes. The relative changes in local solute conductivities were converted to relative changes in bulk aquifer conductivities and accordingly bulk aquifer resistivities adapted from equations Eq. 3-20 and 3-21 and may be approximated by:

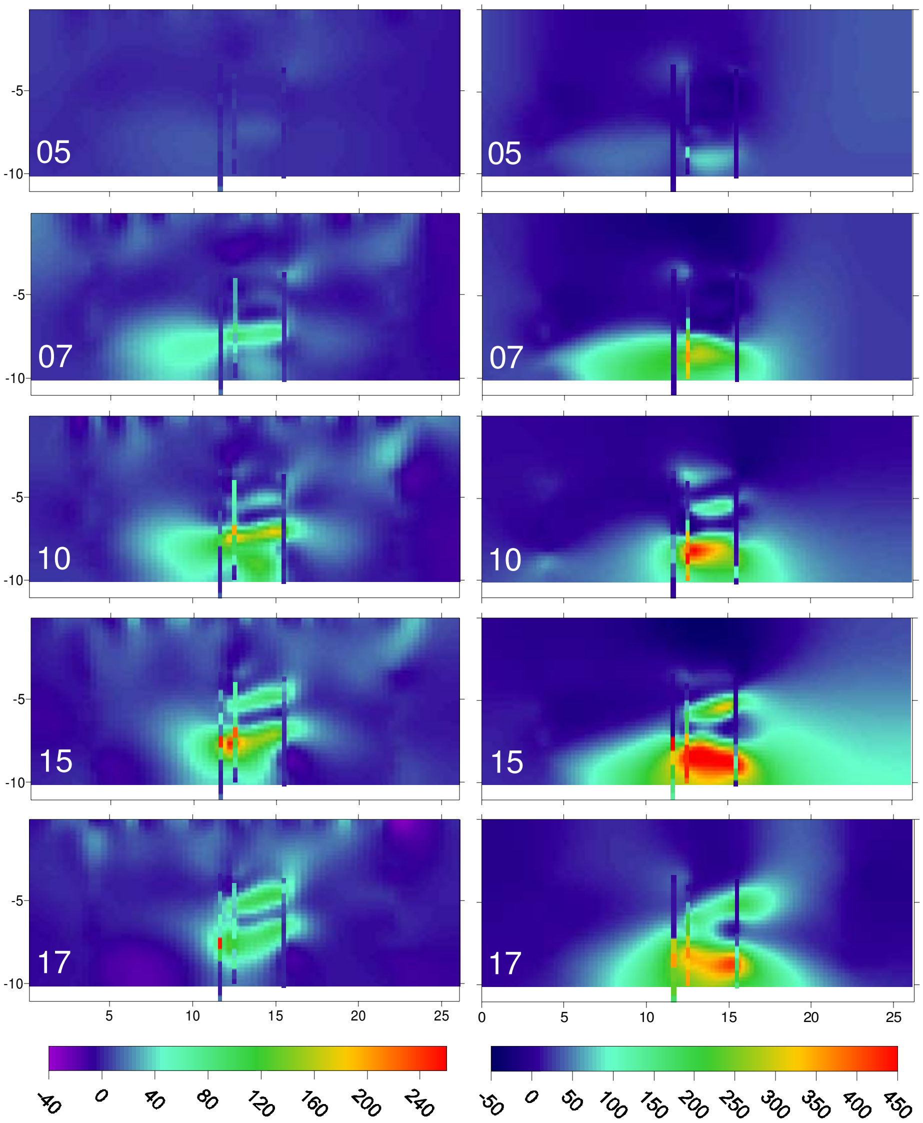

Figure 3-8: Relative changes in bulk aquifer resistivity for the 'negative' tracer test (left side: relative change of ρ in [%]) and in bulk aquifer conductivity for the 'positive' tracer test (right side: relative change of EC_b in [%]) in days after the beginning of injection monitored at the first cross section. *(continuation on the next side)*

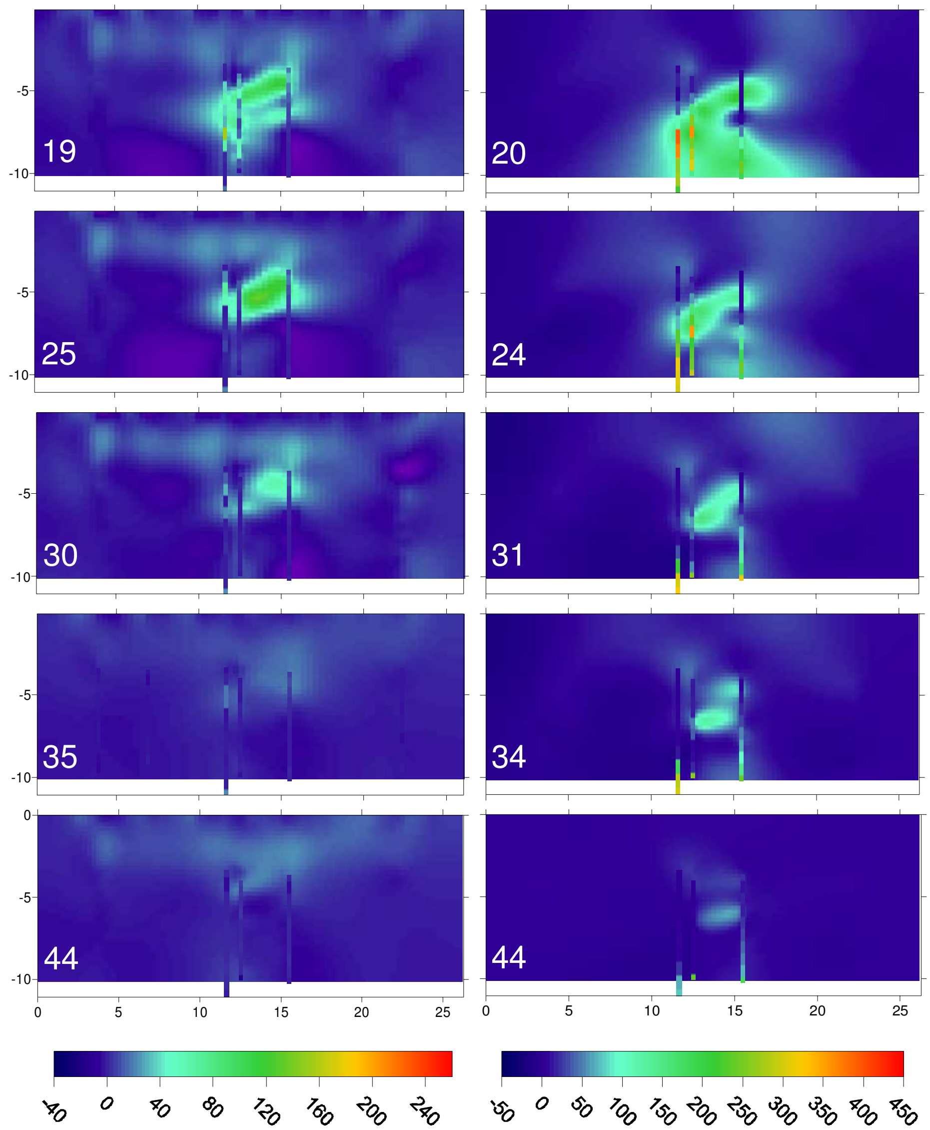

(continuation of Figure 3-8*)*

$$\Delta_r \rho[\%] = 100 \cdot \left[\frac{1/EC_w - 1/EC_{w(ini)}}{1/EC_{w(ini)}} \right] \text{ and} \qquad \text{Eq. 3-22}$$

$$\Delta_r EC_b[\%] = 100 \cdot \left[\frac{EC_w - EC_{w(ini)}}{EC_{w(ini)}} \right]. \qquad \text{Eq. 3-23}$$

In equations Eq. 3-22 and 3-23 the conductivity of the matrix or the intercept $b(\mathbf{x})$ (cp. Eq. 3-12) in the EC_b - EC_w relation has no impact on the equation.

The implementation of MLS data in the relative ERT images shows a rather good coincidence with the ERT derived changes, with respect to the arrival times of the tracer plumes and the relative peak magnitude. But differences obviously exist. Seven days after the beginning of the injection the ERT images already show a lateral spreading of the plume whereas with local multilevel sampling there were only changes in one borehole detected which is situated straight upstream from the injection well but not in the adjacent boreholes. During the positive tracer test, a tail of residual high conductivities was observed in selected MLS which are situated in the lower part of the aquifer near to the aquifer base. These observations are believed to be artifacts because even one year later in the run-up to the 'negative' tracer test higher conductivities than the background conductivity were measured in the same local MLS. This suggests that these MLS are not sufficiently connected to the aquifer and the groundwater flow in this region and that water seemed to be stagnant around the lower section of the borehole.

Concerning the second perpendicular profile, which was situated about 20 m distant from the injection well, only the data for the 'negative' tracer test are inverted. The selected ERT images showing relative changes in bulk electrical resistivities and completed with the local MLS data are presented in Figure 3-9. First, the ERT images of the second cross section appear to be more diffuse than the corresponding images derived for the first cross section. The signal-to-background contrast is less distinct as a result of successive dilution with increasing distance from the injection source. The main process controlling dilution is the local dispersion which is an effect of the interaction of molecular diffusion and complex pore scale velocity (Delleur, 1999).

In the upper zone of the ERT image plane higher and temporally varying resisitivities were observed. These observations might be due to temporal moisture content changes associated with rainfall events and dry periods during the monitoring period. The upper part corresponds with the unsaturated zone. The groundwater table sank about 10 cm from beginning to the end of the monitoring.

The tracer cloud monitored with ERT at the second cross section spread out to a lesser horizontal extend as one could have expected in view of the results from groundwater multilevel sampling. This may be explained by insufficient ERT resolution. With MLS a slight breakthrough was detected in a central borehole at day 17 and day 28 which was not observed in the ERT images. This borehole was not equipped with ERT electrodes since it was not fully screened. The peak of the tracer breakthrough at the second cross section was observed after 21 days with a contrast of about 100 %. This observation fits well to the data derived from groundwater multilevel sampling. Compared to the local data, the ERT images showed a pronounced tailing.

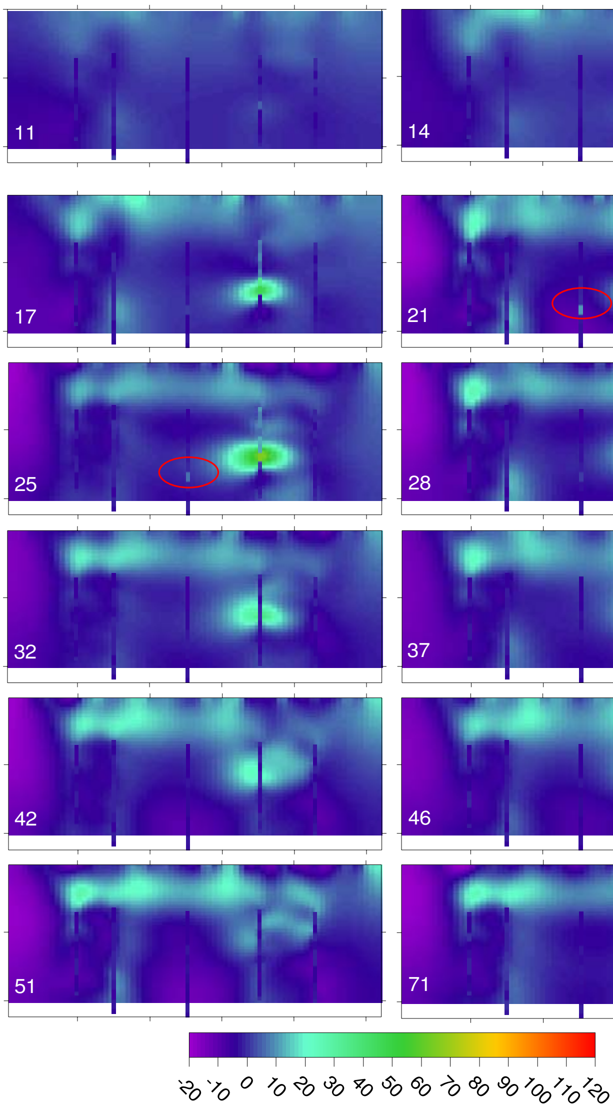

Figure 3-9: Relative change in bulk electrical resistivity [%] monitored with ERT and MLS (columns) at the second cross sectional reference plane (numbers = days after the beginning of injection). Red marked is the tracer breakthrough in borehole 38 (cp. Figure 3-1).

In the ERT inversion, the roughness model, which is related to the model contrast, is minimized subject to fitting the data to an acceptable degree (noise level). For a decreasing model contrast the signal-to-noise ratio decreases. As a consequence, the smoothness constraint leads to a more pronounced decrease in spatial resolution and contrast in the inverted image when the model contrast decreases (Vanderborght et al., 2005).

The tracer plume evolution in the parallel to flow direction profile is illustrated in Figure 3-10 for the 'negative' tracer injection. The borehole at the left hand side of the image plane represents the injection well. As mentioned above, the tracer was injected continuously for one week and over the entire aquifer thickness, which explains the very high relative changes in resistivity in this borehole during the first days of monitoring with a maximum of 280 % observed in the MLS. In contrast, ERT monitored changes were less distinct with only 130 % increase during the injection period. After the injection and during the ongoing monitoring, MLS and ERT showed the opposite behavior with higher relative changes in the ERT image and fast decreasing resistivity in the MLS. During the injection the tracer volume released in the injection well was too small to be resolved with ERT. The insufficient resolution is the result of the discretization of the model elements on the one hand and the smoothness constraint on the other hand. The opposite phenomena after more than one week can be explained by the specific flow conditions in a borehole. Due to differing hydraulic conductivities inside a well, in the well screen, in the filter pack and in the aquifer, the flow in a borehole is characterized by the convergence of the streamlines towards the borehole, where hydraulic conductivity is infinite (Englert, 2003). Thus, due to the convergence of the streamlines, the tracer solution in the borehole is faster exchanged with fresh water from the up-stream than in the surrounding area in the aquifer.

Generally, the tracer plume showed a downward drift to the middle and lower part of the aquifer till 17 days after injection and afterwards some tendency of moving upward as it was observed in the first cross section, too. At greater distances from the injection well (day 21) the tracer plume is insufficiently resolved and after 35 days of monitoring the contrast is too low to reveal a distinct signal-to-noise contrast caused by the tracer. Higher resistivities are still observed with ERT in the vicinity of the boreholes but not in the region between the boreholes where the sensitivity of the ERT imaging is considerable reduced (cp. Figure 3-10).

One important reason for the insufficient resolution in particular in the parallel profile is the 2D approximation of the solute plume for the inversion of resistance measurements. The assumption of constant resistivities perpendicular to the cross sectional image plane is problematic for the parallel profile due to the minor perpendicular extension of the tracer plume. Furthermore the local MLS data showed that with increasing distance, the tracer solution was detected in MLS which were situated more westward from the mean flow direction and the parallel profile, respectively. This points out that the assumption of constant resistivities perpendicular to the mean flow direction was not given.

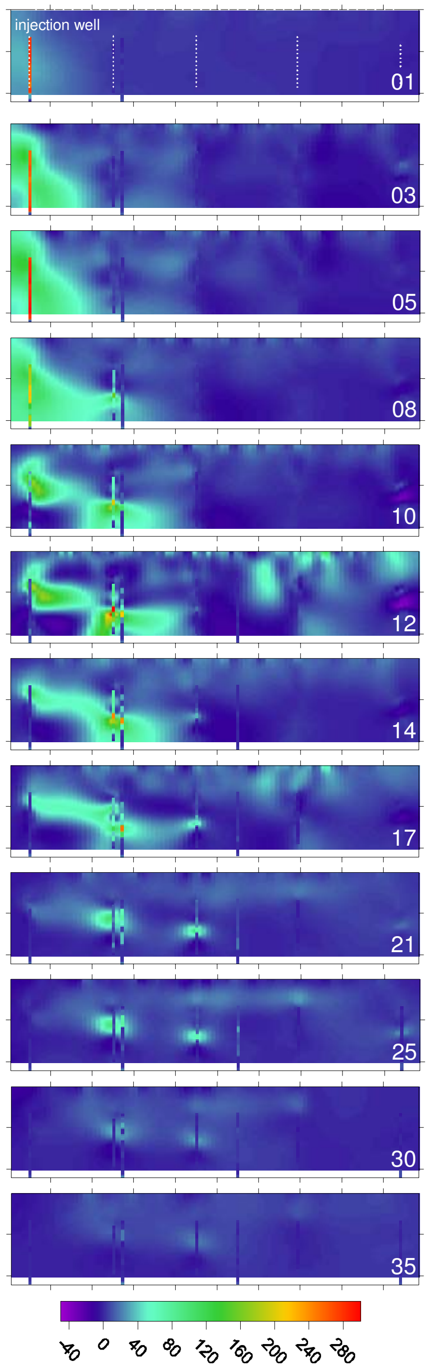

Figure 3-10: Temporal plots of relative changes in bulk aquifer resistivity ρ (ERT) and conductivity EC_b (columns = MLS), respectively, in [%] at the parallel profile ('negative' test).

3.2.4.2 Comparison of Local Breakthrough Curves

Besides the imaging of relative changes in resistivity or conductivity at cross sections, another method to compare ERT with MLS is to plot absolute breakthrough curves derived from groundwater multilevel sampling together with the ERT derived breakthrough curves in the corresponding pixels in the image plane. Based on the results presented in section 3.2.3 where calibration relations for a set of sand-gravel mixtures that cover the aquifer heterogeneity are presented a formation factor a=0.18 was chosen for the calculations of the bulk soil conductivity from multilevel solute conductivity measurements. The results generated with a formation factor of 0.15 showed only slight differences concerning to the peak magnitude. Generally the best fit with the ERT pixel breakthroughs was gained with a formation factor of 0.18.

Figure 3-11 to 3-14 show calculated breakthrough curves of two selected observation wells, borehole 26 and 61, in the first perpendicular profile for the 'positive' and 'negative' tracer test, respectively. Borehole 26 and 61 are located 10 m downstream of the injection well. Well B 26 is located in the expected trajectory of the tracer plume's center of mass whereas well B 61 is 3 m laterally from it.

In the 'positive' tracer test (Figure 3-11 and 3-12) the main tracer mass was detected by both the MLS and ERT in the middle and lower parts of the aquifer. In well 26, the breakthrough curves obtained with the MLS show higher peak concentrations in the upper part of the aquifer than the ERT derived breakthrough curves (MLS 12 and 16 at 6.38 m and 7.58 m). Furthermore an earlier breakthrough was observed in MLS 12 compared to the ERT derived breakthrough curve. The BTCs derived from the lowest parts in the aquifer show a good agreement between MLS and ERT concerning to peak magnitude and shape of the BTCs. As a result of the longer travel distance and the location more aside from the expected center of mass of the plume, the BTCs in well 61 show generally lower peak concentrations than those in well 26. In contrast to the observations in borehole 26, the ERT breakthrough curves show earlier arrival times than the MLS derived BTCs. Moreover, the MLS derived BTC show longer lasting tailing in the lower aquifer zone.

Figure 3-13 shows selected BTCs measured during the 'negative' tracer test in well 26. The main tracer mass was detected in the middle aquifer zone. As observed before in the 'positive' tracer test the MLS derived BTCs show earlier arrival times in the middle part of the aquifer (MLS 8 and 12 at 5.18 and 6.38 m). But concerning to the magnitude and shape the BTC MLS and ERT fit well. The best correlation between MLS and ERT was observed for the MLS 16 and 20 and depth between 7.58 and 9.38 m below the surface.

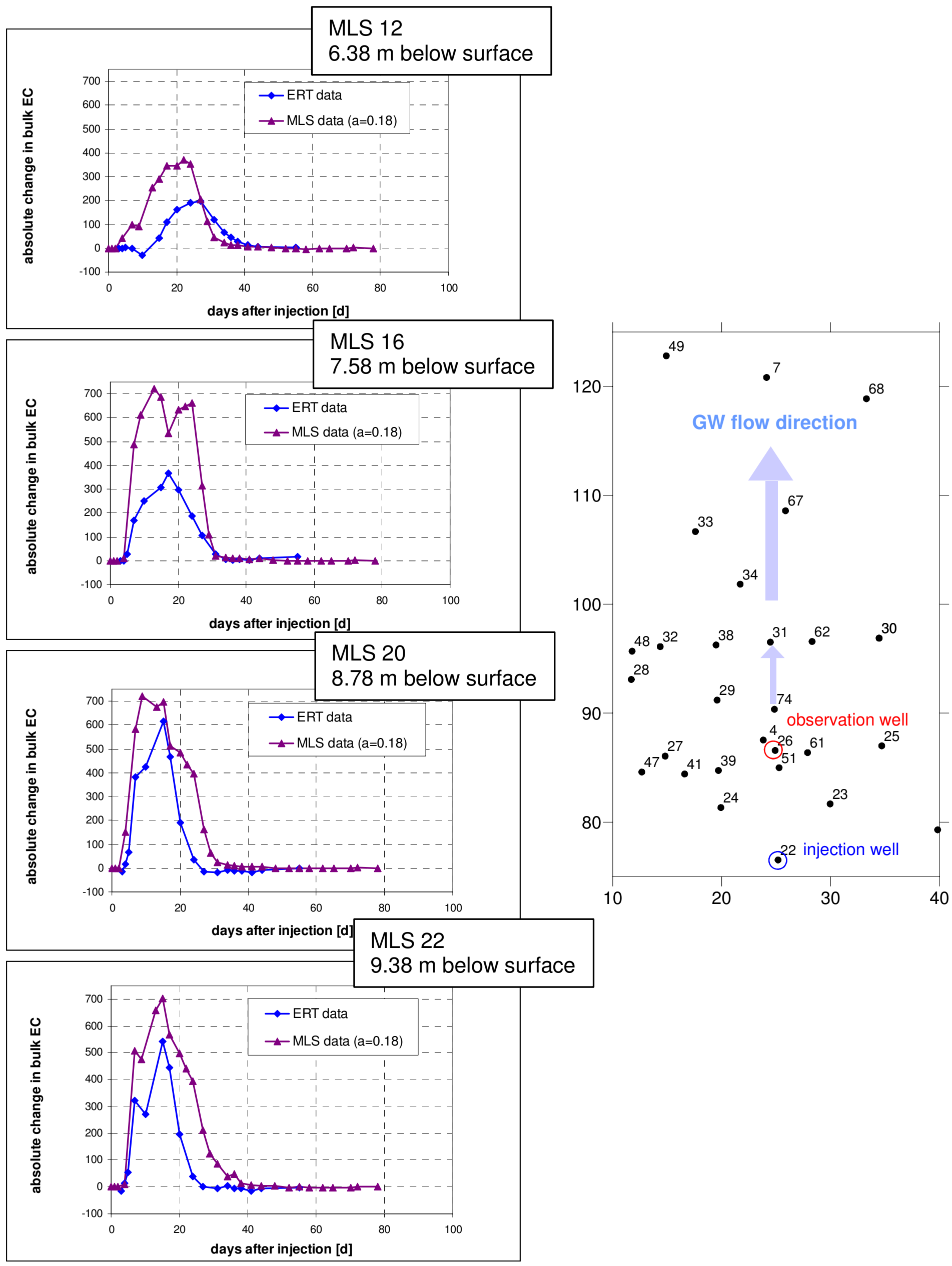

Figure 3-11: BTCs of absolute changes in bulk electrical conductivity [$\mu S \cdot cm^{-1}$] compared to the background conductivity derived from solute samples of MLS and the corresponding ERT pixels of borehole 26 during the 'positive' tracer test 2002.

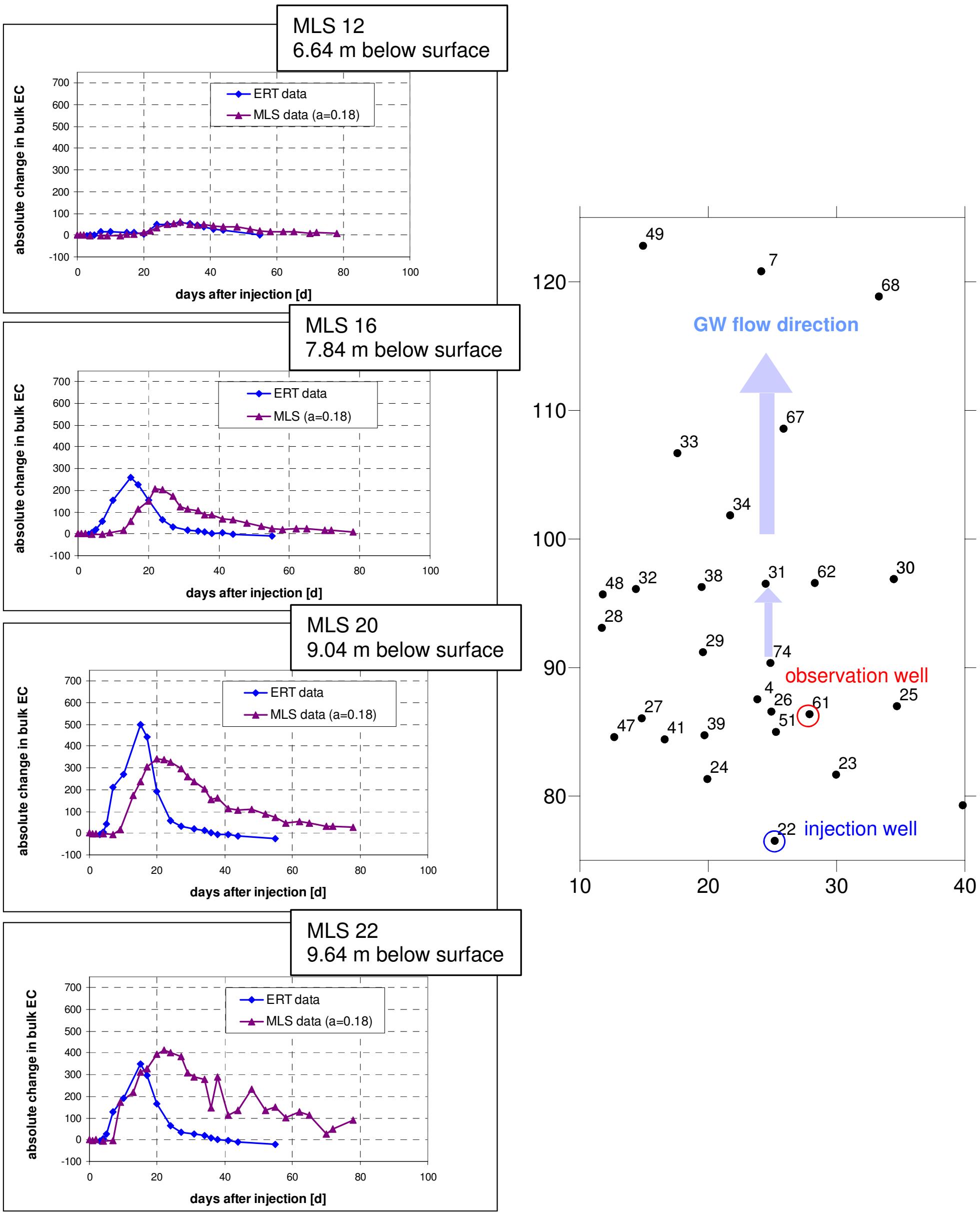

Figure 3-12: BTCs of absolute changes in bulk electrical conductivity [$\mu S{\cdot}cm^{-1}$] compared to the background conductivity derived from solute samples of MLS and the corresponding ERT pixels of borehole 61 during the 'positive' tracer test 2002.

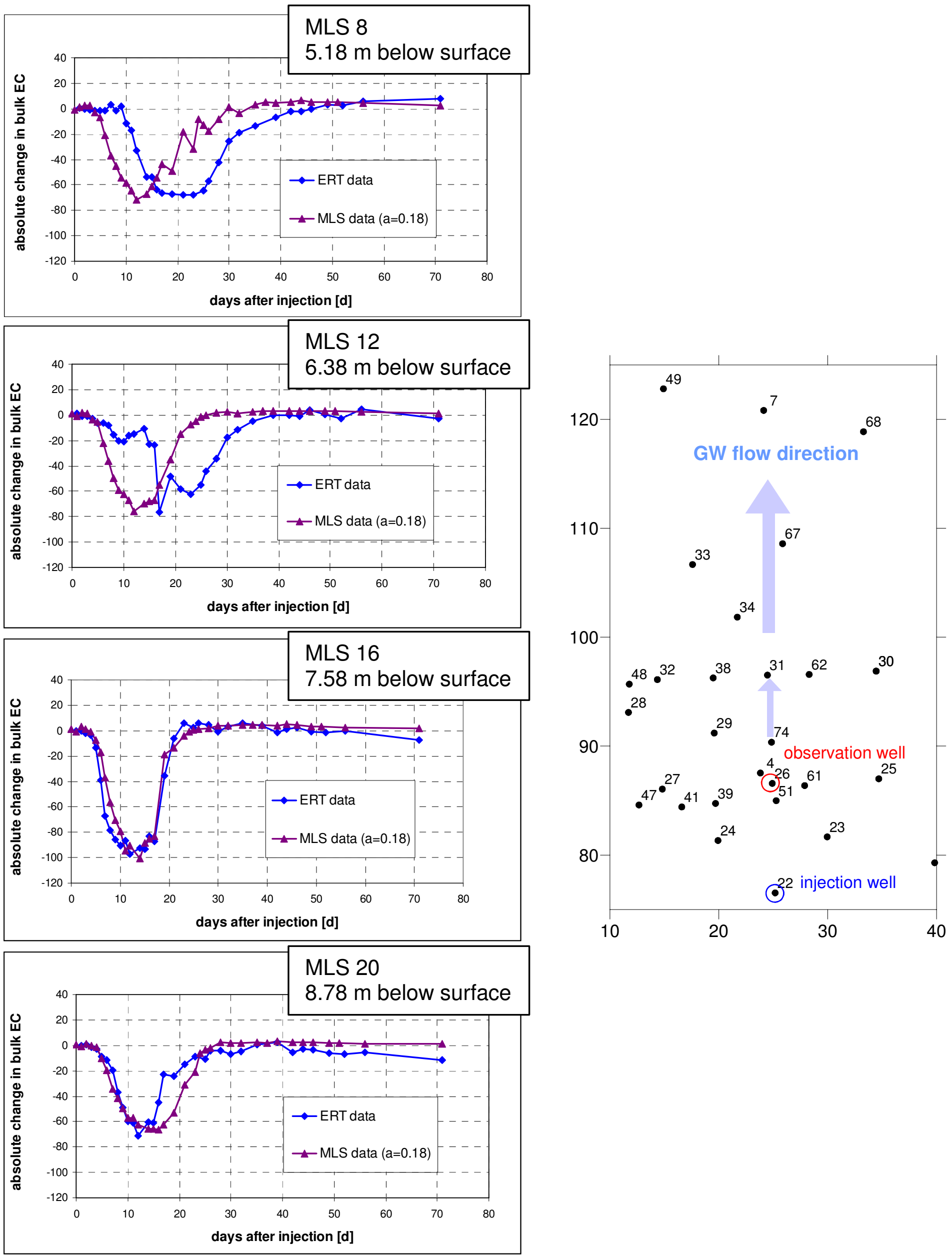

Figure 3-13: BTCs of absolute changes in bulk electrical conductivity [$\mu S \cdot cm^{-1}$] compared to the background conductivity derived from solute samples of MLS and the corresponding ERT pixels of borehole 26 during the 'negative' tracer test 2003.

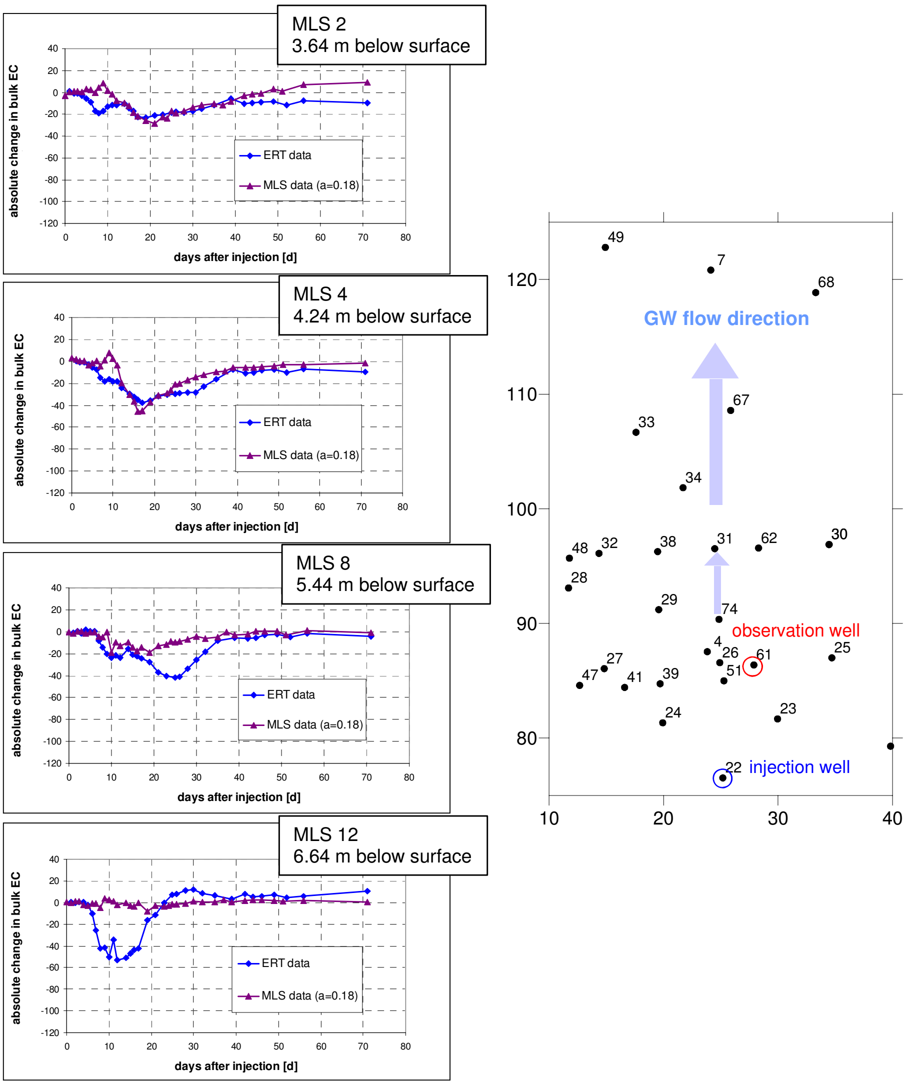

Figure 3-14: BTCs of absolute changes in bulk electrical conductivity [µS·cm^{-1}] compared to the background conductivity derived from solute samples of MLS and the corresponding ERT pixels of borehole 61 during the 'negative' tracer test 2003.

In Figure 3-14 the BTCs during the 'negative' tracer test in well 61 are shown. In analogy to the 'positive' tracer test, the contrast between the tracer peak and the background conductivity is smaller than in borehole 26. However, in contrast to the 'positive' tracer test only in the uppermost MLS of borehole 61 a breakthrough was detected whereas with ERT the main breakthrough was observed in the middle aquifer zone. The agreement between ERT and MLS breakthrough curves is clearly less good in this well and experiment. It should be noted that the ERT data show more consistency between the 'positive' and 'negative' tracer tests for this well.

Reasons for the different results between both methods are on the one hand the different spatial resolution of ERT and MLS and on the other hand the different volume that is sampled with MLS compared to the ERT pixel volume for which EC_b is estimated in the ERT inversion. Moreover Vanderborght et al. (2005) showed with synthetic experiments that such differences are not unexpected in heterogeneous aquifers. Another aspect which can be considered as an explanation for unexpected differences, are artifacts that are generated by the well and filter material around the well. These artifacts may influence the multilevel sampling considerably. The tailing or very slow removal of high concentrations in the deeper part of the aquifer are indications of these artifacts. Also the difference between the positive and negative tracer test which was observed in borehole 61 is an indication of such artifacts.

3.2.4.3 Comparison of 'positive' and 'negative' Tracer Plumes

The breakthrough of both the 'negative' and the 'positive' tracer was clearly resolved with ERT in the first cross section which was already shown in Figure 3-8. The arrival times of the tracer solutions were similar with a slightly more distinct breakthrough for the 'positive' tracer. After 10 days the tracer cloud was horizontally separated in two parts due to large scale heterogeneity. The 'negative' tracer moved primarily through the middle central part in the ERT image plane whereas the 'positive' tracer sank density driven down to the lower central part of the ERT image plane. Generally, the downward sinking of the 'positive' tracer was accompanied by more lateral spreading while the lower part of the 'negative' cloud showed an upward trend. For the 'positive' tracer a pronounced tailing was observed. For both experiments the breakthrough in the upper and middle part was delayed in comparison to the breakthrough in the lower part of the aquifer.

3.2.5 Recovered Tracer Mass

Based on the theoretical explanations (cp. subsection 3.1.5) the recovered tracer mass derived from the ERT data sets at the first cross section was calculated for the 'positive' tracer test. For the 'negative' tracer test 2003 mass balances at the first and second cross section were calculated.

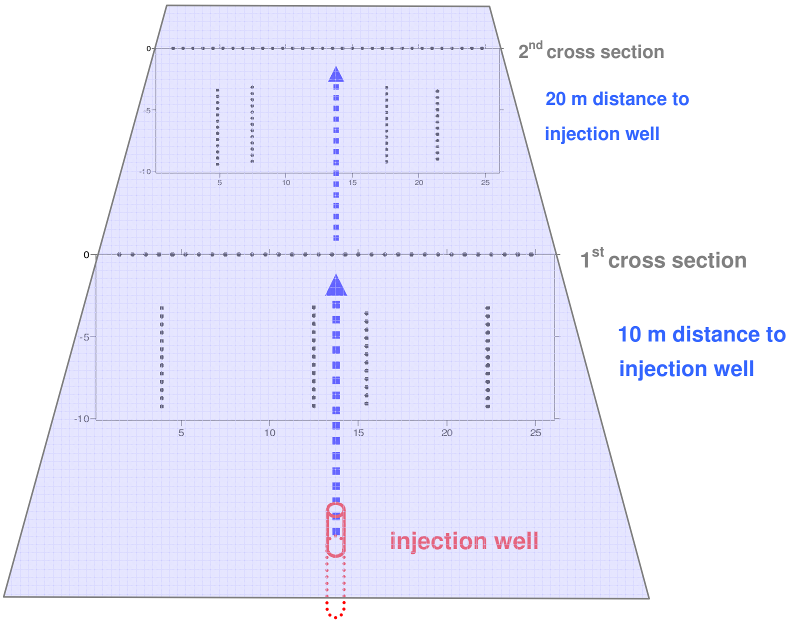

Figure 3-15: Schematic figure of the test site with the two reference planes.

Concerning to both tracer tests a mean formation factor of $a = 0.18$ was chosen and a mean intercept $b = 17.5 \mu S \cdot cm^{-1}$. One ERT voxel was about 0.075 m². The time of injection was 7 days. The initial background conductivity was determined from groundwater multilevel sampling in the run-up to the tracer tests. The mean Darcy flow velocity was given by the analysis of the equivalent transport parameters. The mean total porosity of the Krauthausen aquifer was set to 0.27. As introduced in subsection 3.1.3 the ERT data needed to be standardized to 25℃ by a temperature correction factor of 1.365.

The results of the mass balances are summarized in the following tables. For the 'positive' tracer test, 69 % of the tracer mass was recovered at the first cross section with ERT. Approximately the same amount was found for the 'negative' tracer test at the first cross section. The resolution of the ERT measurements was similar for both experiments.

Table 3-2: Mass balance results at the first cross section ('positive' tracer test).

First cross section 2002 ('positive' tracer test)				
$EC_{w(ini)}$ [µS·cm^{-1}]	**<q>** [m·d^{-1}]	**injected tracer mass $CaCl_2$** [kg]	**recovered tracer mass** [kg]	**recovered tracer mass** [%]
916	**0.22**	**400**	**276**	**69**

Table 3-3: Mass balance results at the first cross section ('negative' tracer test).

First cross section 2003 ('negative' tracer test)				
$EC_{w(ini)}$ [µS·cm^{-1}]	**<q>** [m·d^{-1}]	**injected tracer 'mass'** [µS·cm^{-1}·m^3]	**recovered tracer 'mass'** [µS·cm^{-1}·m^3]	**recovered tracer 'mass'** [%]
888	**0.25**	**89 320**	**61 871**	**68**

Table 3-4: Mass balance results at the second cross section ('negative' tracer test).

Second cross section 2003 ('negative' tracer test)				
$EC_{w(ini)}$ [µS·cm^{-1}]	**<q>** [m·d^{-1}]	**injected tracer 'mass'** [µS·cm^{-1}·m^3]	**recovered tracer 'mass'** [µS·cm^{-1}·m^3]	**recovered tracer 'mass'** [%]
888	**0.24**	**89 320**	**12 483**	**14**

For the second cross section the recovered tracer mass was only 14 % of the injected tracer mass. The small amount of recovered tracer mass at the second cross section can be explained by the lower resolution at this cross section due to the electrode configuration and the signal to noise ratio was lower at the second cross section.

3.2.6 Comparison of Equivalent Transport Parameters

To characterize the heterogeneity of the transport processes we used the one-dimensional stream tube model approach. Solute transport within the plume was quantified by the equivalent stream tube velocity v_{eq} and the equivalent dispersivity λ_{eq}. The equivalent parameters were derived from the ERT data sets generated at the first cross section for the 'positive' tracer test and at the first and second cross section for the 'negative' tracer test. Furthermore the multilevel sampling data from boreholes situated in the cross sectional area of the first and second reference plane were analyzed as well. The results are illustrated in the following tables and figures.

Figure 3-16 shows the zeroth moment of the electrical conductivities measured with ERT at the first cross section. For both tracer tests the initial EC_b was subtracted from the measured EC_b at time t. So, the plots show the absolute values of the difference between $EC_{b(ini)}$ and EC_b. For the 'positive' tracer test the highest amount in conductivity was measured between borehole 26 and 61 in a depth of 8 and 9 m below the surface. There is a second layer with higher conductivity but less distinct contrast in the middle to upper part of the aquifer ranging from 4 to 5 m below the surface.

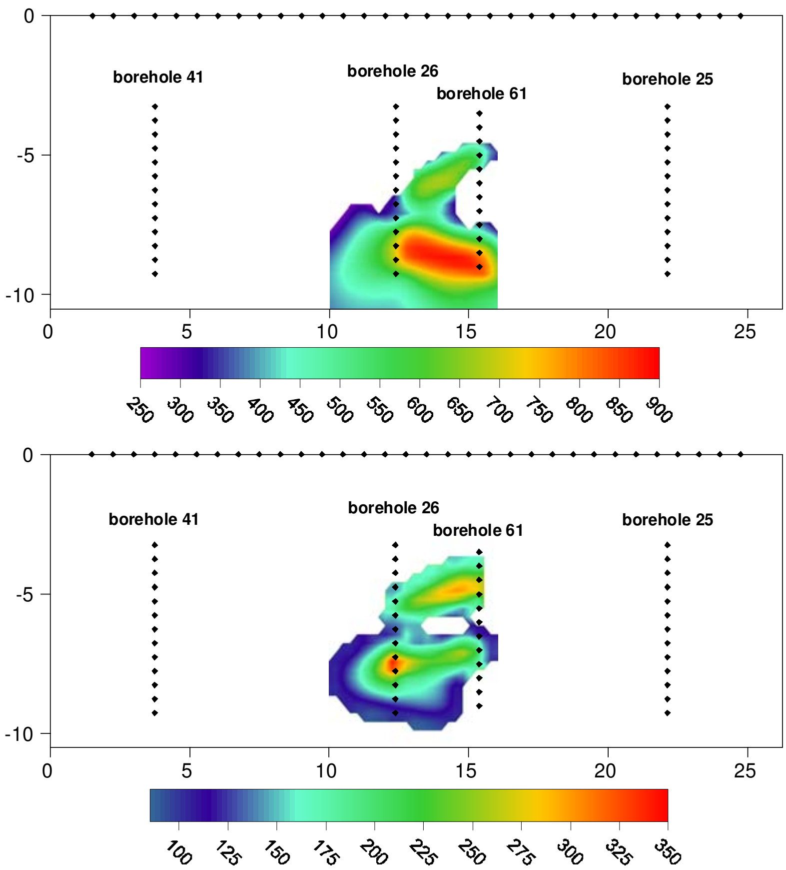

Figure 3-16: Zeroth moment of the ERT derived electrical conductivity in [µS · cm^{-1} · d] at the first cross section. Above: 'positive' tracer test 2002, below: 'negative' tracer test 2003. Dots mark the position of borehole and surface electrodes, respectively.

A similar separation of two horizontal layers was detected in 2003 as a result of aquifer heterogeneity. Due to the lower density of the 'negative' tracer the relative amount of conductivity detected in the upper zone between the boreholes 26 and 61 is higher compared to the 'positive' test.

Figure 3-17 shows the stream tube velocities in cut-outs of the first cross section together with velocities derived from groundwater multilevel sampling data. In both, the 'positive' and 'negative' tracer tests, the equivalent stream tube velocity derived from the ERT data sets are higher in the lower part of the aquifer. The equivalent velocities derived from the 'negative' tracer test are generally higher than those derived from the 'positive' test. The equivalent velocities derived from groundwater multilevel sampling are in a broad area in rough accordance with the ERT results but some differences obviously exist. For instance, the multilevel samplers show that the breakthrough occurs faster in the lower part of the aquifer. But the deviations between MLS and ERT are not consistent for the two experiments. For example, in well 4, there is a rapid breakthrough during the 'positive' tracer test between 4 and 5 m depth. This is not observed in the 'negative' test neither in the ERT data. In well 26, there is a slower breakthrough during the 'positive' experiment between 4 and 7 m below the surface than in well 4 whereas the opposite is true for the 'negative' tracer test. These inconsistencies in the MLS data point at some fundamental problems with using such local sampling methods to monitor tracer tests and characterize transport in heterogeneous aquifers.

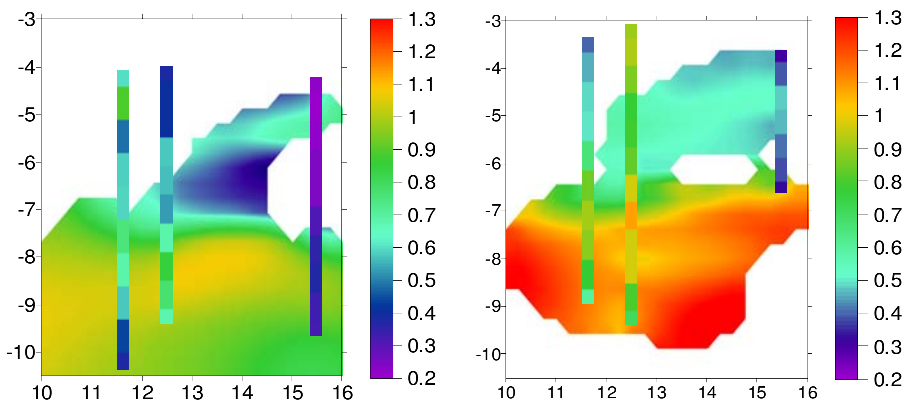

Figure 3-17: Equivalent stream tube velocities in [$m \cdot d^{-1}$] derived from ERT data and complemented with MLS (cut-out from the first cross section with boreholes 4, 26 and 61 from left to right). Left plot: 'positive' tracer test, right plot: 'negative' tracer test.

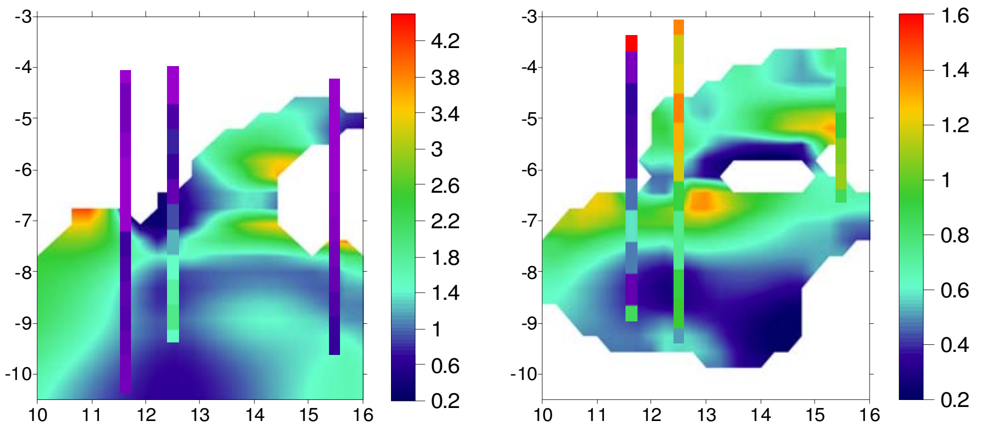

Figure 3-18: Equivalent stream tube dispersivities in [m] derived from ERT data and complemented with MLS (cut-out from the first cross section). Left plot: 'positive' tracer test, right plot: 'negative' tracer test.

Figure 3-18 shows the equivalent dispersivities estimated with the stream tube model approach. The ERT equivalent dispersivities for the 'positive' and 'negative' tracer test show a good correlation concerning to the distribution of higher and lower dispersivities but differences in the magnitude. For the 'positive' tracer test the equivalent dispersivity values range between 0.2 and 4.5 m compared to 0.2 to 1.6 m for the 'negative' tracer test. Estimated equivalent dispersivities derived from groundwater samples of the 'positive' tracer test are extremely low. For the 'negative' tracer test the multilevel data show a rough accordance with the ERT data but for well 26 the dispersivities are about factor 2 higher than the ERT derived equivalent values. Vanderborght et al. (2005) showed in synthetic experiments that stream tube dispersivities from ERT data can be considerable larger than the actual ones. This is especially so in regions with gradients in the stream tube velocities. The same is actually observed in these tracer experiments.

For the second cross section only the data sets from the 'negative' tracer test were inverted and analyzed with the stream tube model approach. The zeroth moment is shown in Figure 3-19. Only in the immediate vicinity of borehole 31 which was equipped with ERT borehole electrodes tracer mass was detected, mainly in the middle aquifer zone.

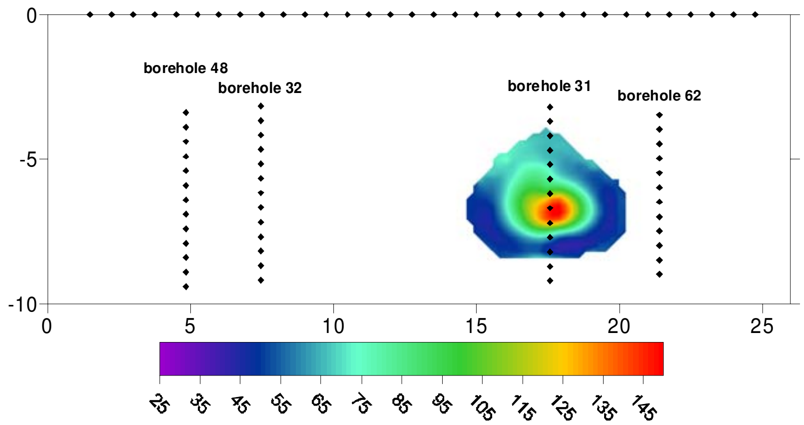

Figure 3-19: Zeroth moment of the ERT derived electrical conductivity in [µS·cm^{-1}·d^{-1}] at the second cross section ('negative' tracer test 2003).

The estimated equivalent parameters are mapped in Figure 3-20. The ERT derived equivalent velocity shows a horizontal zoning with lower velocities in the middle and upper part of the aquifer whereas the results of the multilevel sampling stream tube analysis show a more or less uniform velocity over the entire aquifer thickness. Both, ERT and MLS, show a layer with higher dispersivity in a depth of 6 to 7 m below the surface compared to the area above and below this zone. Generally MLS derived higher equivalent velocities than ERT but lower dispersivities. Again, the ERT derived dispersivities seem to be larger in regions where the gradients in the stream tube velocities is large. To point out the quantitative results of both experiments the estimated values are summarized in the following table.

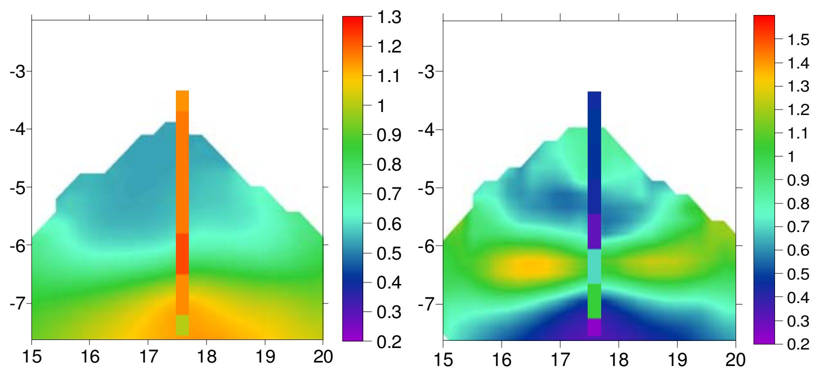

Figure 3-20: Equivalent stream tube velocity [m·d^{-1}] and dispersivity [m] derived from ERT data and complemented with MLS data (cut-out from the second cross section).

Table 3-5: Equivalent stream tube parameter for the first and second cross section (equivalent velocity $\left\langle v_{eq} \right\rangle$ in [m/d], equivalent dispersivity $\left\langle \lambda_{eq} \right\rangle$ and advective dispersivity $\left\langle \lambda_{adv} \right\rangle$ in [m]).

first cross section

	$<v_{eq}>$		$\sigma^2 v_{eq}$		$<\lambda_{adv}>$		$<\lambda_{eq}>$	
	2002	**2003**	**2002**	**2003**	**2002**	**2003**	**2002**	**2003**
MLS	0,48	0,69	0,04	0,06	1,05	0,74	0,91	1,44
ERT	0,81	0,94	0,04	0,08	0,63	0,71	1,51	0,6

second cross section

	$<v_{eq}>$		$\sigma^2 v_{eq}$		$<\lambda_{adv}>$		$<\lambda_{eq}>$	
	2002	**2003**	**2002**	**2003**	**2002**	**2003**	**2002**	**2003**
MLS	0,78	1,11	0,02	0,01	0,32	0,06	1,34	0,51
ERT		0,87		0,06		0,70		0,88

$\left\langle \lambda_{adv} \right\rangle$ is the advective dispersivity which is defined as:

$$\left\langle \lambda_{adv} \right\rangle = \frac{x \cdot \sigma_t^2 \left\langle 1/v_{eq} \right\rangle}{2 \cdot \mu_t \left\langle 1/v_{eq} \right\rangle^2} \qquad \text{Eq. 3-24}$$

where x is the distance to the injection well.

3.3 Conclusions and Discussion

In the first part of the thesis the tracer tests conducted at the Krauthausen test site were investigated to improve the applicability of Electrical Resistivity Tomography (ERT) to characterize and quantify subsurface transport processes in a heterogeneous aquifer. The spatio-temporal evolution of the tracer plume was monitored with ERT at two cross sections perpendicular to the mean flow direction and at one parallel profile in flow direction. The breakthrough of both, the 'positive' and the 'negative' tracer plume was clearly resolved in the cross sectional ERT image planes. With regard to the parallel profile the ERT images were influenced by the 2D approximation of the 3D electrical conductivity distribution. The tracer seemed to 'disappear' in the middle between two boreholes and 'reappears' in regions closer to the boreholes.

The breakthrough curves and the spatial pattern of the transport processes that were observed in two comparably conducted tracer tests were similar, which demonstrates that the tracer test results are quite reproducible. Both tracer tests displayed a vertical separation in an upper and lower part of the tracer plume which was clearly monitored with ERT at the first cross section. Nevertheless, there were some differences between the two experiments due to density driven flow of the 'positive' tracer. The tracer plume sank down and moved primarily through the lower parts of the aquifer which lead to an apparent larger stream tube dispersion in the bottom part of the aquifer and a larger lateral spreading. During the 'negative' tracer test the maximum amount of tracer was monitored in the middle aquifer region where less spreading was observed.

The comparison of ERT pixel breakthroughs with corresponding multilevel sampling data showed a good agreement of the arrival times and peak magnitudes of the tracer. However, some obvious differences existed. Besides the smaller sampling volume of the MLS technique compared with the spatial resolution of the ERT technique, differences between the MLS and ERT may also result from artifacts in the MLS technique. The small reproducibility of the tracer transport observed with MLS during the two tracer tests suggests that this measurement technique may be prone to artifacts. Also the very slow flow velocities in the lowest part of the aquifer monitored during the 'positive' tracer test are an indication for an artifact caused by the construction and screening of the observation wells that has a strong influence on the transport processes at the bottom of the aquifer. Furthermore, the resolution of an image which needs to be reconstructed from a rather sparse grid of local concentration measurements with multilevel samplers is considerably lower than the resolution of a concentration image that is derived from an ERT data set.

The spatio-temporal information that was gained with ERT and MLS was interpreted by means of a one-dimensional equivalent STM to quantify the observed heterogeneity of the transport processes. The spatial variability of the transport parameters is related to the spatial hydraulic conductivity distribution at the test site. Regions with lower equivalent velocities correspond to sediments with lower hydraulic conductivity. With regard to the first cross section the equivalent velocities derived in 2003 from the 'negative' tracer test were similar concerning to their distribution but showed higher values than the corresponding velocities derived from the 'positive' tracer test. One reason could be that the 'negative' tracer was transported through other flow paths than the 'positive' tracer. Furthermore, with regard to the chemistry, negative charged chloride ions would preferably flow through regions with higher flow velocities in the central part of the pores. Therefore one could have expected the opposite behavior concerning the derived flow velocities. This is once more an argument for the assumption that the 'positive' tracer solution behaves as an conservative tracer.

The MLS derived velocities showed a rough accordance with the ERT velocities. The correspondence of the stream tube dispersivities that were derived by ERT and MLS was considerable smaller. The dispersivities are expected to be overestimated with ERT which was verified in synthetic experiments (Vanderborght et al., 2005). This overestimation of stream tube dispersivities was shown to be related to lower spatial resolution of the ERT imaging technique leading to an averaging and smearing out of the local breakthrough curves, especially in those regions where the local gradients in stream tube velocity are large. It should be noted that the spatial resolution of the ERT images is dependent on the chosen model parameters like model contrast, error noise and electrode configuration.

The tracer mass recovered with ERT was calculated for both experiments at the first cross section and for the 'negative' tracer test at the second cross section. For the 'positive' tracer test 69 % of the injected tracer mass was recovered at the first cross section. For the 'negative' tracer test 68 % of the mass was found at the first cross section and 14 % percent at the second cross section. The small mass recovery at the second cross section can be explained by the lower ERT resolution caused by the electrode configuration and the lower signal to noise ratio in the second cross section.

4 3D Numerical Flow and Transport Simulations Based on a Deterministic Aquifer Model

4.1 Methods

This section presents three-dimensional numerical simulations of the 'positive' tracer experiment. The simulations were done based on a deterministic aquifer model of the Krauthausen aquifer which was derived from Cone Penetration Tests (CPT) and then compared with the two field tracer tests at Krauthausen.

Cone Penetration Tests

Cone penetration testing (CPT) permits rapid and less expensive exploration of shallow subsurface conditions by logging various physical parameters simultaneously. This exploration method employs sensors that are pushed into the ground to infer the properties of the soil in situ. Due to the small diameter of the cone that is pushed into the ground the geological structure is hardly deformed. Known as direct-push technology, this method can map out the vertical and lateral extent of stratigraphic layers, as well as the distribution of subsurface contaminants down to a depth of 20-30 m in unconsolidated sediments.

Within a scientific co-operation between the FORSCHUNGSZENTRUM JÜLICH GmbH and the EÖTVÖS LORÁND Geophysical Institute of Hungary, the ELGOSCAR 2000 Ltd. performed cone penetration tests at the Krauthausen test site during two surveys in 2003 and 2004. The aim of the surveys was to explore the near surface structure in order to make a precise deterministic model of the subsurface structure and investigate the statistical spatial distribution of the soil material properties (Tillmann et al., 2005).

At the Krauthausen test site 77 cone penetration tests were performed down to a maximum depth of 16 m below the surface. The tests were conducted in a central area of 30 by 20 m. The exact location of the penetration points is shown in Figure 4-1. With CPT highly resolved measurements of physical parameters are carried out either during the pushing process with sensors placed on the tip of the pipe or after the pushing using probes that are moved inside the pipes (Tillmann et al., 2005). The parameters determined with CPT at the test site were the mechanic cone pressure c_r [MPa], the bulk electrical resistivity ρ [Ωm], the natural gamma activity γ [counts per minute] which depends on the clay content, the attenuation of a gamma ray which is related to the bulk density ρ_b [kg · m^{-3}] and the neutron attenuation which can be correlated to the water content θ [Vol.%]. The electrical resistivity was available at 15 locations.

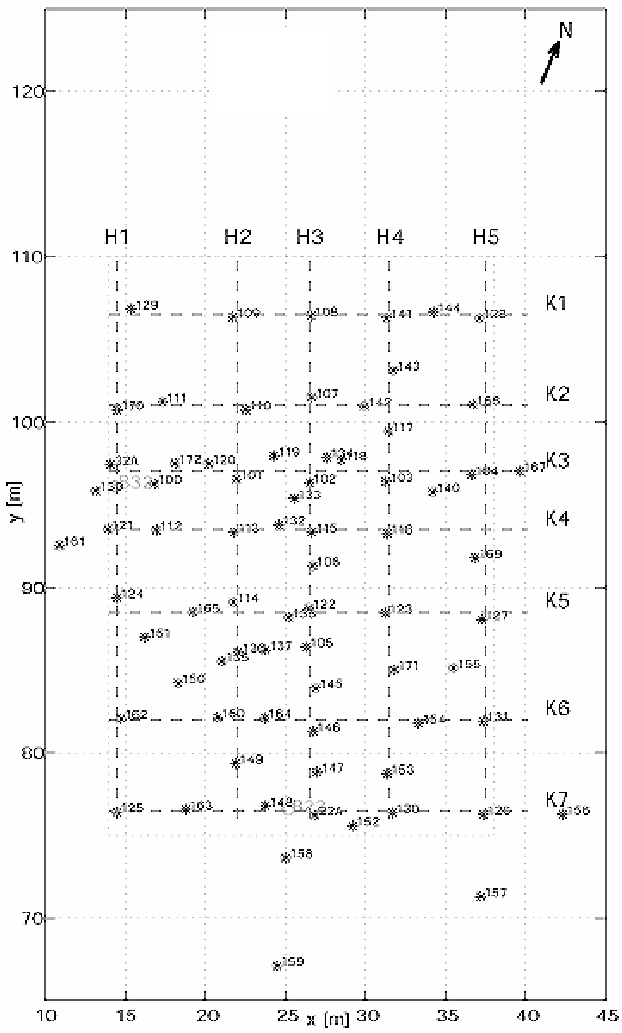

Figure 4-1: Locations of the cone penetration tests. Section K3 corresponds to the second cross section measured with ERT (Tillmann et al., 2005).

Derivation of the Heterogeneous Hydraulic Conductivity Field

In a first step the raw data derived from the CPT were correlated to physical parameters which can be correlated to the water content θ using appropriate calibration functions. Based on the distribution of the physical soil parameters a distinction in geological sections was done. The stratigraphy turned out to be horizontal layered (Tillmann et al., 2005).

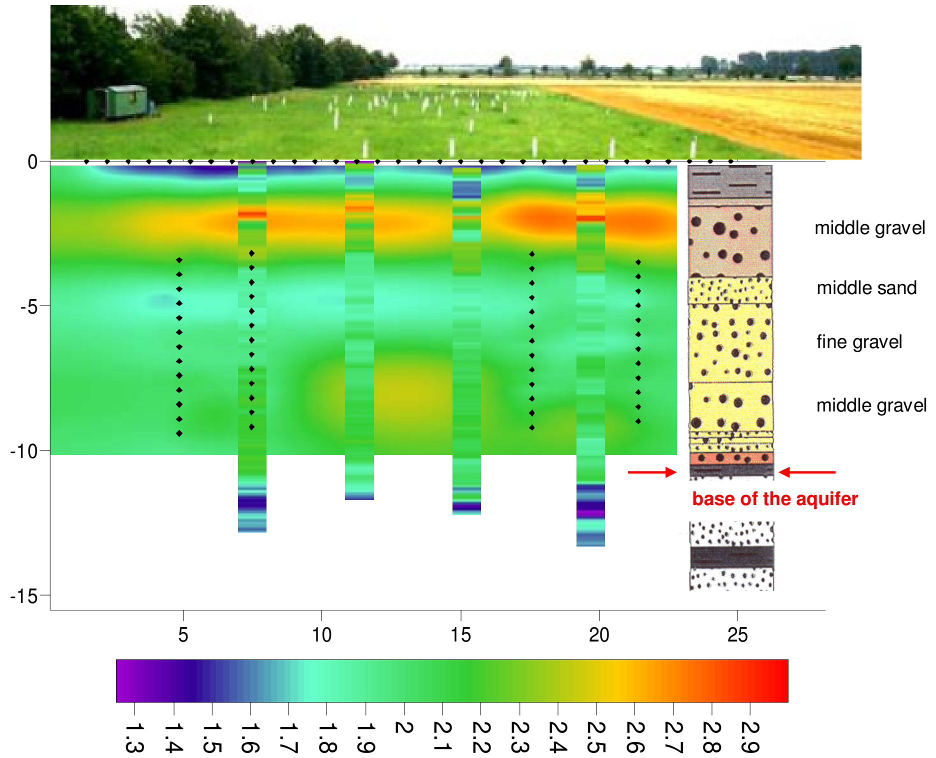

Figure 4-2: Picture of the test site at the top, schematic and idealized lithological profile of the Krauthausen aquifer at the right and an ERT map of the natural bulk electrical resistivity [$\log_{10}$ Ωm] at the second cross section complemented by CPT logs (vertical bars). The black dots mark the location of the ERT surface and borehole electrodes, respectively (Gößling, 2004).

In Figure 4-2 some selected CPT logs where the electrical resistance was available are implemented in an interpolated map of the natural electrical resistance measured with ERT at the second cross section. At the right side of the image a schematic profile of the lithology at the test site is shown. In the upper part of the aquifer a layer with very high resistivities about 650 (ERT) and 750 Ωm (CPT) is observed. This layer corresponds to unsaturated coarse gravels. In a depth of approximately 2 m below the surface the groundwater table is situated. The CPT logs show a rapid decrease of the resistivity due to the saturation of the soil below 2 m depth. With ERT, it is not possible to resolve distinct layer boundaries. Between 4 and 5 m below the surface, ERT as well as CPT derived a layer with higher resistivities of 150 Ωm. This layer can be related to sandy sediments, mainly middle sand. Down to the bottom of the aquifer the correlation between ERT and CPT is less good in between the boreholes in the middle part of the profile. This can be explained by the smaller sensitivity of ERT measurements in this region which causes inversion artifacts. The CPT logs reached to a depth of 13 m below the surface which allowed the determination of the aquifer bottom.

In a second step the CPT data were correlated to parameters that characterize the grain size distribution and that were derived from sieving analysis of sediment from three completely sampled drilling cores. For the sieving analysis, the sediment of the drilling cores was divided in intervals of 10 cm. Using an approach of Bialas and Kleczkowski (1970) the grain size distribution could be related to the hydraulic conductivity distribution:

$$\mathbf{K} = 0.0036 \cdot {d_{20}}^{2.3}, \qquad \text{Eq. 4-1}$$

where the hydraulic conductivity **K** is a function of the effective grain size diameter d_{20}. The 20th percentile d_{20} represents the diameter where the cumulative grain size distribution has the value 0.20. The grain size diameter d_{20} was derived from CPT data using an empirical relation. This relation was determined by correlating $\log_{10} d_{20}$ derived from sieving analysis of the drilling core samples (Döring, 1997) to CPT logs very close to the selected drillings using a multiple linear regression analysis. The highest absolute correlation coefficients were derived for the mechanical cone resistance c_r, the natural gamma activity γ and the bulk density ρ_b (Tillmann et al., 2005). To estimate the error prediction, the predicted diameter $d_{p,20}$ was correlated with the diameter d_{20} gained from the cumulative grain size distribution. The resulting correlation coefficient was 0.737 with a standard deviation of 0.303. Once the diameter d_{20} was derived from the field data, Eq. 4-1 could be used to estimate the hydraulic conductivity at the CPT locations. The resulting empirical equation to derive the hydraulic conductivity from the CPT data sets at the test site is given by.

$$\mathbf{K} = 10^{2.438 \cdot 10^{-2} c_r - 1.927 \cdot 10^{-4} \gamma + 3.611 \rho_b - 18.222} \qquad \text{Eq. 4-2}$$

In a third step the local CPT derived values for $\log_{10} \mathbf{K}$ were interpolated linearly using the algorithm of Barber et al. (1996) to produce the three-dimensional distribution of the hydraulic conductivity at the test site. Figure 4-3 shows two vertical cuts and one horizontal cut through the CPT derived three-dimensional hydraulic conductivity distribution. The vertical cuts belong to the profiles H3 and K3 shown in Figure 4-1, the horizontal cut belongs to a depth of 90 m above sea level and 8.4 m below the surface at the test site. The vertical cuts reproduce the layered structure of the aquifer. The horizontal cut shows the lateral heterogeneity within the layer.

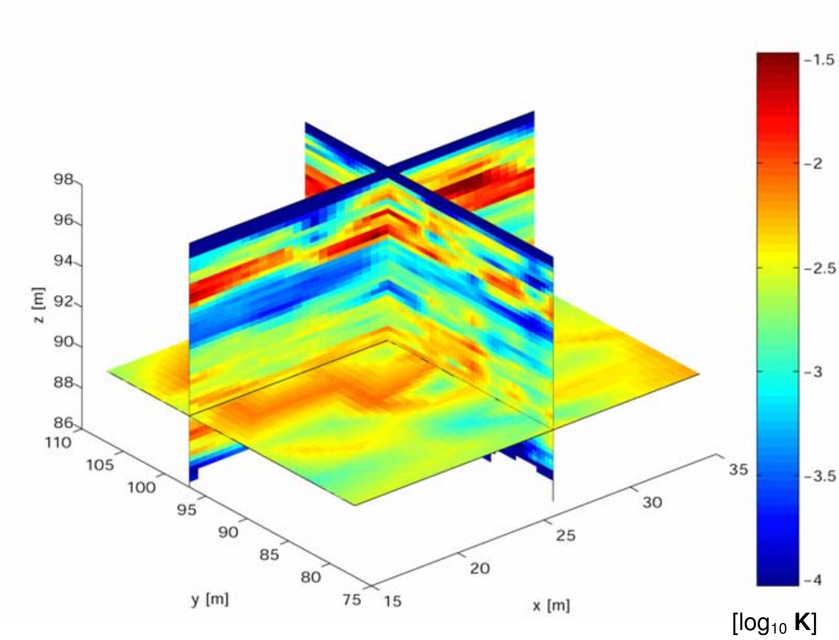

Figure 4-3: Three cuts through the CPT derived three-dimensional hydraulic conductivity field at the test site. The z-coordinate is given in [m NN].

The estimation of the three-dimensional hydraulic conductivity distribution derived a very low conductive layer in the upper zone with 10^{-4} m/s which corresponds to the top pseudogley layer. In a depth between 94 and 96 m above sea level a layer with intensive red colors and high conductivities of 10^{-2} m/s is observed which can be related to the unsaturated coarse gravels. Below this layer in the middle aquifer zone the hydraulic conductivity shows a fast decrease compared to the layers above due to saturation. Down to the base of the aquifer the hydraulic conductivity increases again.

4.2 Numerical Simulations

4.2.1 3D Numerical Flow and Transport Model TRACE/PARTRACE

The AGROSPHERE of the FORSCHUNGSZENTRUM JÜLICH GmbH developed the software package TRACE/PARTRACE (Neuendorf, 1996, Seidemann, 1996) to model three-dimensional flow and transport processes in soils and aquifers. The finite element model TRACE solves the three-dimensional form of the Richards equation for variably saturated porous media. PARTRACE simulates solute transport based on a particle tracking code by solving the three-dimensional convection-dispersion-equation (CDE) using a particle tracking algorithm. The advantages of the TRACE/PARTRACE software package are time-dependent modeling, the combined treatment of saturated and unsaturated zones, the implementation of heterogeneous conductivity fields and the possibility of parallel computing (Englert, 2003).

4.2.2 Model Setup

Flow and transport simulations were carried out in an aquifer model which was derived from CPT data. The heterogeneous hydraulic conductivity field was generated by interpolating the CPT derived hydraulic conductivity parameters collected in the investigation area. Furthermore the natural boundary conditions at the test site like the seasonal variations of the groundwater table in the course of the tracer experiments were considered and implemented as boundary conditions for the numerical simulation of the flow field (cp. Figure 4-4).

Preliminary to the transport simulations in the heterogeneous flow field the tracer test was simulated in a homogeneous aquifer model to check whether the boundary conditions and the tracer injection were implemented correctly.

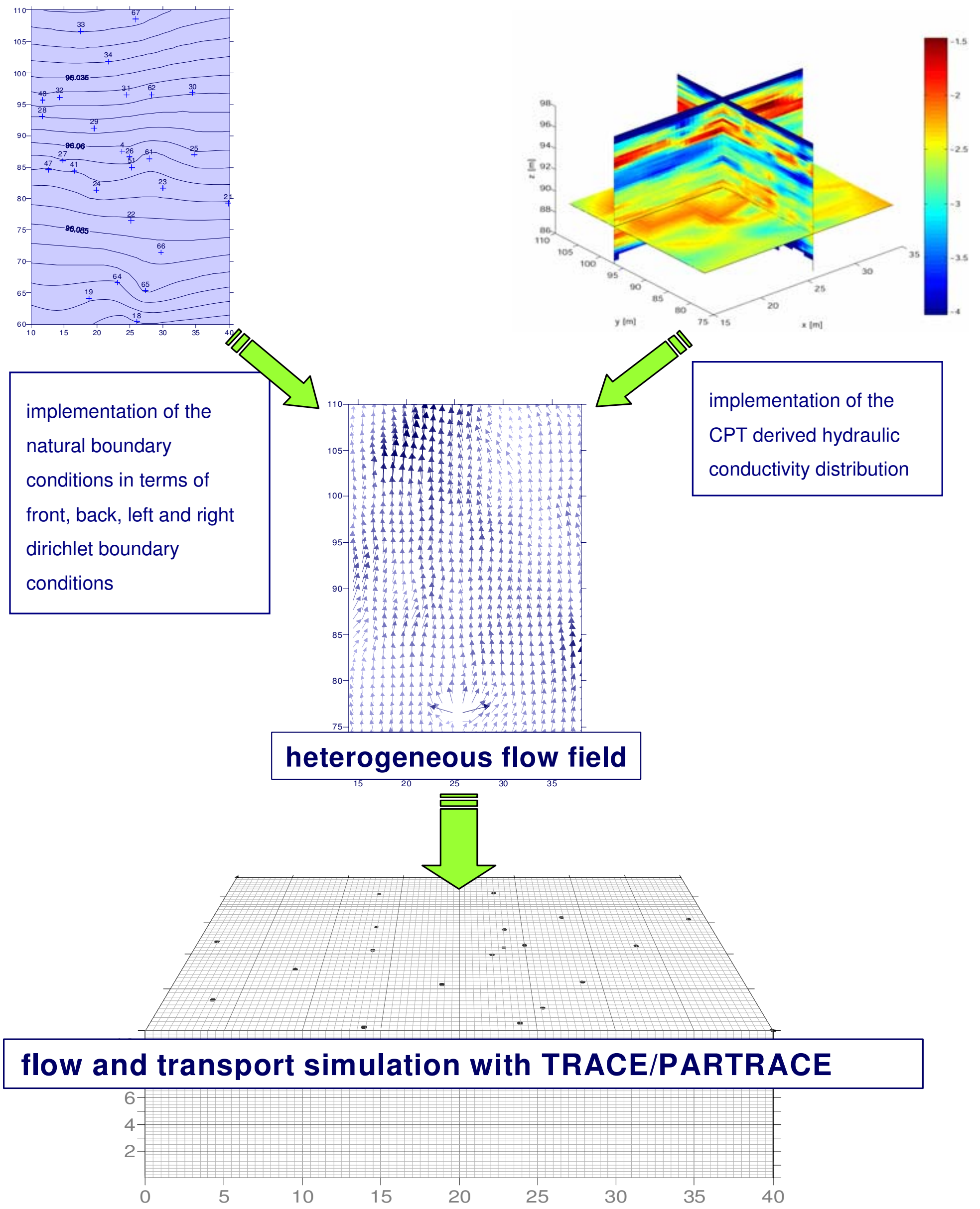

Figure 4-4: Flow chart illustration of the simulation procedure.

4.2.2.1 Model Discretization

A scheme of the discretized three-dimensional aquifer model is given in Figure 4-5. A discretization of 0.5 m was chosen for the x- and y-direction. The longitudinal or y-direction corresponds to the mean flow direction. The length of the simulated area was 40 m in longitudinal direction (80 elements) and 24 m in x-direction (48 elements). In the vertical z-direction, the model was discretized every 0.25 m down to a maximum aquifer depth of 11 m (44 elements). This discretization resulted in totally 168 960 elements and 178 605 nodes.

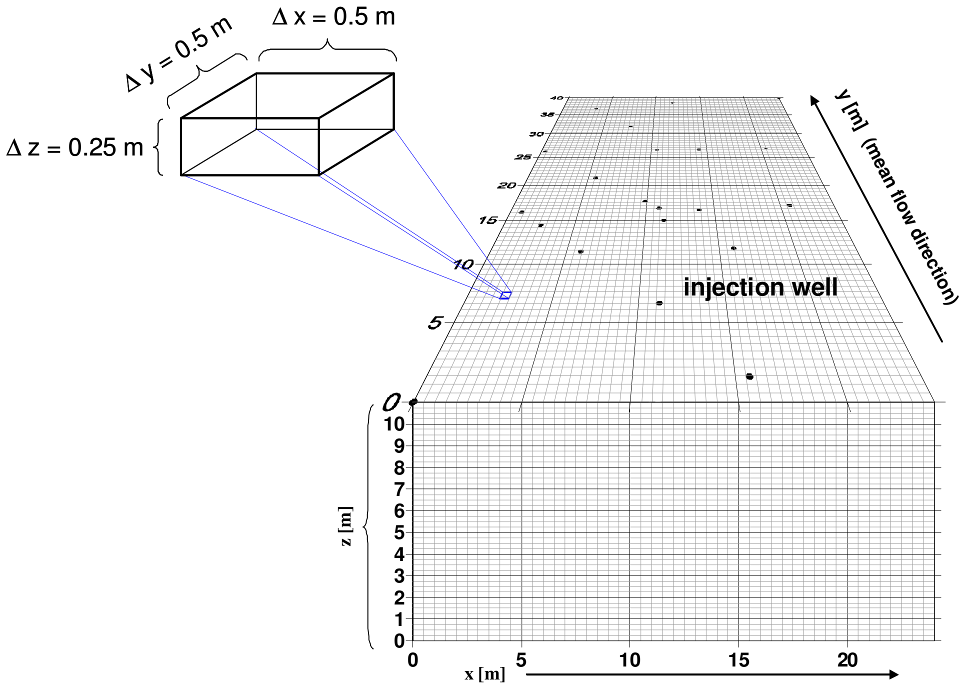

Figure 4-5: Discretized model for the tracer test simulation.

The simulated model is a cut-out of the central investigation area at the test site Krauthausen. In this region the cone penetration tests were conducted with high spatial resolution. The correlation between model and field site is given in Figure 4-6. The zero point for the x- and y-coordinates in the simulation domain corresponds with the field site coordinates x = 14 m, y = 70 m and z = 87 m NN.

The different coordinates for the injection well are given in Table 4-1.

Table 4-1: Different coordinates correlating the field coordinates with the model grid

B 22 (injection well)	x-coordinate	y-coordinate
field site [m]	25.18	76.52
model domain [m]	11	6.5
model [numbered nodes]	23	14

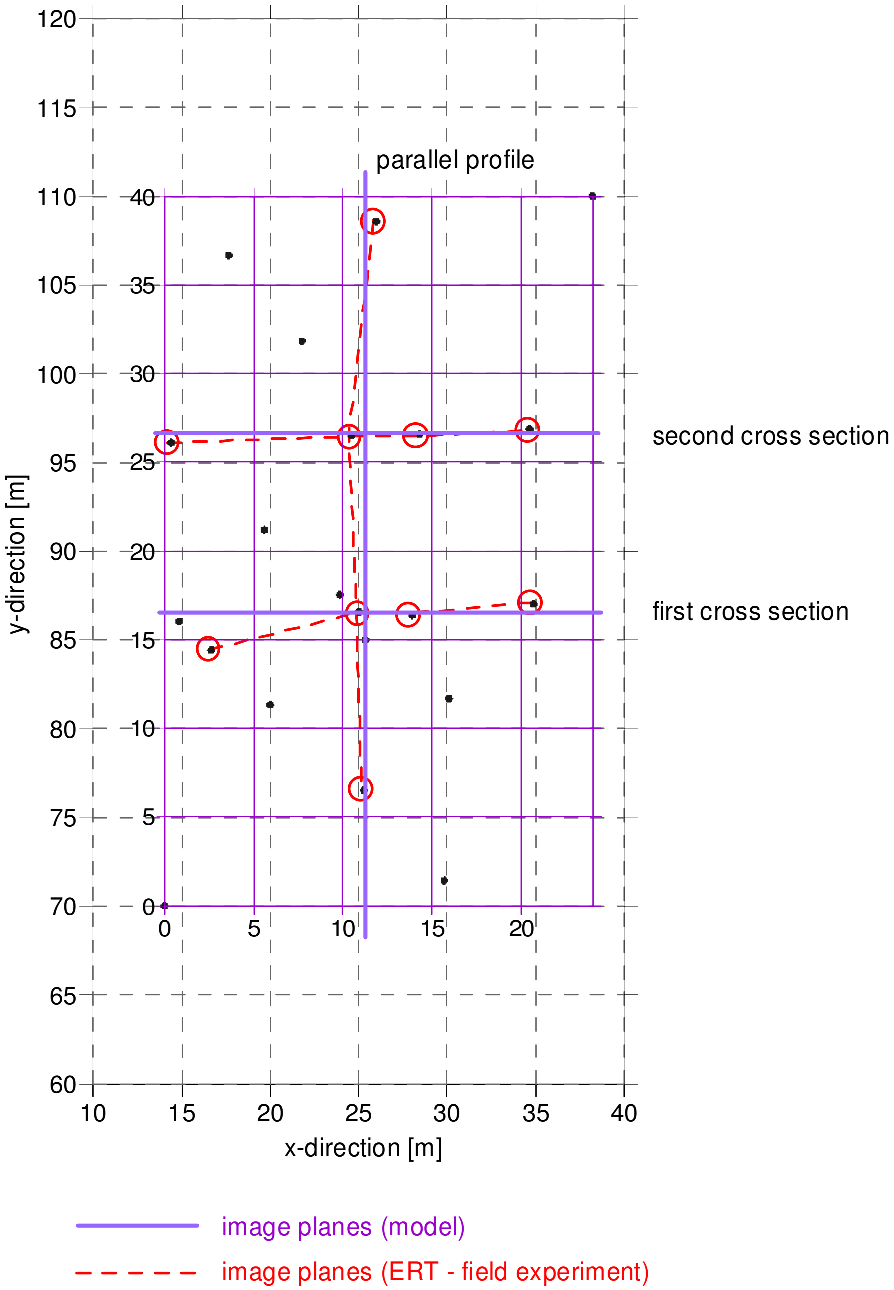

Figure 4-6: Coordinates of the test site Krauthausen and the model field. ERT image planes are marked with dashed red lines, the simulation image planes are marked with continuous violet lines.

4.2.2.2 Parameterization for the Flow and Transport Simulations

For the simulations in a first step a homogenous model was created. The parameters are listed in Table 4-2.

Table 4-2: Model parameter for the homogeneous flow simulation

Simulation Parameter	**Value**
mean hydraulic conductivity **K**	223 [m/d]
mean porosity n	0.27 [-]
simulation time t	85 [d]
longitudinal dispersivity λ_L	0.1 [m]
transversal dispersivity λ_T	0.01 [m]

The mean hydraulic conductivity **K** was derived from the arithmetic average of all CPT data. For the heterogeneous flow simulations the CPT derived hydraulic conductivity distribution was interpolated for every model element.

The flow field was simulated with saturated and unsaturated flow conditions. For the unsaturated flow conditions the van Genuchten parameters were specified (cp. Eq. 2-9) and these parameters were assumed to be constant in the simulation domain. For the heterogeneous model saturated hydraulic conductivities, which were specified at the grid nodes, were obtained from interpolation of the CPT data.

Table 4-3: Cut-out of the soil parameter data file

K	S	θ_s	θ_r	$\alpha 1$	n
9.548433	0	0.27	0.001	10	2.1
6.075563	0	0.27	0.001	10	2.1
3.907009	0	0.27	0.001	10	2.1
3.152841	0	0.27	0.001	10	2.1
5.498792	0	0.27	0.001	10	2.1
9.731039	0	0.27	0.001	10	2.1
14.631621	0	0.27	0.001	10	2.1
40.503331	0	0.27	0.001	10	2.1
112.719935	0	0.27	0.001	10	2.1
234.047869	0	0.27	0.001	10	2.1
135.020739	0	0.27	0.001	10	2.1
171.635236	0	0.27	0.001	10	2.1
208.468331	0	0.27	0.001	10	2.1
.	.	.	.	.	.
.	.	.	.		
.	.	.			
.					

In confined aquifers the effective saturation S ranges between 0.005 and 0.0005 m^{-1}. In our model case the effective saturation was set to zero. The saturated water content θ_s is equal to the porosity referred to Vereecken et al. (2000). The residual water content θ_r can be neglected and was therefore set to a minimum value of 0.001 to avoid numerical problems. The van Genuchten parameters α_1 and n are typical values for course textured soils (Herbst et al., 2005).

For the transport simulation molecular diffusion was neglected. The longitudinal and transversal dispersivities were higher than typical local dispersivities in sandy aquifers (e.g. $\lambda_L = 0.005$ m by Fiori and Dagan, 1999) but of the same order of magnitude derived from an analysis of local breakthrough curves observed in a gravel sediment (e.g. Vanderborght and Vereecken, 2002).

4.2.2.3 Boundary Conditions

During the field tests hydraulic head measurements were conducted once per week or every two weeks. The measurements were used to interpolate maps of the hydraulic head at the test site and document the variations in the groundwater table during the tracer tests. Since variations in the groundwater table influence the flow field within an aquifer the hydraulic head measurements were implemented in the simulations to reproduce the natural conditions at the test site as exactly as possible. As initial condition for the simulations the hydraulic heads at each grid node were derived from interpolation of heads measured in the groundwater observation wells. For the vertical direction, the heads were calculated assuming that no vertical flow occurred. In the course of the 85 days simulation time further Dirichlet boundary conditions were defined at the front, back, left and right model boundaries using interpolation of the head measurements. For the definition of the Dirichlet boundary conditions at the vertical surfaces, it was assumed that no vertical flow occurred in these surfaces. At the bottom and top of the model a zero flow or zero hydraulic head boundary condition was implemented. The mean hydraulic gradient in the y-direction was about -0.002.

4.2.2.4 Tracer Injection

To simulate the impact of the tracer injection on the flow field the tracer volume of 20 m^3 per day over a time-step of 7 days (140 m^3 in total) was injected nodal wise at the location of the injection well. The volume of the source term was distributed over 32 nodes in z-direction between 2.75 and 10.5 m below the model surface, which corresponds to the screening-length of the injection well at the field site. In the homogeneous model the total volume was distributed equally over the 32 source term nodes which led to a mean volume of 0.625 m^3 per node and day. For the heterogeneous simulations, the injected volume was distributed over the different injection nodes proportionally to the hydraulic conductivity of CPT derived hydraulic conductivities at the injection node. This resulted in higher volumes injected at nodes with higher hydraulic conductivity. Each nodal source term was defined as:

$$\text{nodal injection volume} = [(0.625 * \text{local } \mathbf{K}(x_i)) / \text{mean } \mathbf{K}(x)] \qquad \text{Eq. 4-3}$$

where the local **K**(x_i) is the hydraulic conductivity determined from CPT for a specific injection node and the mean **K**(x) is the hydraulic conductivity averaged over all 32 injection nodes.

In a second step the transport was simulated with PARTRACE based on the flow field and water content generated with TRACE, which solves the Richards equation. The total mass of injected tracer was defined in terms of the product of the electrical conductivity of the injected tracer solution and its volume. Since electrical conductivities and resistivities were measured with ERT and MLS, respectively, but not concentrations and since the electrical conductivity is linearly related to the tracer concentration, electrical conductivities were taken as a surrogate for solute concentrations.

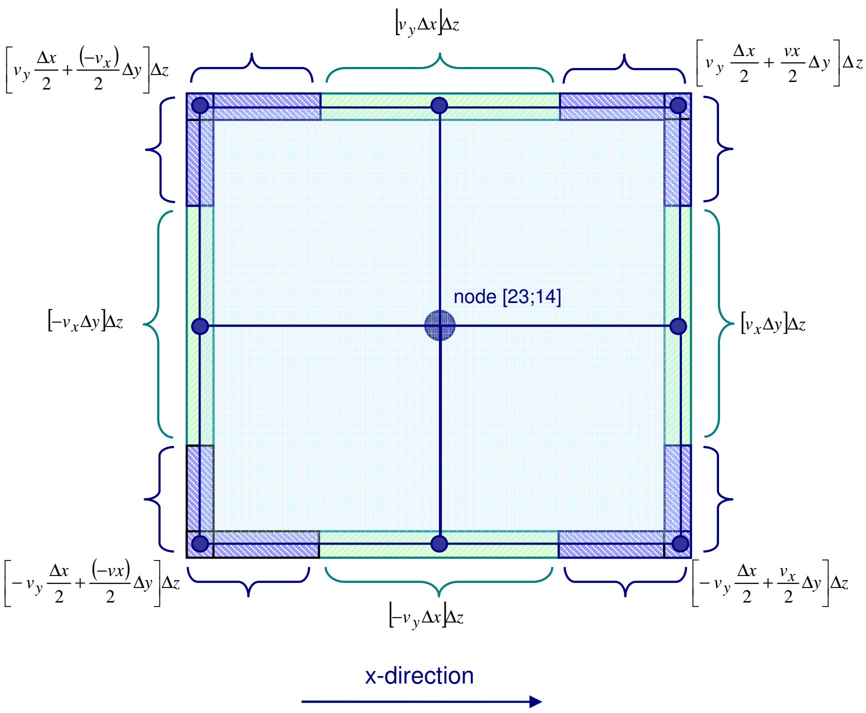

Figure 4-7: Scheme of the injection procedure for the transport simulations with PARTRACE (one horizontal plane). Green marked are the segments of the nodes with one dominating flow direction. For the edge-nodes the injected particles needed to be split into two segments concerning to the relative flow amount in x- and y-direction.

4.3 Results

4.3.1 Numerical Simulation Results

In the following the preliminary homogeneous simulations are shortly described. On the basis of the insights gained from the homogeneous model the heterogeneous simulations are discussed and interpreted concerning to equivalent transport parameters.

4.3.1.1 Homogeneous Model

Figure 4-8 shows horizontal and vertical concentration maps showing the tracer breakthrough derived from the homogeneous simulations. As explained before, the particles needed to be distributed over several injection segments to reproduce the injection at the field site. Using a discretization in x- and y-direction of 0.5 m it was not possible to simulate a totally homogeneously mixed input of the tracer mass with the particle tracking procedure. The concentration maps in a horizontal and in a vertical cross section perpendicular to the mean flow direction show bands with higher concentrations besides the central part of injection. However, the differences in concentrations are not so large and relatively unimportant for the transport simulations in heterogeneous flow fields.

Furthermore with regard to the horizontal plots a slight drift of the tracer plume to the right front boundary of the model can be observed from day 15 to 20. This is an effect of the implementation of the natural boundary conditions at the field site.

The homogeneous simulations showed that the model was appropriate to implement the heterogeneous hydraulic conductivity distribution.

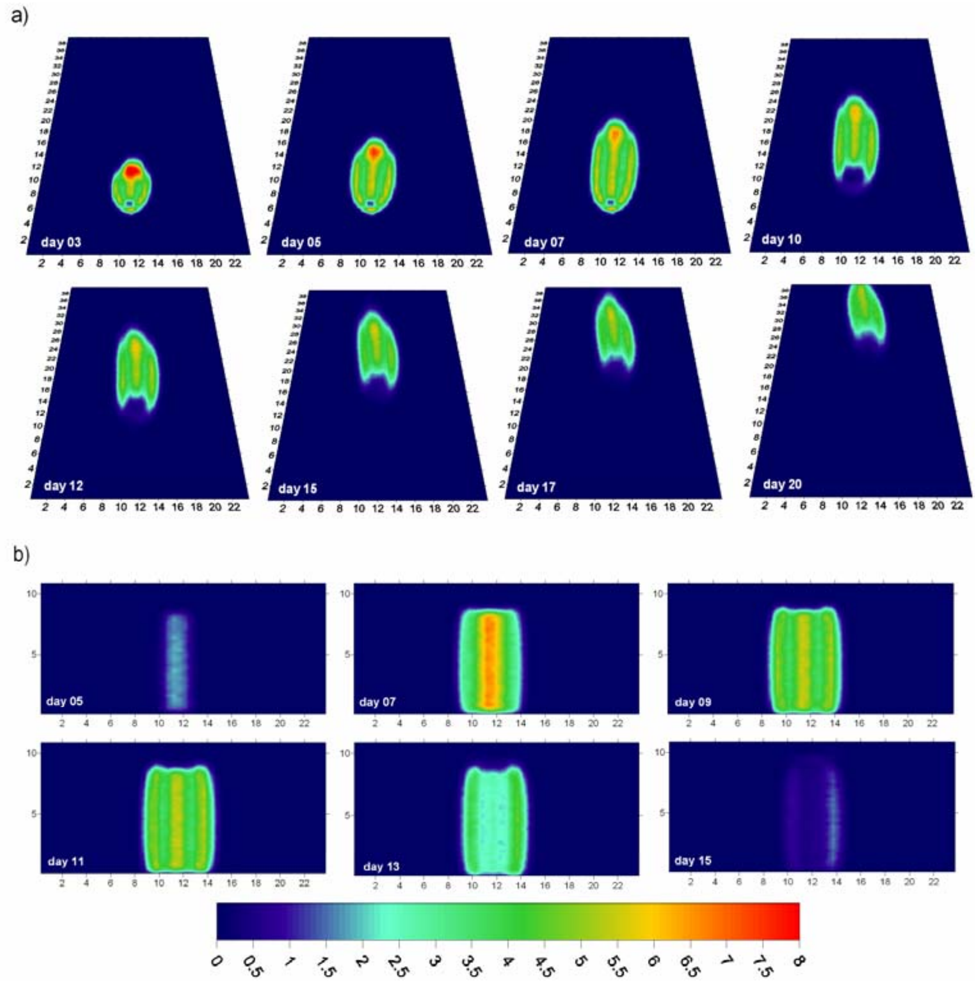

Figure 4-8: Tracer Breakthrough derived from the homogeneous simulation results. a) Horizontal plots (x-y-direction, node 15 in z-direction). b) Vertical plots (x-z-direction), 10 m distant to the injection location corresponding to the first cross section at the field site. The simulated concentrations are given in [mg/m³].

4.3.1.2 Heterogeneous Model

The heterogeneous simulations were done twice. Once with the boundary conditions in 2002 and another time with the boundary conditions in 2003. At the beginning of injection in September 2002 the groundwater table was about 2 m below the surface and increased during the tracer experiment up to 1 m below the surface at the end of November. In 2003 the groundwater level was about 2.4 m below the surface at the beginning of the tracer test and it decreased slightly about 0.1 m in the next 2 months of monitoring.

The simulations with different boundary conditions showed that the impact of the variations of the groundwater table in 2002 and 2003 had no impact on the tracer transport since the simulated tracer breakthrough was the same. The gradient remained constant. Thus the simulated flow field was not significantly affected by the variations in the groundwater table. The following results correspond to the simulation based on the 2002 boundary conditions.

Figure 4-9 shows the temporal evolution of the simulated tracer plume in the flow direction starting from the injection well. The fastest tracer breakthrough is observed in the upper aquifer region. For this region CPT derived very high hydraulic conductivities. The heterogeneity causes dispersion in longitudinal direction. The tracer plume is highly structured in zones with different flow velocities. In the middle and lowest part of the aquifer are two domains with very slow flow velocities. The concentrations simulated with PARTRACE are given in [mg/m³]. The initial concentration of the tracer was 7 mg/m³. It has to be considered that the simulated tracer mass was calculated from the electrical conductivity of the injected tracer solution and the volume of 140 m³ tracer solution, respectively which was injected over one week.

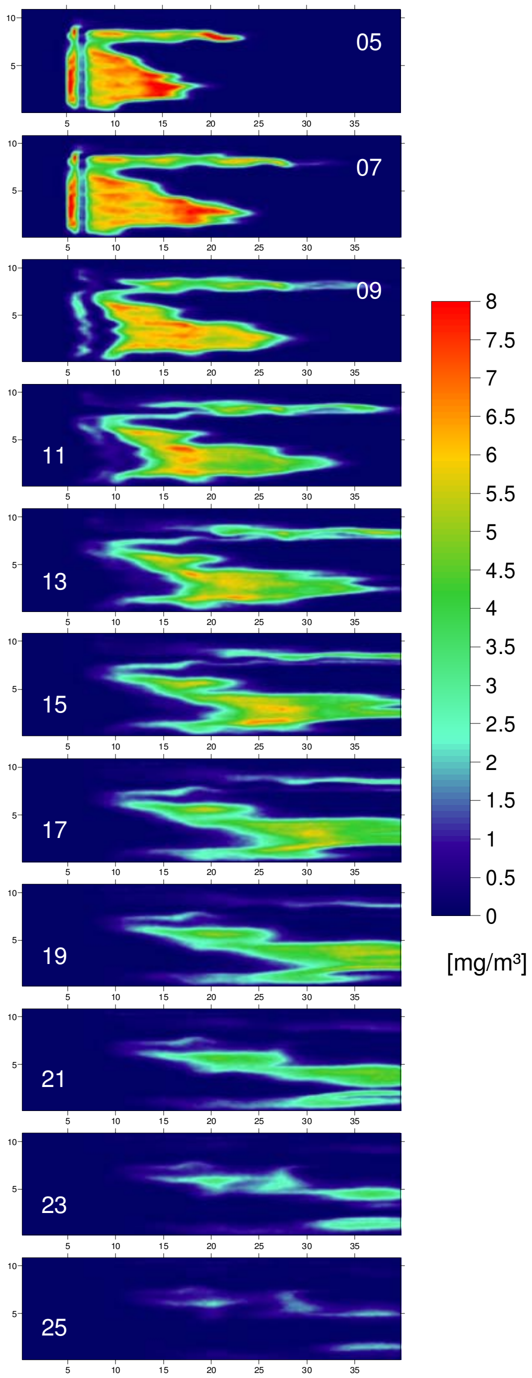

Figure 4-9: Temporal plots (days after beginning of injection) of the simulated tracer evolution in y-z-direction corresponding to the parallel profile at the field site.

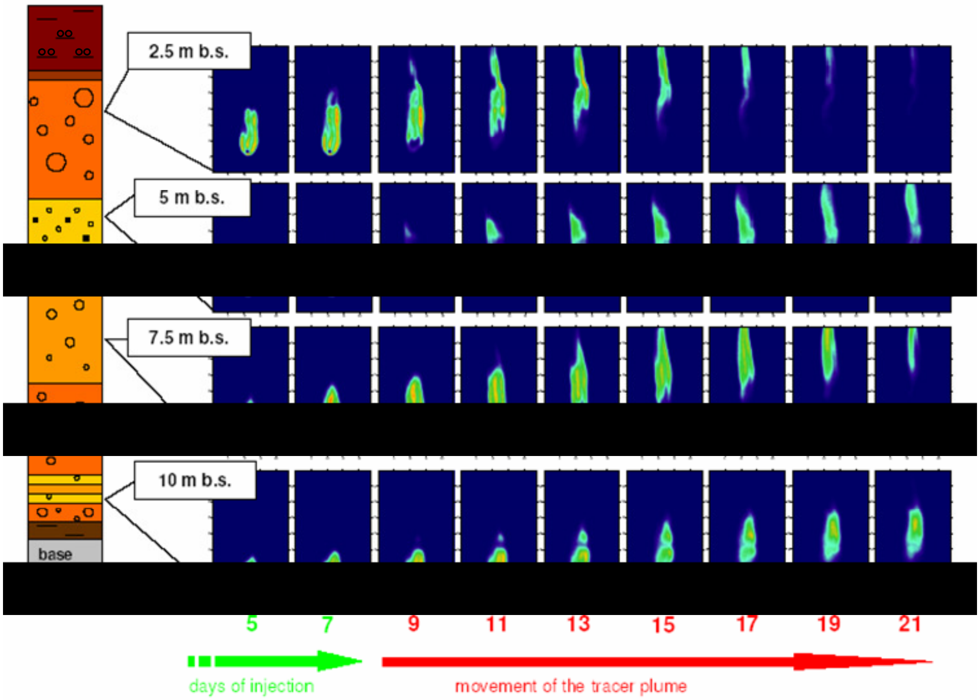

Figure 4-10: Horizontal plots of the simulated plume concentration at different depths in the aquifer showing the temporal evolution of the tracer plume.

Figure 4-10 shows horizontal plots of the temporal evolution of the tracer plume. The depths of the horizontal cut-outs in the modeled aquifer are given and the lithologic units they correspond to regarding the field site are illustrated by an idealized profile of the aquifer lithology. The horizontal plots at 2.5 m below the surface show strong longitudinal dispersion combined with high flow velocities. The tracer plume in this flow domain leaves the back end of the simulation domain completely after 21 days after beginning of injection. This layer corresponds to coarse textured sediments, mainly gravels. The simulation data at 5 m below the surface show a tracer plume that is highly disrupted and moving at a slower flow velocity. The disruption of the tracer plume indicates locally impermeable lenses in this part of the simulated aquifer. This layer is composed of fine grained sediments with dominating sand fraction. The layer 7.5 m below the surface shows a more homogeneous extension of the tracer plume. The movement of the tracer plume in the first days after injection is similar to the homogeneous simulation results. At the field site this layer corresponds to mainly fine gravels. The lowest flow velocities accompanied with minor longitudinal dispersion are simulated in the lowest part, 10 m below the surface of the aquifer. This layer is composed of an inter-bedded strata of sandy and gravely sediments with some clay content. 21 days after the beginning of injection the tracer mass in this part has even reached the central area of the modeled simulation domain.

4.3.1.3 Derivation of Equivalent Transport Parameters

Similarly to the characterization of the heterogeneity observed with ERT and MLS in the field tracer tests effective stream tube model parameters were used to interpret the heterogeneity of the simulated tracer breakthrough. The heterogeneity was investigated at a cross sectional plane corresponding to the first cross section at the field site. The stream tube parameters were estimated in two different ways. In a first procedure, they were estimated using a least square fit of the 1D convection dispersion equation (cp. Eq. 2-16) to the simulated BTCs. In the second procedure, they were estimated from the temporal moments of the local BTCs (cp. Eqs. 2-24 and 2-25). The results of the STM approach and the temporal moment analysis are illustrated in Figure 4-11.

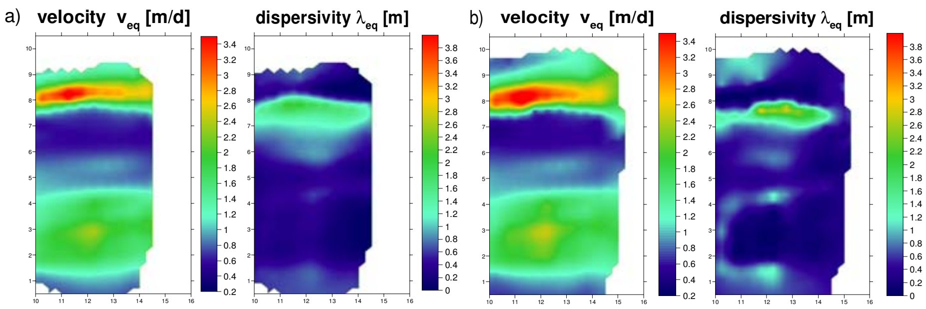

Figure 4-11: Stream tube model parameters derived from a) temporal moment analysis and b) least squares fit of the 1D convection dispersion equation (first cross section).

The derived velocities and dispersivities show a good correlation for both approaches. The highest velocities with more than 3 m per day were observed at 2.5 m below the model surface. Another domain with higher velocities of 1.5 to 2 m per day was observed between 6 and 8.5 m below the surface.

The quantitative values calculated for the numerical simulations are summarized in Table 4-4.

Table 4-4: Results of the characterization of the heterogeneity by means of a stream tube model: comparison between CDE-fit and temporal moment analysis for the first cross section.

	$<v_{eq}>$		$\sigma^2 v_{eq}$		$<\lambda_{adv}>$		$<\lambda_{eq}>$	
	CDE-fit	**moments**	**CDE-fit**	**moments**	**CDE-fit**	**moments**	**CDE-fit**	**moments**
simulation	1.42	1.34	0.50	0.40	1.02	0.86	0.44	0.54

The velocities derived from least square fit are higher than the velocities calculated with temporal moment analysis. The effective velocity was determined with 1.42 and 1.34 m per day. As a reason of the very high velocities in the upper aquifer region compared to the overall velocities the variance of the effective velocity is relatively high for both approaches. The dispersivities derived from the least square fit of the equivalent 1D convection dispersion equation are lower than those derived from temporal moment analysis. Vanderborght and Vereecken (2001) showed that equivalent dispersivities of local BTCs derived from least square fit of the 1D CDE were considerable smaller than those derived from the time moments since local BTCs exhibit extended tailing.

4.3.2 Comparison of Simulation and Field Test

The numerical simulations were done neglecting density effects. The 'positive' tracer test, which was conducted injecting the calcium chloride solution, showed a density driven sinking resulting from the higher density of the salt solution compared to the groundwater. Therefore the tracer test in 2003 with the 'negative' tracer seemed to be more appropriate for the comparison between tracer test and simulation.

In Figure 4-12 the tracer breakthroughs at the first cross section for the 'positive' and 'negative' tracer tests are compared with the simulation results. The simulation data show a fast and distinct tracer breakthrough in the upper part of the simulated aquifer three days after the start of injection, which was not observed in the field tests. Concerning to the field tests, there was no distinct breakthrough until five and seven days after the start of injection, for the 'positive' and 'negative' tracer tests, respectively. But, this early breakthrough occurred in the lower part of the aquifer. The main tracer breakthrough of the field tests was observed in the middle and lower parts of the aquifer. The simulation shows a distinction of the tracer plume in two main parts after 5 days due to heterogeneity. From ten days on the visible separation in different plume sections proceeds and the plume is split into three parts after 15 days. A similar vertical zoning of the tracer plume was detected in the field tests. The best correlation between field tests and simulation is given from 15 days after the beginning of injection to day 20. After 24 days the simulated tracer breakthrough at the first cross section is almost completed. The tracer plumes monitored with ERT at the field site were observed for more than 35 days during the 'negative' tracer test and about 45 days during the 'positive' tracer test.

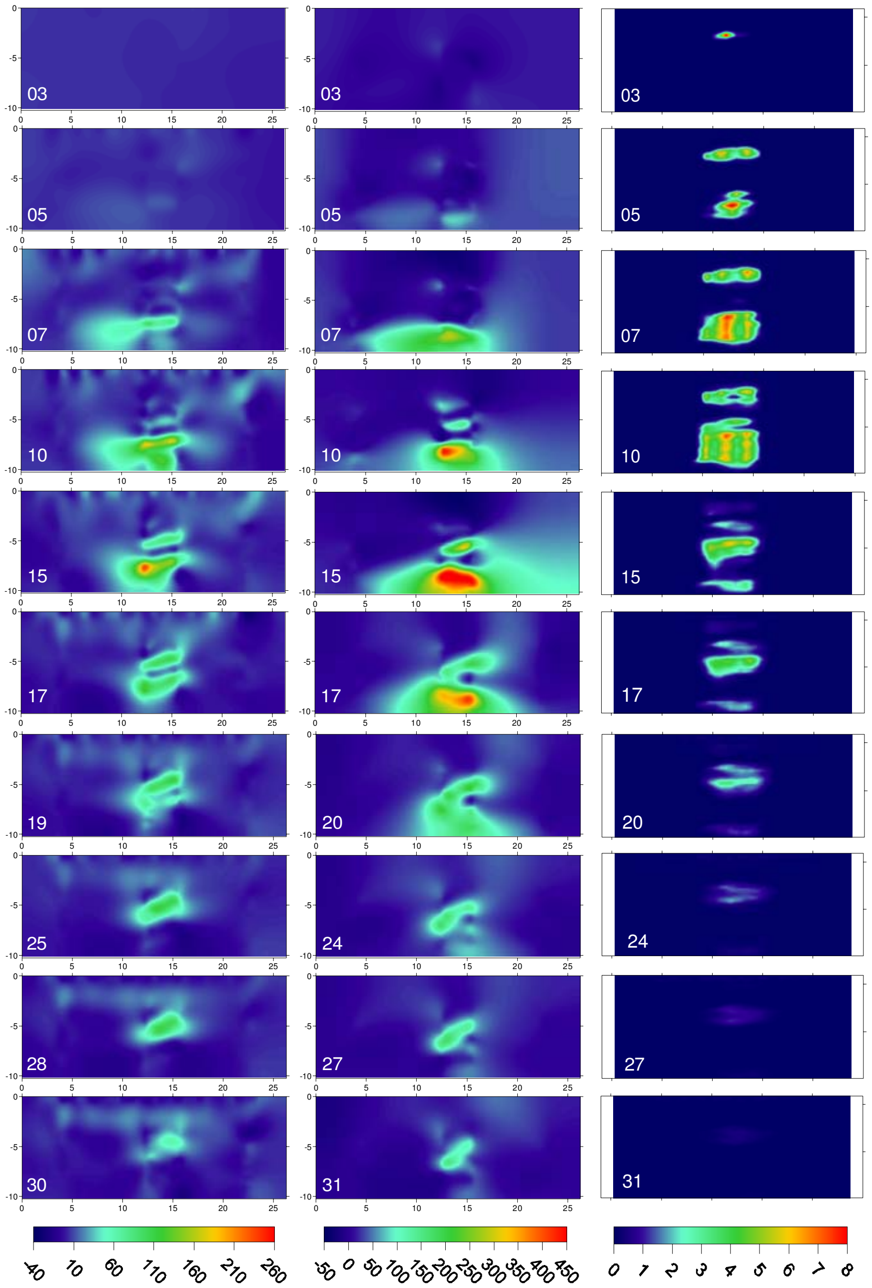

Figure 4-12: Comparison between 'negative' tracer test (left side), 'positive' tracer test (middle) and numerical simulation (right side). The tracer tests are illustrated in [%] relative change in conductivity and resistivity, respectively. The simulated concentrations are given in [mg/m³].

Comparison of Equivalent Transport Parameters

In Figure 4-13 the equivalent parameters derived with temporal moment analysis for the simulations are compared with the equivalent parameters derived from the STM approach for the 'positive' and 'negative' tracer tests (first cross section).

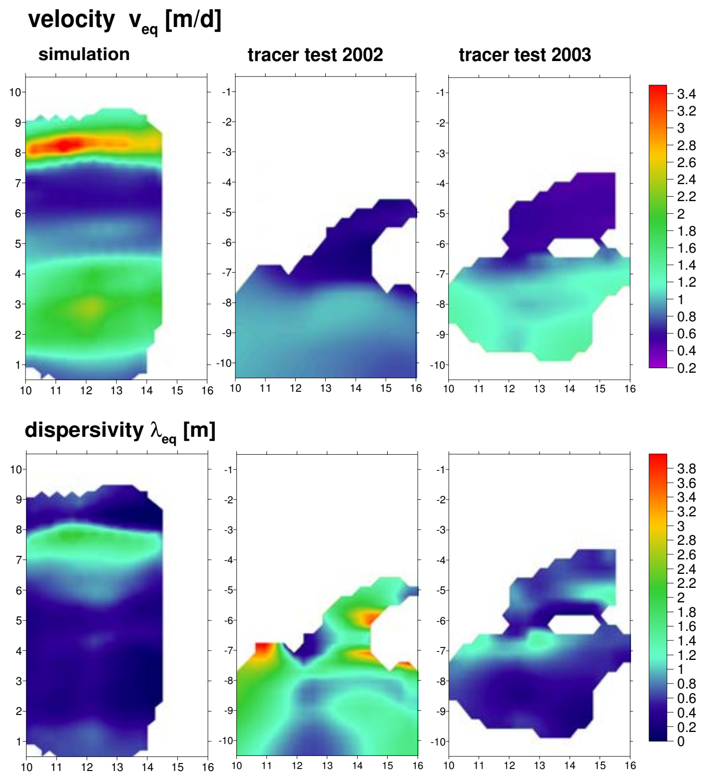

Figure 4-13: Equivalent transport parameters for the simulations and the tracer tests. The plots correspond to the first cross section at field site and model.

For the equivalent velocity, the plots show a good correlation between the tests and the simulations velocity in the middle and lower part of the aquifer. In the simulations, the highest velocities were derived in the upper aquifer region. This more conductive zone was not flown through by tracer solution in the field tests because of the screening of the injection well. The injection well at the field site, borehole 22, is screened between 3 and 11 m below the surface.

With regard to the dispersivity the simulations show less accordance with the tests. The simulations derived very low dispersivities except for the upper region which corresponds to the layer with the highest velocities. The best fit with the simulations shows the 'negative' tracer test. The dispersivities derived for the 'positive' tracer test are generally higher.

4.4 Conclusions and Discussion

In the second part of the thesis the tracer tests were simulated and compared with the tracer tests at the Krauthausen test site. The three-dimensional numerical flow and transport simulations were done using the TRACE and PARTRACE numerical models. To reproduce a realistic model of the aquifers heterogeneity Cone Penetration Tests (CPT) conducted at the test site were used to estimate a three-dimensional hydraulic conductivity distribution which was implemented in the numerical model. The hydraulic conductivity distribution was derived from CPT using a regression analysis between grain size distribution parameters and the hydraulic conductivity (Tillmann et al., 2005). The numerical simulations suggested the presence of a highly conductive layer in the upper part of the aquifer, in which the simulated tracer velocity is high. In the tracer tests, this was not observed because no tracer was recovered in this layer. Since no tracer mass was found in this layer in the 'negative' experiment either, density driven flow cannot be used as an explanation why there was no tracer found in this upper aquifer region. Therefore, the tracer tests suggest that this layer is not that conductive as derived from the regression analysis. Therefore, the validity of the regression equation for the upper part of the aquifer, in which a considerable amount of clay is present, should be questioned. More recent permeameter tests in columns packed with aquifer sediment from this layer indicated that the hydraulic conductivity of this layer is indeed lower. For the middle and deeper part of the aquifer, the observed tracer breakthrough pattern was fairly well reproduced in the numerical simulations which demonstrates that the aquifer model for this part was quite accurate.

To quantify the heterogeneity, the simulations were analyzed by means of a one-dimensional stream tube model approach. The equivalent velocities determined from the simulations were higher than the field test equivalent velocities. This can be explained by the upper aquifer region with high hydraulic conductivities which was not captured during the tracer tests at the field site. Besides this upper aquifer flow domain, simulation and ERT showed a good agreement concerning the magnitude and overall distribution of the flow velocities. The dispersivities derived from the simulations showed a good agreement with the dispersivities derived from the 'negative' tracer test for the upper and lower aquifer region. The 'positive' tracer test dispersivities were about factor 2 or even more higher compared to the simulations. The better fit between the 'negative' tracer test and the simulations compared to the 'positive' tracer test and the simulations points out that the model is more appropriate for tracers with negligible density effects. With the transport model TRACE/PARTRACE it is not possible to simulate density driven flow.

Furthermore, the simulations showed that CPT is an appropriate fast and comparably cost-extensive method to characterize the aquifer heterogeneity at the test site Krauthausen.

5 Outlook

Further work should be done on the simulations with regard to the upper part of the aquifer. Because of the fact that this upper part of the flow domain was not captured with the field tests, it should be neglected in the simulations as well. In addition, the very high hydraulic conductivities derived with CPT in the upper aquifer region should be compared in more detail to analyses of grain size distribution. This could lead to an optimization of the calibration between CPT and grain size which is used for the multiple linear regression analysis.

Concerning the validation of the simulations it would be useful to run a representative amount of simulations based on different conductivity distributions. For the CPT derived conductivity distribution at the test site a standard deviation of 0.303 was determined. The impact of this variation in the conductivity distribution should be analyzed to validate the deterministic aquifer model.

For the ERT inversions better inversion algorithms are required. To improve these inversion algorithms, information about the hydro-geologic process should be included in the ERT data set inversion. For instance, the mass balance can be included in the regularization term. Another point to improve the ERT inversion is to condition the inversion on measured electrical conductivities in the image plane. However, the results from the multilevel sampling illustrated that these data may be prone to errors as well and do not have the same volume of support as the ERT pixels so that one should be careful when including such kind of data for conditioning.

Bibliography

Archie, G. E. (1942). The electrical resistivity log as an aid in determining some reservoir characteristics. *Trans. Am. Inst. Miner. Metall.* **146**: 54-62.

Barber, C. B., D. P. Dobkin and H. T. Huhdanpaa (1996). The Quickhull Algorithm for Convex Hulls. *ACM Transactions on Mathematical Software*. **22**(4): 469-483.

Bear, J. (1972). *Dynamics of Fluid in Porous Media*, Elsevier New York.

Bialas, Z. and A. S. Kleczkowski (1970). Über den praktischen Gebrauch von einigen empirischen Formeln zur Berechnung des Durchlässigkeitskoeffizienten K. *Archivum Hydrotechniki*. Warschau.

Cvetkovic, V. D. and A. M. Shapiro (1989). Solute advection in stratified formations. *Water Resour. Res.* **25**: 1283-1289.

Dagan, G. (1984). Solute transport in heterogeneous porous formations. *J. Fluid Mech.* **145**: 151-177.

Dagan, G., V. Cvetkovic and A. Shapiro (1992). A solute flux approach to transport in heterogeneous formations: 1. The general framework. *Water Resour. Res.* **28**: 1369-1376.

Dagan, G. and V. Nguyen (1989). A comparison of travel time and concentration approaches to modeling transport by groundwater. *J. Contam. Hydrol.* **4**: 79-91.

Daily, M. and E. Owen (1991). Cross borehole resistivity tomography. *Geophysics* **56**: 1228-1235.

Daily, M., A. L. Ramirez, D. J. LaBrecque and J. Nitao (1992). Electrical resistivity tomography of vadoze water movement. *Water Resour. Res.* **28**: 1429-1442.

Delleur, J. W. (1999). *The Handbook of Groundwater Engeneering*. Boca Raton and Heidelberg, CRC Press and Springer Verlag.

Dey, A. and H. F. Morrison (1979). Resistivity modeling for arbitrarily shaped two-dimensional structures. Geophys. Prospect. **27**: 106-136.

Döring, U. (1997). Transport der reaktiven Stoffe Eosin, Uranin und Lithium in einem heterogenen Grundwasserleiter. Ph.D. thesis, Christian Albrechts Universität, Kiel.

Englert, A. (2003). Measurement, Estimation and Modeling of Groundwater Flow Velocity at Krauthausen Test Site. Ph.D. thesis, AGROSPHERE Institute, FORSCHUNGSZENTRUM JÜLICH GmbH, RWTH Aachen.

Fiori, A. and G. Dagan (1999). Concentration fluctuations in transport by groundwater: Comparison between theory and field experiments. *Water Resour. Res.* **35**: 139-163.

Franson, M. A. H. (1985). Standard Methods for the Examination of Water and Wastewater. *16th ed. Am. Public Health Assoc.*, Washington, DC.

Gelhar, L. W. (1993). *Stochastic Subsurface Hydrology*. Prenstice Hall, Upper Saddle River, N. J.

Gössling, K. (2004). Geoelektrische Tomographie zur Überwachung eines Tracerversuchs auf dem Testfeld Krauthausen. Master thesis. Institut für Geophysik und Meteorologie, Universität zu Köln.

Herbst, M., H. Hardelauf, R. Harms, J. Vanderborght and H. Vereecken (2005). Pesticide fate at regional scale: Development of an integrated model approach. *Physics and Chemistry of the Earth* **30**: 542-549.

Jury, W. A. and G. Sposito (1985). Field calibration and validation of solute transport models for the unsaturated zone. *Soil Sci. Soc. Am. J.* **49**: 1331-1341.

Jury, W. A. and K. Roth (1990). Transfer functions and solute movement through soil: theory and application. Basel, Boston, Berlin, Birkhäuser Verlag.

Kemna, A., J. Vanderborght, B. Kulessa and H. Vereecken (2002). Imaging and characterisation of subsurface solute transport using electrical resistivity tomography (ERT) and equivalent transport models. *J. Hydrol.* **267**(3-4): 125-146.

LaBrecque, D. J., M. Miletto, W. D. Daily, A. L. Ramirez and E. Owen (1996). The effects of noise on Occam's inversion of resistivity tomography data. *Geophysics* **61**: 538-548.

LaBrecque, D. J. and X. Yang (2001). Difference inversion of ERT data: A fast inversion method for 3D in situ monitoring. *J. Environ. Eng. Geophys.* **5**: 83-90.

Leij, F. J. and J. H. Dane (1991). Solute transport in a two-layer medium investigated with time moments. *Soil Sci. Soc. Am. J.* **55**: 1529-1535.

Mualem, Y. (1977). Extension of the similarity hypothesis used for modeling the soil water characteristic. *Wat. Resour. Res.* **29**(2): 773-780.

Müller, K., J. Vanderborght, A. Englert, A. Kemna and H. Vereecken (2005). Characterization of transport processes in a heterogeneous aquifer using electrical resistivity tomography (ERT). *Proceedings of GQ2004, the 4th International Groundwater Conference, held at Waterloo, Canada, July 2004, IAHS Publ.* **297**: 182-190.

Neuendorf, O. (1996). Numerische 3-D Simulation des Stofftransportes in einem heterogenen Aquifer. ph.D. thesis, RWTH Aachen.

Neumann, S. P., L. C. Winter and C. M. Newman (1987). Stochastic theory of field-scale Fickian dispersion in anisotropic porous media. *Water Resour. Res.* **23**: 453-466.

Ramirez, A. L., M. Daily, D. J. LaBrecque, E. Owen and D. Chesnut (1993). Monitoring an underground steam injection process using electrical resistance tomography. *Water Resour. Res.* **29**: 73-87.

Reynolds, J. M. (1997). *An Introduction to Applied and Environmental Geophysics*. John Wiley & Sons: Chichester.

Rhoades, J. D., N. A. Manteghi, P. J. Shouse and W. J. Alves (1989). Soil electrical conductivity and soil salinity: new formulations and calibrations. *J. Am. Soil Sci. Soc.* **53**: 433-439.

Seidemann, R. (1996). Parallelisierung eines Finite Elemente Programms zur Modellierung des Transports von Stoffen durch heterogene poröse Medien. ph.D. thesis, Rheinische Friedrich-Wilhelms Universität Bonn.

Sen, P. N., P. A. Goode and A. Sibbit (1988). Electrical conduction in clay bearing sandstones at low and high salinities. *J. Appl. Phys.* **63**: 4832-4840.

Shapiro, A. M. and V. D. Cvetkovic (1988). Stochastic analysis of solute arrival time in heterogeneous porous media. *Water Res. Res.* **24**: 1711-1718.

Simmons, C. S. (1982). A stochastic-convective transport representation of dispersion in one-dimensional porous media systems. *Water Res. Res.* **18**: 1193-1214.

Singha, K., A. M. Binley, J. W. Lane Jr. and S. M. Gorelick (2003). Electrical imaging of tracer migration at the Massachusetts Military Reservation, Cape Cod. In *Symposium on the Application of Geophysics to Engeneering and Environmental Problems (SAGEEP). April 6-10, 2003. San Antonio, Texas.* Proceedings [CD ROM]: 464-474. Environ. and Eng. Geophys. Soc., Denver, Colo.

Tillmann, A., Z. Nyari, I. Fejes, A. Englert, J. Vanderborght, J. Stickel, J. Bagi and I. Balazs (2005). Cone Penetration Tests (CPT) on the Krauthausen Test Site - Part I: Data Aquisition and Preliminary Interpretation of the Surveys 2003 and 2004. Online Publication of the Forschunszentrum Jülich GmbH.

Tillmann, A., Z. Nyari, I. Fejes, J. Vanderborght and H. Vereecken (2004). Cone Penetration Tests for investigation of heterogeneity in an aquifer at Krauthausen. In *Proceedings of EAGE 66th Conference & Exhibition*, Paris.

Vanderborght, J. and H. Vereecken (2001). Analyses of locally measured bromide breakthrough curves from a natural gradient tracer experiment at Krauthausen. *J. Contam. Hydrol.* **54**: 141-171.

Vanderborght, J. and H. Vereecken (2002). Estimation of local scale dispersion from local breakthrough curves during a tracer test in a heterogeneous aquifer: The Lagrangian Approach. *J. Contam. Hydrol.* **54**: 141-171.

Vanderborght, J., A. Kemna, H. Hardelauf and H. Vereecken (2005). Potential of electrical resistivity tomography to infer aquifer transport characteristics from tracer studies: A synthetic case study. *Water Resour. Res.* **41:** W06013.

Van Genuchten, M. T. (1980). A closed-form equation for predicting the hydraulic conductivity of unsaturated soils. *Soil. Sci. Soc. Am. J.* **19**(1): 161-180.

Vereecken, H., U. Döring, H. Hardelauf, U. Jaekel, U. Hashagen, O. Neuendorf, H. Schwarze, and R. Seidemann (2000). Analysis of solute transport in a heterogeneous aquifer: the Krauthausen field experiment. *J. Contam. Hydrol.* **45**(3-4): 329-358.

Appendix

Tracer Injection: Electrical Conductivity Distribution During the First Days of Monitoring

'negative' tracer test

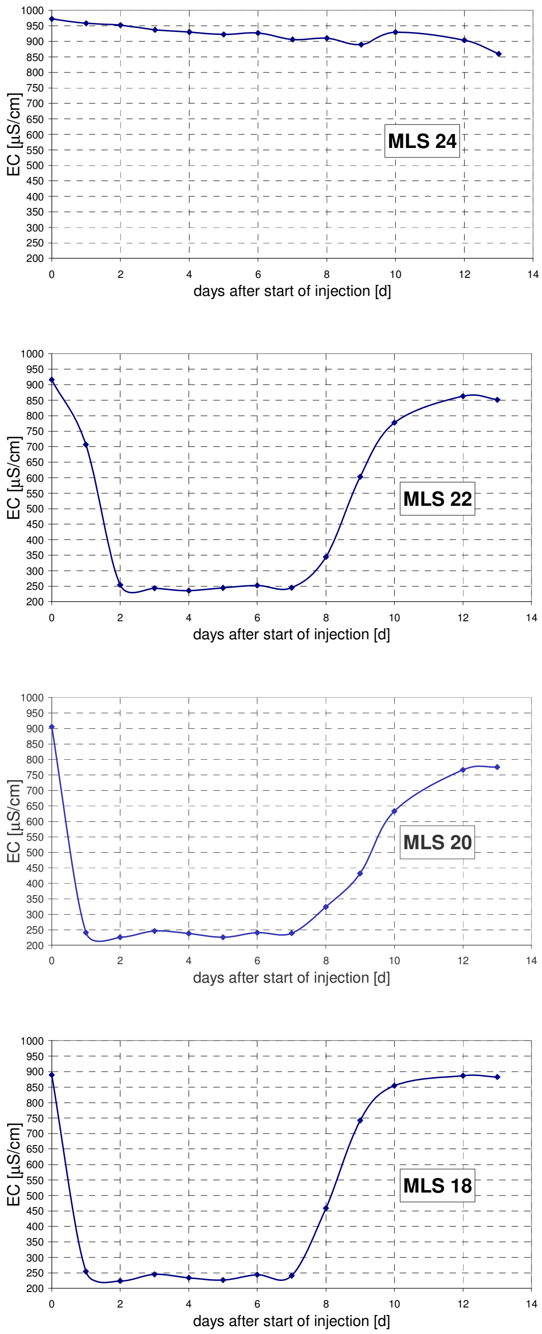

Borehole 22: BTC in electrical conductivity in the MLS during the first days after start of injection

'negative' tracer test

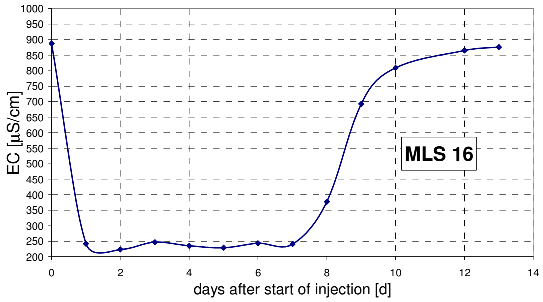

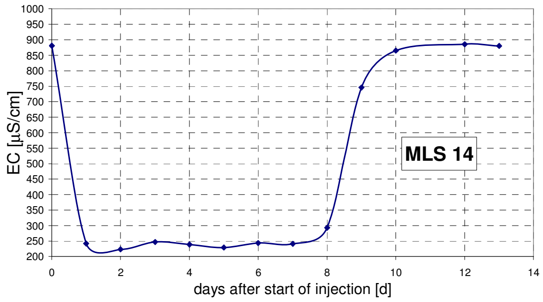

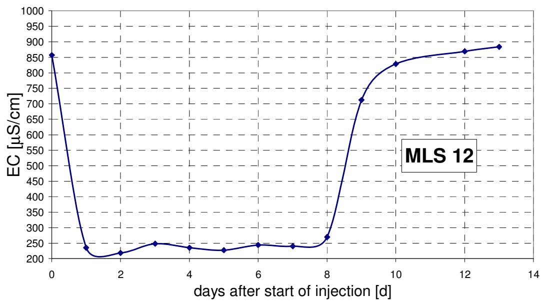

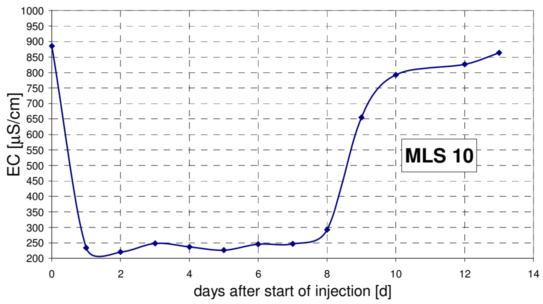

Borehole 22: BTC in electrical conductivity in the MLS during the first days after start of injection

'negative' tracer test

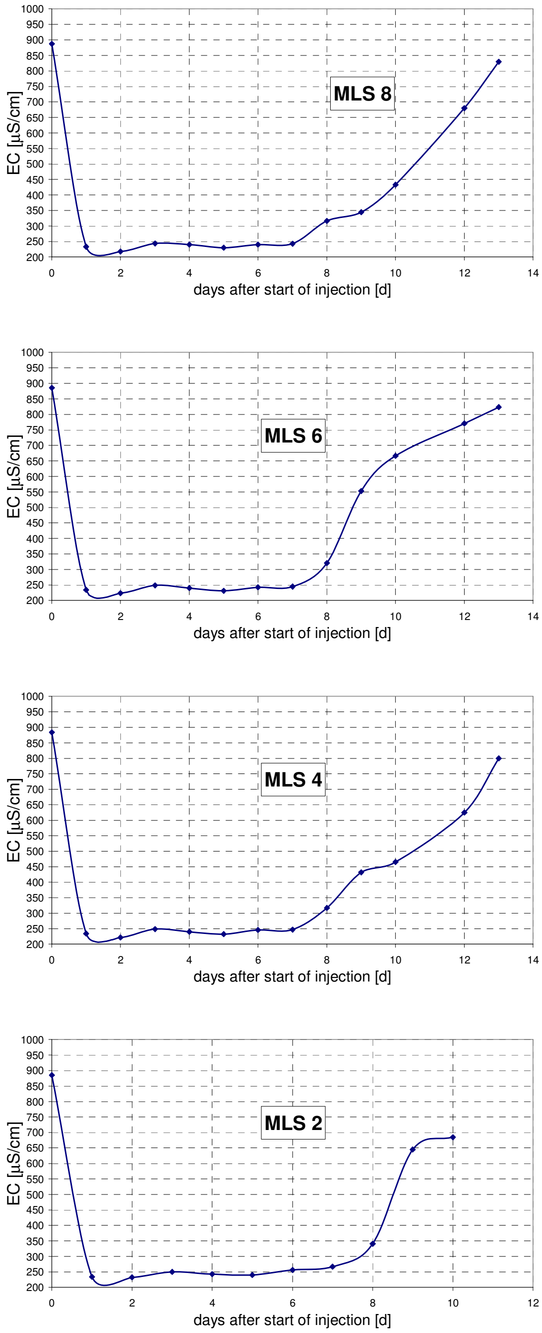

Borehole 22: BTC in electrical conductivity in the MLS during the first days after start of injection

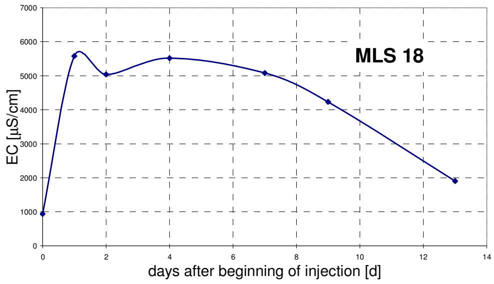

'positive' tracer test

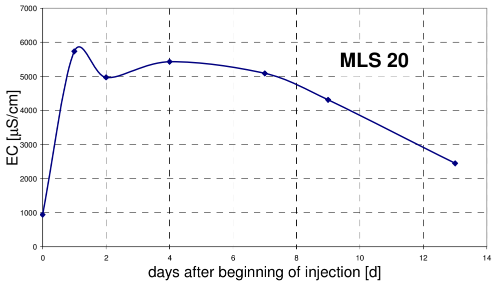

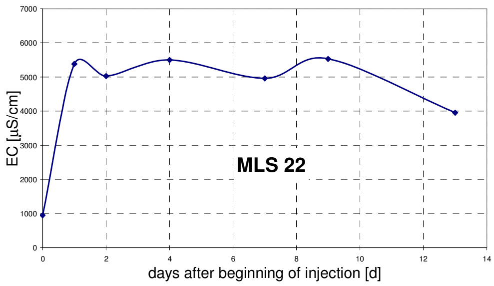

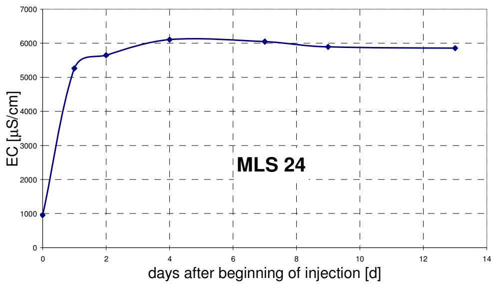

Borehole 22: BTCs from the MLS during the first days after start of injection

'positive' tracer test

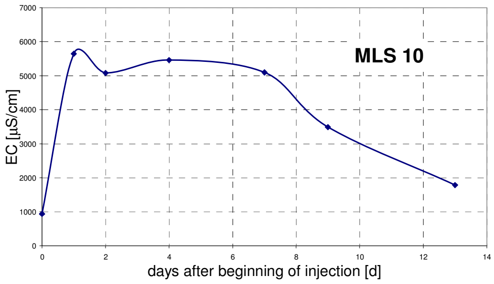

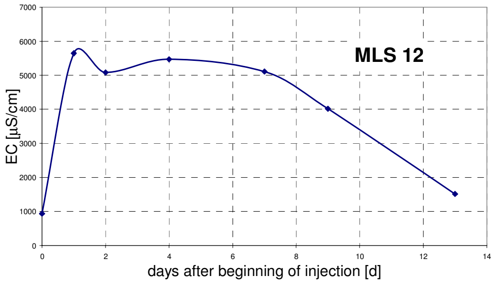

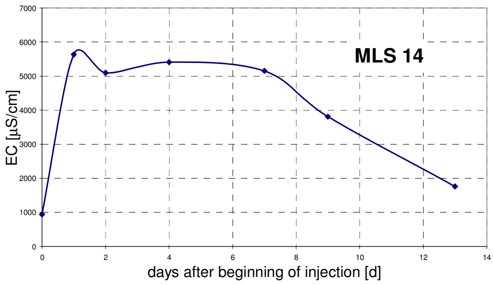

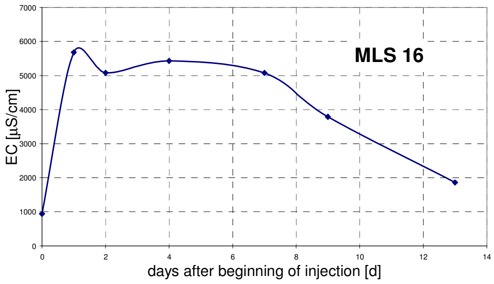

Borehole 22: BTCs from the MLS during the first days after start of injection

'positive' tracer test

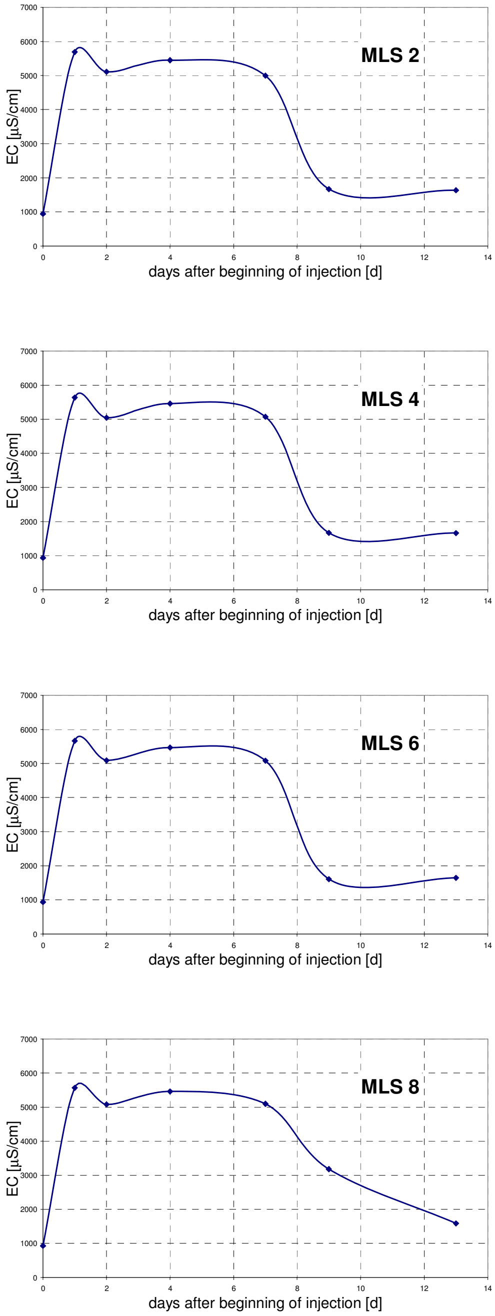

Borehole 22: BTCs from the MLS during the first days after start of injection

Mean GW-Table Used for the Simulations as Boundary Conditions

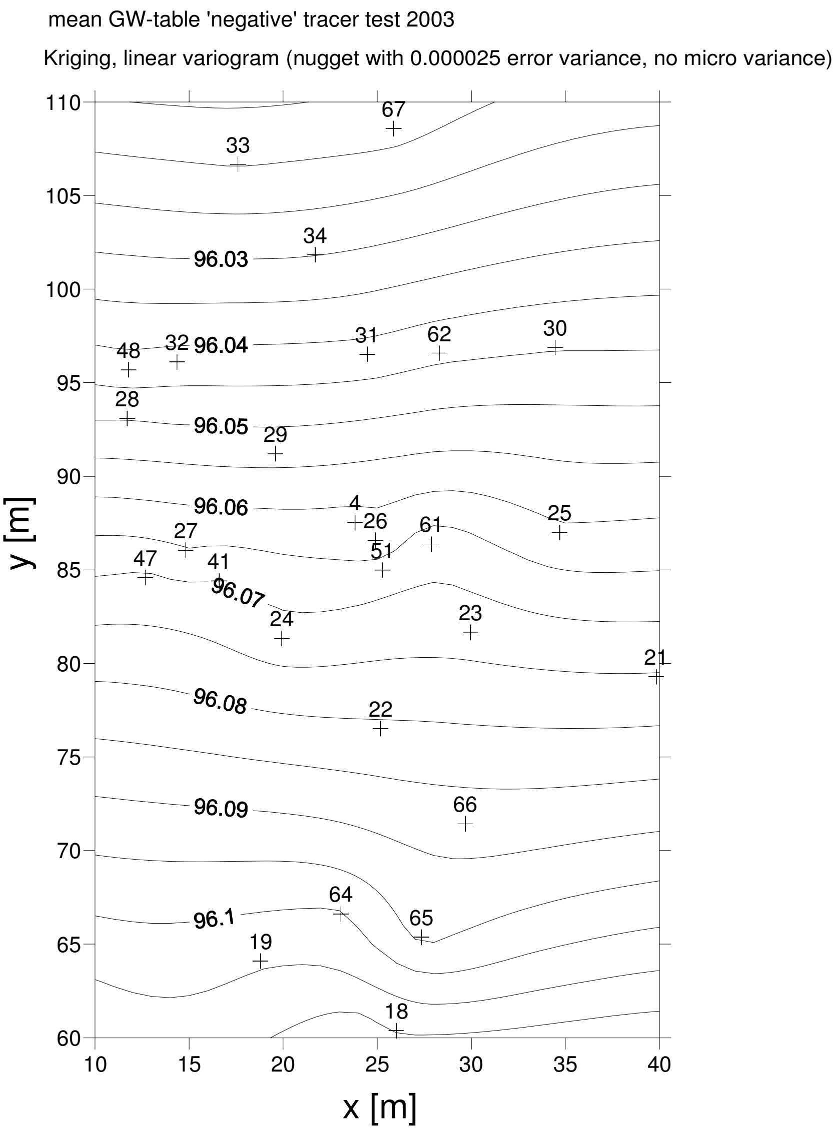
mean GW-table 'negative' tracer test 2003
Kriging, linear variogram (nugget with 0.000025 error variance, no micro variance)
96.03
96.04
96.05
96.06
96.07
96.08
96.09
96.1
67
33
34
48
32
31
62
30
28
29
4
26
61
25
27
47
41
51
24
23
21
22
66
64
65
19
18
y [m]
x [m]

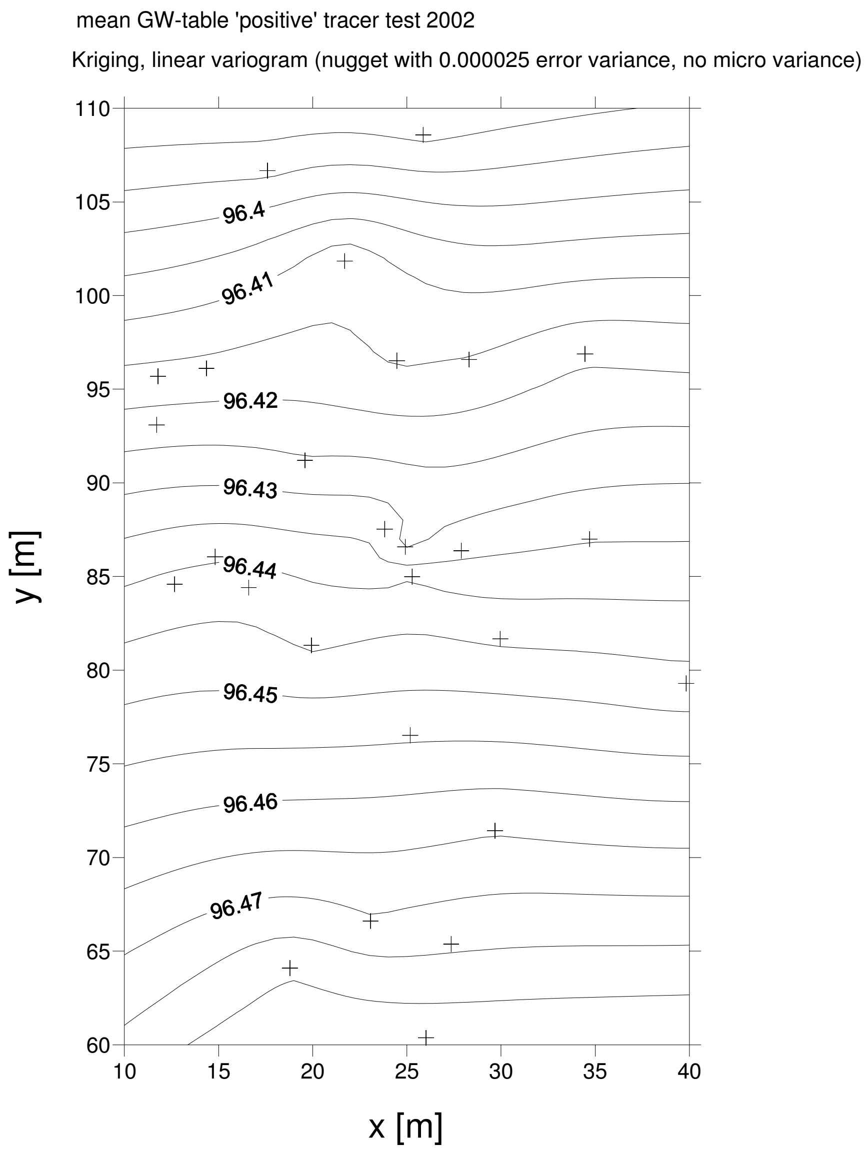
mean GW-table 'positive' tracer test 2002
Kriging, linear variogram (nugget with 0.000025 error variance, no micro variance)
96.4
96.41
96.42
96.43
96.44
96.45
96.46
96.47
110
105
100
95
90
85
80
75
70
65
60
10
15
20
25
30
35
40
y [m]
x [m]

1. **Energiemodelle in der Bundesrepublik Deutschland. Stand der Entwicklung**
   IKARUS-Workshop vom 24. bis 25. Januar 1996
   herausgegeben von S. Molt, U. Fahl (1997), 292 Seiten
   ISBN: 3-89336-205-3

2. **Ausbau erneuerbarer Energiequellen in der Stromwirtschaft**
   Ein Beitrag zum Klimaschutz
   Workshop am 19. Februar 1997, veranstaltet von der Forschungszentrum Jülich GmbH und der Deutschen Physikalischen Gesellschaft
   herausgegeben von J.-Fr. Hake, K. Schultze (1997), 138 Seiten
   ISBN: 3-89336-206-1

3. **Modellinstrumente für CO_2-Minderungsstrategien**
   IKARUS-Workshop vom 14. bis 15. April 1997
   herausgegeben von J.-Fr. Hake, P. Markewitz (1997), 284 Seiten
   ISBN: 3-89336-207-X

4. **IKARUS-Datenbank - Ein Informationssystem zur technischen, wirtschaftlichen und umweltrelevanten Bewertung von Energietechniken**
   IKARUS. Instrumente für Klimagas-Reduktionsstrategien
   Abschlußbericht Teilprojekt 2 „Datenbank“
   H.-J. Laue, K.-H. Weber, J. W. Tepel (1997), 90 Seiten
   ISBN: 3-89336-214-2

5. **Politikszenarien für den Klimaschutz**
   Untersuchungen im Auftrag des Umweltbundesamtes
   Band 1. Szenarien und Maßnahmen zur Minderung von CO_2-Emissionen in Deutschland bis zum Jahre 2005
   herausgegeben von G. Stein, B. Strobel (1997), 410 Seiten
   ISBN: 3-89336-215-0

6. **Politikszenarien für den Klimaschutz**
   Untersuchungen im Auftrag des Umweltbundesamtes
   Band 2. Emissionsminderungsmaßnahmen für Treibhausgase, ausgenommen energiebedingtes CO_2
   herausgegeben von G. Stein, B. Strobel (1997), 110 Seiten
   ISBN: 3-89336-216-9

7. **Modelle für die Analyse energiebedingter Klimagasreduktionsstrategien**
   IKARUS. Instrumente für Klimagas-Reduktionsstrategien
   Abschlußbericht Teilprojekt 1 „Modelle“
   P. Markewitz, R. Heckler, Ch. Holzapfel, W. Kuckshinrichs, D. Martinsen, M. Walbeck, J.-Fr. Hake (1998), VI, 276 Seiten
   ISBN: 3-89336-220-7

8. **Politikszenarien für den Klimaschutz**
Untersuchungen im Auftrag des Umweltbundesamtes
Band 3. Methodik-Leitfaden für die Wirkungsabschätzung von Maßnahmen zur Emissionsminderung
herausgegeben von G. Stein, B. Strobel (1998), VIII, 95 Seiten
ISBN: 3-89336-222-3

9. **Horizonte 2000**
6. Wolfgang-Ostwald-Kolloquium der Kolloid-Gesellschaft
3. Nachwuchstage der Kolloid- und Grenzflächenforschung
Kurzfassungen der Vorträge und Poster
zusammengestellt von F.-H. Haegel, H. Lewandowski, B. Krahl-Urban (1998), 150 Seiten
ISBN: 3-89336-223-1

10. **Windenergieanlagen - Nutzung, Akzeptanz und Entsorgung**
von M. Kleemann, F. van Erp, R. Kehrbaum (1998), 59 Seiten
ISBN: 3-89336-224-X

11. **Policy Scenarios for Climate Protection**
Study on Behalf of the Federal Environmental Agency
Volume 4. Methodological Guideline for Assessing the Impact of Measures for Emission Mitigation
edited by G. Stein, B. Strobel (1998), 103 pages
ISBN: 3-89336-232-0

12. **Der Landschaftswasserhaushalt im Flußeinzugsgebiet der Elbe**
Verfahren, Datengrundlagen und Bilanzgrößen
Analyse von Wasserhaushalt, Verweilzeiten und Grundwassermilieu im Flußeinzugsgebiet der Elbe (Deutscher Teil). Abschlußbericht Teil 1.
von R. Kunkel, F. Wendland (1998), 110 Seiten
ISBN: 3-89336-233-9

13. **Das Nitratabbauvermögen im Grundwasser des Elbeeinzugsgebietes**
Analyse von Wasserhaushalt, Verweilzeiten und Grundwassermilieu im Flußeinzugsgebiet der Elbe (Deutscher Teil). Abschlußbericht Teil 2.
von F. Wendland, R. Kunkel (1999), 166 Seiten
ISBN: 3-89336-236-3

14. **Treibhausgasminderung in Deutschland zwischen nationalen Zielen und internationalen Verpflichtungen**
IKARUS-Workshop am 27.05.1998, Wissenschaftszentrum Bonn-Bad Godesberg. Proceedings
herausgegeben von E. Läge, P. Schaumann, U. Fahl (1999), ii, VI, 146 Seiten
ISBN: 3-89336-237-1

15. **Satellitenbildauswertung mit künstlichen Neuronalen Netzen zur Umweltüberwachung**
    Vergleichende Bewertung konventioneller und Neuronaler Netzwerkalgorithmen und Entwicklung eines integrierten Verfahrens
    von D. Klaus, M. J. Canty, A. Poth, M. Voß, I. Niemeyer und G. Stein (1999), VI, 160 Seiten
    ISBN: 3-89336-242-8

16. **Volatile Organic Compounds in the Troposphere**
    Proceedings of the Workshop on Volatile Organic Compounds in the Troposphere held in Jülich (Germany) from 27 – 31 October 1997
    edited by R. Koppmann, D. H. Ehhalt (1999), 208 pages
    ISBN: 3-89336-243-6

17. **CO_2-Reduktion und Beschäftigungseffekte im Wohnungssektor durch das CO_2-Minderungsprogramm der KfW**
    Eine modellgestützte Wirkungsanalyse
    von M. Kleemann, W. Kuckshinrichs, R. Heckler (1999), 29 Seiten
    ISBN: 3-89336-244-4

18. **Symposium über die Nutzung der erneuerbaren Energiequellen Sonne und Wind auf Fischereischiffen und in Aquakulturbetrieben**
    Symposium und Podiumsdiskussion, Izmir, Türkiye, 28.-30.05.1998. Konferenzbericht
    herausgegeben von A. Özdamar, H.-G. Groehn, K. Ülgen (1999), IX, 245 Seiten
    ISBN: 3-89336-247-9

19. **Das Weg-, Zeitverhalten des grundwasserbürtigen Abflusses im Elbeeinzugsgebiet**
    Analyse von Wasserhaushalt, Verweilzeiten und Grundwassermilieu im Flußeinzugsgebiet der Elbe (Deutscher Teil). Abschlußbericht Teil 3.
    von R. Kunkel, F. Wendland (1999), 122 Seiten
    ISBN: 3-89336-249-5

20. **Politikszenarien für den Klimaschutz**
    Untersuchungen im Auftrag des Umweltbundesamtes
    Band 5. Szenarien und Maßnahmen zur Minderung von CO_2-Emissionen in Deutschland bis 2020
    herausgegeben von G. Stein, B. Strobel (1999), XII, 201 Seiten
    ISBN: 3-89336-251-7

21. **Klimaschutz durch energetische Sanierung von Gebäuden. Band 1**
    von J.-F. Hake, M. Kleemann, G. Kolb (1999), 216 Seiten
    ISBN: 3-89336-252-2

22. **Electroanalysis**
Abstracts of the 8th International Conference held from 11 to 15 June 2000 at the University of Bonn, Germany
edited by H. Emons, P. Ostapczuk (2000), ca. 300 pages
ISBN: 3-89336-261-4

23. **Die Entwicklung des Wärmemarktes für den Gebäudesektor bis 2050**
von M. Kleemann, R. Heckler, G. Kolb, M. Hille (2000), II, 94 Seiten
ISBN: 3-89336-262-2

24. **Grundlegende Entwicklungstendenzen im weltweiten Stoffstrom des Primäraluminiums**
von H.-G. Schwarz (2000), XIV, 127 Seiten
ISBN: 3-89336-264-9

25. **Klimawirkungsforschung auf dem Prüfstand**
Beiträge zur Formulierung eines Förderprogramms des BMBF
Tagungsband des Workshop „Klimaforschung“, Jülich, vom 02. bis 03.12.1999
von J.-Fr. Hake, W. Fischer (2000), 150 Seiten
ISBN: 3-89336-270-3

26. **Energiezukunft 2030**
Schlüsseltechnologien und Techniklinien
Beiträge zum IKARUS-Workshop 2000 am 2./3. Mai 2000
herausgegeben von U. Wagner, G. Stein (2000), 201 Seiten
ISBN: 3-89336-271-1

27. **Der globale Wasserkreislauf und seine Beeinflussung durch den Menschen**
Möglichkeiten zur Fernerkundungs-Detektion und -Verifikation
von D. Klaus und G. Stein (2000), 183 Seiten
ISBN: 3-89336-274-6

28. **Satelliten und nukleare Kontrolle**
Änderungsdetektion und objektorientierte, wissensbasierte Klassifikation von Multispektralaufnahmen zur Unterstützung der nuklearen Verifikation
von I. Niemeyer (2001), XIV, 206 Seiten
ISBN: 3-89336-281-9

29. **Das hydrologische Modellsystem J2000**
Beschreibung und Anwendung in großen Flußgebieten
von P. Krause (2001), XIV, 247 Seiten
ISBN: 3-89336-283-5

30. **Aufwands- und ergebnisrelevante Probleme der Sachbilanzierung**
von G. Fleischer, J.-Fr. Hake (2002), IV, 64 Blatt
ISBN: 3-89336-293-2

31. **Nachhaltiges Management metallischer Stoffströme**
Indikatoren und deren Anwendung
Workshop, 27.-28.06.2001 im Congresscentrum Rolduc, Kerkrade (NL)
herausgegeben von W. Kuckshinrichs, K.-L. Hüttner (2001), 216 Seiten
ISBN: 3-89336-296-7

32. **Ansätze zur Kopplung von Energie- und Wirtschaftsmodellen zur Bewertung zukünftiger Strategien**
IKARUS-Workshop am 28. Februar 2002, BMWi, Bonn. Proceedings
herausgegeben von S. Briem, U. Fahl (2003), IV, 184 Seiten
ISBN: 3-89336-321-1

33. **TRACE. Tree Rings in Archaeology, Climatology and Ecology**
Volume 1: Proceedings of the Dendrosymposium 2002,
April 11th – 13th 2002, Bonn/Jülich, Germany
edited by G. Schleser, M. Winiger, A. Bräuning et al., (2003), 135 pages, many partly coloured illustrations
ISBN: 3-89336-323-8

34. **Klimaschutz und Beschäftigung durch das KfW-Programm zur CO_2-Minderung und das KfW-CO_2-Gebäudesanierungsprogramm**
von M. Kleemann, R. Heckler, A. Kraft u. a., (2003), 53 Seiten
ISBN: 3-89336-326-2

35. **Klimaschutz und Klimapolitik: Herausforderungen und Chancen**
Beiträge aus der Forschung
herausgegeben von J.-Fr. Hake, K. L. Hüttner (2003), III, 231 Seiten
ISBN: 3-89336-327-0

36. **Umweltschutz und Arbeitsplätze, angestoßen durch die Tätigkeiten des Schornsteinfegerhandwerks**
Auswertung von Schornsteinfeger-Daten
von M. Kleemann, R. Heckler, B. Krüger (2003), VII, 66 Seiten
ISBN: 3-89336-328-9

37. **Die Grundwasserneubildung in Nordrhein-Westfalen**
von H. Bogena, R. Kunkel, T. Schöbel, H. P. Schrey, F. Wendland (2003), 148 Seiten
ISBN: 3-89336-329-7

38. **Dendro-Isotope und Jahrringbreiten als Klimaproxis der letzten 1200 Jahre im Karakorumgebirge/Pakistan**
von K. S. Treydte (2003), XII, 167 Seiten
ISBN: 3-89336-330-0

39. **Das IKARUS-Projekt: Energietechnische Perspektiven für Deutschland**
herausgegeben von P. Markewitz, G. Stein (2003), IV, 274 Seiten
ISBN: 3-89336-333-5

40. **Umweltverhalten von MTBE nach Grundwasserkontamination**
von V. Linnemann (2003), XIV, 179 Seiten
ISBN: 3-89336-339-4

41. **Climate Change Mitigation and Adaptation: Identifying Options for Developing Countries**
Proceedings of the Summer School on Climate Change, 7-17 September 2003, Bad Münstereifel, Germany
edited by K. L. Hüttner, J.-Fr. Hake, W. Fischer (2003), XVI, 341 pages
ISBN: 3-89336-341-6

42. **Mobilfunk und Gesundheit: Risikobewertung im wissenschaftlichen Dialog**
von P. M. Wiedemann, H. Schütz, A. T. Thalmann (2003), 111 Seiten
ISBN: 3-89336-343-2

43. **Chemical Ozone Loss in the Arctic Polar Stratosphere: An Analysis of Twelve Years of Satellite Observations**
by S. Tilmes (2004), V, 162 pages
ISBN: 3-89336-347-5

44. **TRACE. Tree Rings in Archaeology, Climatology and Ecology**
Volume 2: Proceedings of the Dendrosymposium 2003,
May 1st – 3rd 2003, Utrecht, The Netherlands
edited by E. Jansma, A. Bräuning, H. Gärtner, G. Schleser (2004), 174 pages
ISBN: 3-89336-349-1

45. **Vergleichende Risikobewertung: Konzepte, Probleme und Anwendungsmöglichkeiten**
von H. Schütz, P. M. Wiedemann, W. Hennings et al. (2004), 231 Seiten
ISBN: 3-89336-350-5

46. **Grundlagen für eine nachhaltige Bewirtschaftung von Grundwasserressourcen in der Metropolregion Hamburg**
von B. Tetzlaff, R. Kunkel, R. Taugs, F. Wendland (2004), 87 Seiten
ISBN: 3-89336-352-1

47. **Die natürliche, ubiquitär überprägte Grundwasserbeschaffenheit in Deutschland**
von R. Kunkel, H.-J. Voigt, F. Wendland, S. Hannappel (2004), 207 Seiten
ISBN: 3-89336-353-X

48. **Water and Sustainable Development**
edited by H. Bogena, J.-Fr. Hake, H. Vereecken (2004), 199 pages
ISBN: 3-89336-357-2

49. **Geo- and Biodynamic Evolution during Late Silurian / Early Devonian Time (Hazro Area, SE Turkey)**
by O. Kranendonck (2004), XV, 268 pages
ISBN: 3-89336-359-9

50. **Politikszenarien für den Umweltschutz**
Untersuchungen im Auftrag des Umweltbundesamtes
Langfristszenarien und Handlungsempfehlungen ab 2012 (Politikszenarien III)
herausgegeben von P. Markewitz u. H.-J. Ziesing (2004), XVIII, 502 Seiten
ISBN: 3-89336-370-X

51. **Die Sauerstoffisotopenverhältnisse des biogenen Opals lakustriner Sedimente als mögliches Paläothermometer**
von R. Moschen (2004), XV, 130 Seiten
ISBN: 3-89336-371-8

52. **MOSYRUR: Water balance analysis in the Rur basin**
von Heye Bogena, Michael Herbst, Jürgen-Friedrich Hake, Ralf Kunkel, Carsten Montzka, Thomas Pütz, Harry Vereecken, Frank Wendland (2005), 155 Seiten
ISBN: 3-89336-385-8

53. **TRACE. Tree Rings in Archaeology, Climatology and Ecology**
Volume 3: Proceedings of the Dendrosymposium 2004,
April 22nd – 24th 2004, Birmensdorf, Switzerland
edited by Holger Gärtner, Jan Esper, Gerhard H. Schleser (2005), 176 pages
ISBN: 3-89336-386-6

54. **Risikobewertung Mobilfunk: Ergebnisse eines wissenschaftlichen Dialogs**
herausgegeben von P. M. Wiedemann, H. Schütz, A. Spangenberg (2005), ca. 380 Seiten
ISBN: 3-89336-399-8

55. **Comparison of Different Soil Water Extraction Systems for the Prognoses of Solute Transport at the Field Scale using Numerical Simulations, Field and Lysimeter Experiments**
by L. Weihermüller (2005), ca. 170 pages
ISBN: 3-89336-402-1

56. **Effect of internal leaf structures on gas exchange of leaves**
by R. Pieruschka (2005), 120 pages
ISBN: 3-89336-403-X

57. **Temporal and Spatial Patterns of Growth and Photosynthesis in Leaves of Dicotyledonous Plants Under Long-Term CO2- and O3-Exposure**
by M. M. Christ (2005), 125 pages
ISBN: 3-89336-406-4

58. **Öffentliche Kommunikation über Klimawandel und Sturmflutrisiken Bedeutungskonstruktion durch Experten, Journalisten und Bürger**
von H. P. Peters, H. Heinrichs (2005), 231 Seiten, CD
ISBN: 3-89336-415-3

59. **Umsatz verschiedener Ernterückstände in einem Bodensäulenversuchssystem – Einfluss auf die organische Bodensubstanz und den Transport zweier Xenobiotika**
von N. Drewes (2005), 221 Seiten
ISBN: 3-89336-417-X

60. **Evaluierung der CO2-Minderungsmaßnahmen im Gebäudebereich**
von M. Kleemann, P. Hansen (2005), 84 Seiten
ISBN: 3-89336-419-6

61. **TRACE. Tree Rings in Archaeology, Climatology and Ecology**
Volume 4: Proceedings of the Dendrosymposium 2005,
April 21st – 23rd 2005, Fribourg, Switzerland
edited by Ingo Heinrich, Holger Gärtner, Michel Monbaron, Gerhard Schleser (2006), 313 pages
ISBN: 3-89336-425-0

62. **Diffuse Nitrateinträge in die Grund- und Oberflächengewässer von Rhein und Ems**
Ist-Zustands- und Maßnahmenanalysen
von R. Kunkel, F. Wendland (2006), 130 Seiten
ISBN: 3-89336-437-4

63. **Abhängigkeit des Wurzelwachstums vom Lichtregime des Sprosses und deren Modifikation durch Nährstoffe sowie im Gravitropismus**
von Kerstin A. Nagel (2006), 119 Seiten
ISBN: 3-89336-443-9

64. **Chancen und Risiken zukünftiger netzgebundener Versorgung**
Ein multi-kriterielles Verfahren zur Bewertung von Zukunftsszenarien
von C. R. Karger, W. Hennings, T. Jäger (2006), 296 Seiten
ISBN: 3-89336-445-5

65. **Die Phosphatbelastung großer Flusseinzugsgebiete aus diffusen und punktuellen Quellen**
von B. Tetzlaff (2006), 287 Seiten
ISBN: 3-89336-447-1

66. **Fate of veterinary pharmaceuticals in soil: An experimental and numerical study on the mobility, sorption and transformation of sulfadiazine**
by A. Wehrhan (2006), XXII, 134 pages
ISBN: 3-89336-448-X

67. **Biomacromolecules of Fossil Algae, Spores and Zooclasts from Selected Time Windows of Proterozoic to Mesozoic Age as Revealed by Pyrolysis-Gas Chromatography-Mass Spectrometry – A Biogeochemical Study**
by S. Dutta (2006), XVI, 139 pages
ISBN: 3-89336-455-2

68. **Bestimmung der Nicotinverteilung und anderer Stickstoffverbindungen in den Blattgeweben von *Nicotiana tabacum* unter verschiedenen Wachstumsbedingungen durch Einzelzellanalyse, Kapillarelektrophorese und der Massenspektrometrie**
von K. Wieland (2006), X, 189 Seiten
ISBN: 3-89336-458-7

69. **Systemic effects of mycorrhization on root and shoot physiology of *Lycopersicon esculentum***
by K. Klug (2006), IV, 105 Seiten
ISBN: 3-89336-463-3

70. **The impact of nutrient heterogeneity on maize plants**
by R. Rist (2006), XII, 74 Seiten
ISBN: 3-89336-464-1

71. **Optimization of Tracer Experiments to Characterize Transport Properties in Heterogeneous Aquifers Using Non-Invasive Measurement Techniques**
by K. Müller (2006), XVII, 103 Seiten
ISBN: 3-89336-465-X

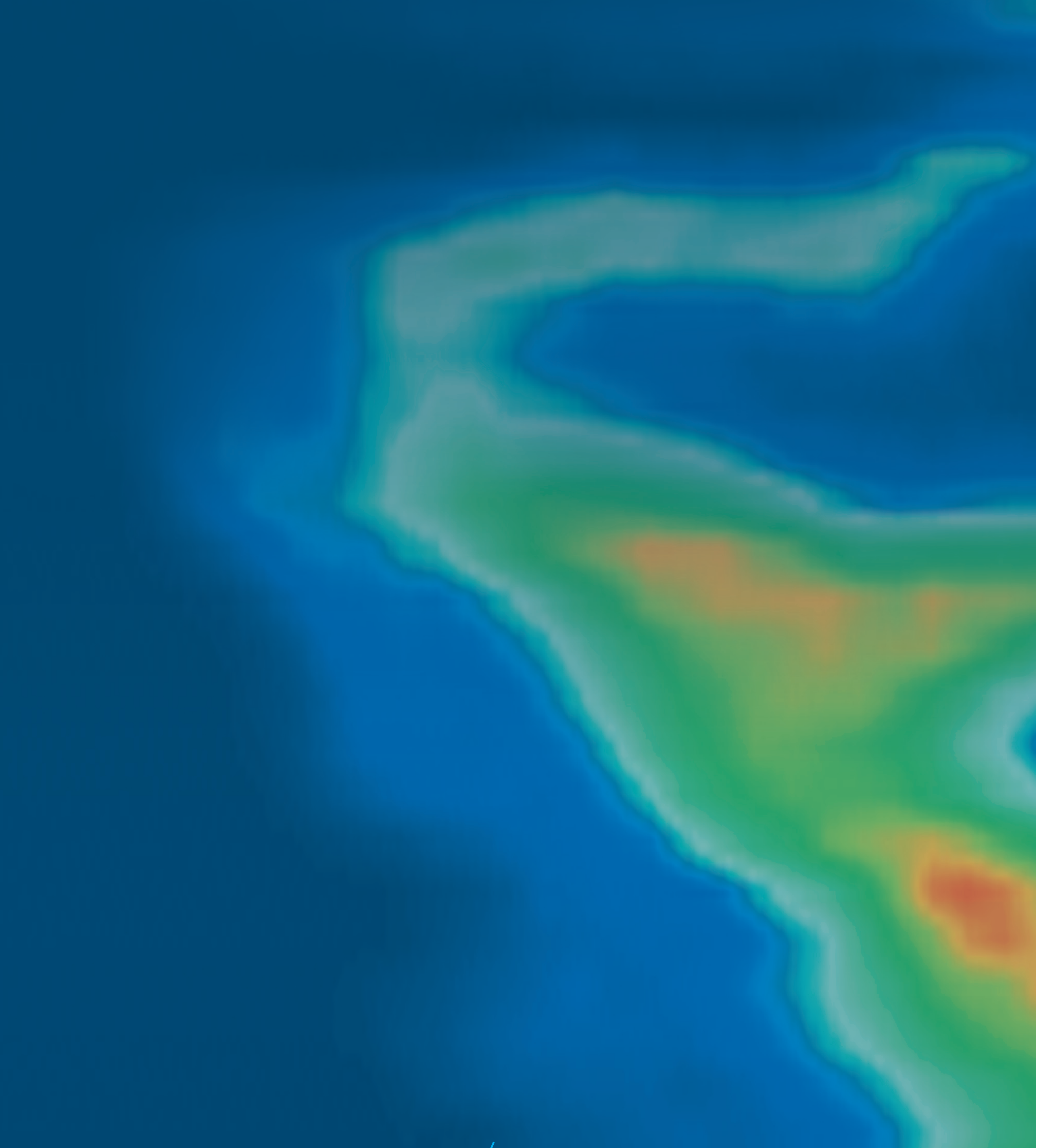

Forschungszentrum Jülich
in der Helmholtz-Gemeinschaft

50 Jahre / Zukunft

Band/Volume 71
ISBN 3-89336-465-X

Umwelt
Environment